THE CATHOLIC UNIVERSITY OF AMERICA

A Coupled Microresonator Array for Mass Detection

A DISSERTATION

Submitted to the Faculty of the

Department of Mechanical Engineering

School of Engineering

Of The Catholic University of America

In Partial Fulfillment of the Requirements

For the Degree

Doctor of Philosophy

By

Teresa J. Ryan

Washington, D.C

2013

A Coupled Microresonator Array for Mass Detection

Teresa J. Ryan, Ph.D.

Directed by: John A. Judge, Ph.D.

This work describes a method of mass detection based on coupled arrays of nominally identical resonators. Coupled arrays of this type can be used for a variety of applications, however this work primarily focuses on ultrasensitive mass detection, in which resonator surfaces are functionalized to selectively adsorb one or more target analytes (e.g., chemical or biological agents). The measurement of a system resonant frequency and resonator amplitudes describing the corresponding system mode shape provides the basis for the determination of resonator masses, which are increased by the presence of the target analyte(s). A weighted average of results from measurements of multiple system modes is used to improve the robustness of the approach.

The first part of this work describes numerical investigation of the sensitivity of this mass detection approach to measurement noise. System mode shapes are perturbed to simulate measurement noise, and resulting errors in identifying system masses are quantified as a function of array size, coupling strength, and level of mass variation. Sensitivity to measurement noise is low for lightly coupled arrays of nearly identical elements and increases when mass variation causes significant mode localization. For any mass variation level, an optimal combination of array size and coupling strength minimizes noise sensitivity.

The second part of this work is an experimental investigation using arrays of nearest-neighbor coupled silicon cantilevers. Designs with a range of coupling strengths are fabricated. The results support the findings of the numerical simulations. Below a transition value in the ratio of mass

disorder to coupling strength, responses are spatially extended and the sensitivity of the mass calculation to noise is independent of disorder. Above the transition, mode localization becomes significant and the error in mass identification increases with increasing mass disorder. Experimental results show that in the regime with extended responses, the sensor is linear and highly repeatable when detecting mass up to approximately 15% of the mass of a single cantilever. When used in a regime with localized responses, standard deviation of mass calculations increases dramatically. A threshold of detection for the method is experimentally found to be 0.2% of the cantilever mass ($\alpha = 0.01$).

This thesis by Teresa J. Ryan fulfills the thesis requirement for the doctoral degree in Mechanical Engineering approved by John A. Judge, Ph.D., as Director, and by Joseph F. Vignola, Ph.D., and George P. Mavroeidis, Ph.D. as Readers.

John A. Judge, Ph.D., Director

Joseph F. Vignola, Ph.D., Reader

George P. Mavroeidis, Ph.D., Reader

Sometimes the questions are complicated and the answers are simple.
Dr. Seuss

TABLE OF CONTENTS

LIST OF FIGURES

Figure **Page**

LIST OF TABLES

ACKNOWLEDGMENTS

This work supported by the National Science Foundation under Grant No. NSG-0747598.

Foremost among those due thanks and acknowledgment are Drs. Joseph Vignola and John Judge. The patience, humor, and understanding that accompanies their wealth of technical expertise seems limitless. Dr. Patrick O'Malley, though he was no longer in the office next door for the last few semesters of my work, remained an inspiration on many levels. The lab infrastructure he built and his software legacy has served us all well. I still want to be like Pat when I grow up. Many thanks to Aldo Glean for countless great conversations–enlightening technical discussions and peer review of works in progress as well as our common complaints on the cold weather, discussions of island time, etc. Also critical have been the keen eyes and steady hands of Hong Nguyen, without whom there would have been many more lost spheres in the vacuum chamber.

Beyond the folks at CUA, thanks are due to family and friends in many directions. First, my husband, Kurt, who has patiently endured the ever-moving projected completion date. My mom and sister, along with dear friends Deidre, Karen, and Harry have provided perspective, support, and reminders that there was light at the end of the tunnel through these whacky years in DC. Stefin provided critical feline assistants, mead, and a great place to live for a substantial portion of my time in DC. Thanks to you all.

CHAPTER 1

INTRODUCTION

1.1 Problem Statement and Proposed Work

Any investigation with resonant structures requires an understanding of the localization of vibration energy in a system. Different applications can capitalize on that localization in different ways. The foundation of this work is also localization; more specifically, this work lies at the intersection of these various topics and has the potential to add useful perspective to all of these seemingly disparate areas of inquiry. Although this work will be implemented with planar silicon structures with an emphasis on MEMS/NEMS opportunities, the underlying idea is general and widely applicable.

One goal of this effort is to demonstrate a prototype mass sensor system. The system is based on an array of coupled resonant microcantilevers and will use measured system resonant response amplitudes and frequencies to extract array characteristics. For the specific application of mass detection, numerical simulation and experiment will inform the practical question of detection threshold in a given array design in the presence of measurement noise. The broad plan of work includes:

- *Numerical Simulation:* The investigation uses a numerical model based on a one-dimensional array of coupled resonators. The simulations explore the sensitivity of system identification within a parameter space that includes element characteristics (stiffness, damping), array

characteristics (coupling ratio, mass and stiffness disorder, number of elements) and measurement parameters (noise, number of iterations used for averaging).

- *Experiment:* One-dimensional arrays of cantilevers are designed, fabricated and tested in a sequence of experiments that complement the numerical simulation described above. These experiments are conducted using a microscope-based scanning laser Doppler vibrometer (LDV) system. The vibrometer measurements are processed to yield an amplitude map of each target array. An inverse eigenvalue algorithm, which uses the amplitude map as input, is introduced as a novel technique for robust system mass identification. The experiments include arrays with characteristics that lie within the parameter space from the numerical work. Known masses are added to the cantilevers with specific goal of identifying the experimental threshold of detection as a percentage of cantilever mass.

1.2 Thesis Contribution

This work represents academic originality in a number of ways. The inverse eigenvalue technique advances the state of the art of coupled arrays in MEMS/NEMS as mass sensors. A robust method for mass identification, and the understanding of the sensitivity of that identification in the face of measurement noise and system disorder is a contribution to the field of complex system dynamics. The relationship between disorder, coupling strength, and array size is predicted by simulation and affirmed by experimental evidence, providing another tangible example of localization effects at work.

1.3 Organization of Thesis

Chapter 2 begins with a basic review of sensors and periodic systems. Section 2.1 tells the story of MEMS as an innovation in the signal processing community. The review of literature throughout Chapter 2 pulls together various lines of inquiry, ranging from the pursuit of a mono-

lithic radio-frequency filter[1] to the selective detection of a single molecule[2] to an artificial nose.[3,4] Such a broad foundation by nature lends broad applicability to the current work. Section 2.2 begins with an overview of microdevices as sensors which leads into a discussion of the various phenomena exploited (static deflection, resonant frequency shift, resonant response amplitudes, higher response modes), as well as a survey of the wide ranging scope and applicability of the technique. Chapter 3 frames the relevance and significance of this work by describing the connections to related inquiry. Chapter 3 begins by reviewing periodic systems (3.1) and the localization of vibration energy (3.2). The discussion includes ongoing work here at the Center for Acoustics, Vibrations, and Structures at the Catholic University of America on a related multi-element system. Section 3.3 is a summary of related work done by the author and collaborators in which one- and two-dimensional arrays of coupled paddle oscillators are investigated for use as a bandpass filter. The work on bandpass filters is included as it relates to the treatment of disorder and localization throughout this work. Chapter 4 begins the specific discussion of the proposed mass detection method, presenting the model and mathematical basis for the sensor. Sections 4.2 and 4.3 then present the approach for mass calculation and explore the sensitivity to noise of the approach with numerical simulation. Chapter 5 presents the methods and materials for the experimental work. Section 5.1 details the measurement system based around a scanning laser Doppler vibrometer, Section 5.2 describes the design of the prototype mass sensors, and Section 5.3 summarizes the protocols for protoype testing. Chapter 6 presents the experimental findings. Chapter 7 provides the conclusions and discusses future directions for this research.

CHAPTER 2

HISTORICAL CONTEXT: FROM SIGNAL PROCESSING TO MASS DETECTION

Chapter Introduction

Just over half a century has elapsed since a talk during which Richard Feynman put a $1000 bounty on production of an electric motor that would fit in a 1/64" cube or a legible 1/25,000 image of a printed page.[5] The stuff of 1959's science fiction has, year after year, become the stuff of scientific milestones, publications, and further inspiration. Exploration and innovation has maintained a steady barrage, advancing the edge of this frontier of diminishing dimensions ever smaller. Feynman assured us "there's plenty of room at the bottom" as the scale of structures shrinks. Four decades later, Michael Roukes reassures us that there is still plenty of room downscale, both in his lab at Caltech in Pasadena,[6] where Feynman gave his talk, and in laboratories around the world. It is both wondrous and inevitable that the "wow factor" of a mass sensor with yoctogram[7] sensitivity or real-time mass spectrometry of one molecule at a time[2] will fade, just as it has for the xenon atom rendition of the letters I,B, and M (Figure 2.1)[8] that caused such a sensation only a short time ago.

Rapidly changing fields such as this are difficult to capture in a textbook. As with any field, state of the art innovation is found in current journals. The following list of books, however, provides for a thorough treatment of the history and evolution of MEMS and NEMS from a variety of perspectives that goes beyond the focused summary presented in this work.

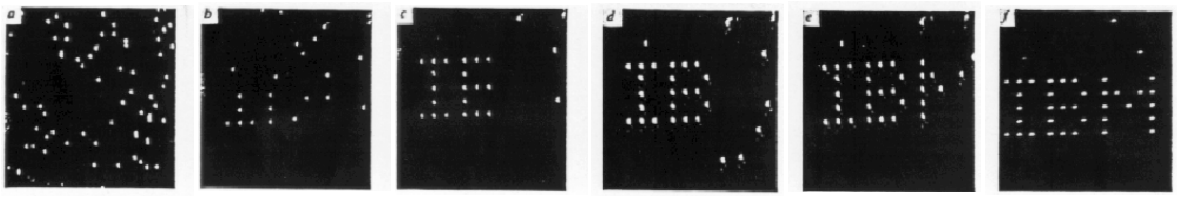

Figure 2.1: Reprinted by permission from Macmillan Publishers Ltd: Eigler, D. M., & Schweizer, E. K. (1990). Positioning single atoms with a scanning tunnelling microscope. *Nature*, 344(6266), 524-526. doi:10.1038/344524a0 ©1990 A sequence of STM images taken during the construction of a patterned array of xenon atoms. Grey scale is assigned according to the slope of the surface. The atomic structure of the nickel surface is not resolved. The $(1\bar{1}0)$ direction runs vertically. *a*) The surface after xenon dosing. *b-f*) Each letter is 50Å from top to bottom.[8]

- Stephen Beeby, *MEMS Mechanical Sensors*[9]
- Miko Elwenspoek, *Mechanical Microsensors*[10]
- Hector J. de los Santos *Introduction to Microelectromechanical Microwave Systems*[11]
- Stephen Senturia, *Microsystem Design*[12]
- Chang Liu, *Foundations of MEMS*[13]
- Marc J. Madou, *Fundamentals of Microfabrication: The Science of Miniaturization*[14]

The relative size scales of the MEMS and NEMS universe are included with some familiar objects in Figure 2.2. The prototype sensors used in this work fit into the small scale range, indicated by the lighter arrow in Figure 2.2. Conceptually, the ideas in this work generalize upward indefinitely and downward toward to the limit of classical mechanics and fabrication technology. Figure 2.3, reproduced from work by Lavrik,[15] shows comparative frequency and mass for micro-, nano-, and molecular scale structures. The cantilevers of these prototype sensors have masses on the order of 10^{-3}g and fundamental frequencies around 10 kHz placing these experiments just outside the lower left corner of Figure 2.3. The comparatively large size of the prototype allows for experiments with extremely high resolution control of system mass disorder. The intended implementation of

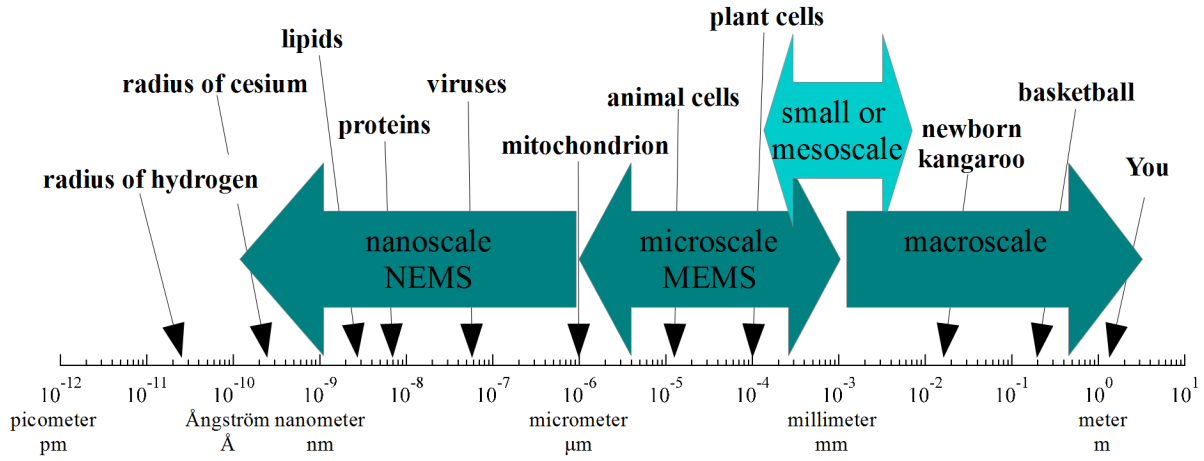

Figure 2.2: Representative object sizes from nano- to macroscale

the technique is well downscale from the size of the prototypes, with fundamental frequencies approaching GHz range.

As part of the race downward in scale, researchers have been exploring the behavior of microresonators individually and as systems in coupled arrays from a variety of application perspectives. The remainder of this chapter is dedicated to the history and evolution of microstructures generally and periodic arrays of coupled microstructures specifically. Though this work is focused on mass detection, the associated history lesson must begin with the quest for signal processing capability manufactured with complementary metal-oxide-semiconductor (CMOS) technology on a silicon chip. To some degree, it is the pioneering work in high frequency filters that provided both figurative and literal springboards that enabled a proliferation of sensors faster, smaller, and more sensitive than ever before.

Organization of Chapter

This chapter begins with a survey of early radio frequency filter research in Section 2.1 to frame the historical context of this work. As will be illustrated with a summary of some of our work with filters (Section 3.3), disorder is the enemy to those trying to use periodic systems for filtering. Sec-

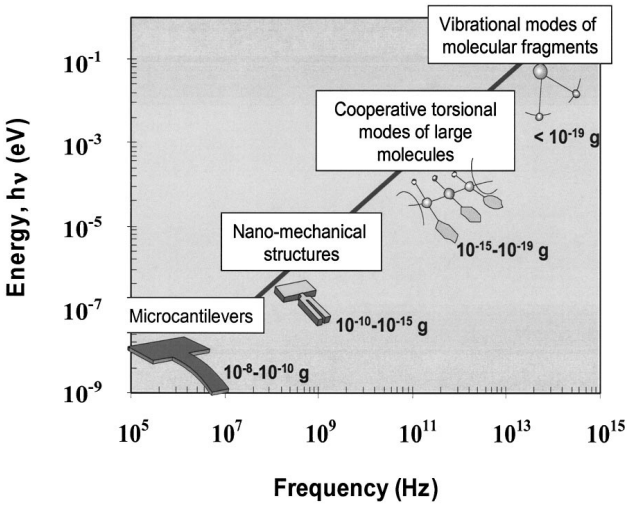

Figure 2.3: Mass and energy of micro- and nanoscale structures. Reprinted with permission from Lavrik, N. V., Sepaniak, M. J., & Datskos, P. G. (2004). Cantilever transducers as a platform for chemical and biological sensors. *Review of Scientific Instruments*, 75(7), 2229-2253. ©2004 American Institute of Physics. The cantilevers used in the experiments in this work have masses of approximately 10^{-3}g, with fundamental frequencies around 10^4 Hz.

tion 2.2 makes the transition out of the world of signal processing (in which sensitivity to disorder and vibration localization are phenomena to be overcome, minimized, and cleverly avoided) to the realm of microscale sensors, which exploits that sensitivity in order to detect changes in the system. A primer on sensor function is included in Section 2.2. The remainder of the chapter is a review of related work, beginning with the first resonant mass sensors, proceeding to the use of higher modes and arrays of sensors, and finishing with the work of Spletzer and Thiruvenkatanathan, which are the most relevant precursors to this investigation.

2.1 Filters: Evolution of High Frequency Filters

Before the storylines of periodic systems and sensors converge, this detour into signal processing is required to fully frame the current research. The commercial impact of the miniaturization of electronics is clear. Successful implementation of on-chip monolithic (CMOS) signal processing has the potential to bring about another revolutionary reduction in the physical scale and power

consumption of electronic devices, comparable to the one experienced with the advent of the transistor. Use of electromechanical devices for signal processing dates back to the World War II era.[16] The electromechanical components of that time were bulky and positioned separate from the electrical circuitry. The introduction of an electromechanical resonant gate transistor[17,18] in 1965 gave the revolution of miniaturization[19] a boost of momentum. The advent of surface acoustic wave devices[20] brought the filtering function onto the board, where it remains today in consumer electronics.

Researchers in the 1980's like Petersen[21] and Greenwood[22] were quick to acknowledge the tremendous potential in silicon micromechanical devices. Innovation in manufacturing and process technology throughout the 80's and 90's at last enabled the research as Feynman envisioned, on a truly microscale.[14] Among the early efforts, a number of researchers turned to the problem of developing signal filters using resonant micromechanical components. An ideal filter will transmit all of the signal energy within a desired frequency range (the pass band) with no distortion, and will transmit no energy at frequencies outside that band (the stop band). Filter rolloff is the term referring to the sharpness of the transition from the filter stop band to the pass band.

The simplest mechanical filter is composed of a single resonant structure, which will have a single resonant peak with bandwidth, Δ, that defines a narrow passband. In this simple case, *filter* bandwidth and *resonance* bandwidth are equal. Both the bandwidth and rolloff are determined by the quality factor, Q, of the resonance, which is an indicator of damping in a structure. One definition of quality factor is the ratio of the center frequency of the system resonance to the bandwidth of that resonance, $Q = f_c/\Delta$. A higher Q represents less damping and therefore longer energy retention and/or less energy loss per cycle of oscillation. As the filter design incorporates more than one resonant structure, *filter* bandwidth is determined by system characteristics such as spacing of the resonant peaks, while filter rolloff relies on the dissipation of energy within the system. That dissipation depends on the Q of individual resonant peaks: a narrow *resonance* bandwidth, Δ, increases Q, which makes for improved out-of-band rolloff.

Building from successful manufacture of a monolithic micromechanical oscillator[23] with a capacitive drive and sense mechanism, Nguyen and collaborators including Howe, Lin and others at both the University of Michigan and Berkeley were among the first to employ coupled microstructures.[1] Their work began with two or more nominally identical beams in various configurations beginning with nearest-neighbor coupled pairs and linear chains.[24–27] Bannon's work employed a mechanical coupling element between parallel clamped-clamped beams, where filter bandwidth is determined by coupling strength.[28,29] Shortly after, Clark *et. al.* reported electrical coupling of the same clamped-clamped oscillator pair architecture. A DC bias voltage is applied to one oscillator in order to change the frequency in a process known as frequency detuning.[30] The degree of detuning, or the amount of imposed variation, creates the filter passband. Electrical coupling of oscillators is explored further with both passive capacitive and active transistor-based methods.[31,32] The electrostatic force is also exploited as a means to actuate the resonators by way of interdigitated cantilevers or combs.[23,33,34] Beyond cantilever or clamped-clamped beam elements, circular coupling schemes and drumhead type resonators have also been explored.[35]

The search for a way to induce and transduce the vibration of these microstructures moved in step with the effort for devices with higher quality factor, Q. Much of the work with these high-Q resonant structures has been done in the absence of air to eliminate that damping. In 1998, Lin[36] introduced a planar encapsulation procedure to allow for retention of the higher Q observed under vacuum in a compact implementation. In the years since these early milestones, planar fabrication techniques continued to advance, allowing resonators with fully CMOS compatible actuation and detection being manufactured for research use.[37] Even today, a practical, fully manufacturable monolithic signal processing function remains elusive. Innovation in the laboratory continues to chase the next revolution in electronics as many researchers continue the effort to bring the filtering function onto a CMOS process chip by way of these high-Q oscillators.[29,38–46]

2.2 Sensor Background

This section presents a primer on basic sensor function while providing the remainder of the historical scaffolding for this work. The latter half of the 1980's saw the introduction of the first dynamic mode atomic force microscope[47] (Figure 2.4) and a proliferation of microscale devices,[48] such as the single resonating cantilever or bubble tolerant micropump pictured in Figure 2.5a and 2.5b. Innovation spawned outward from the advances in microfabrication, with resonant mass sens-

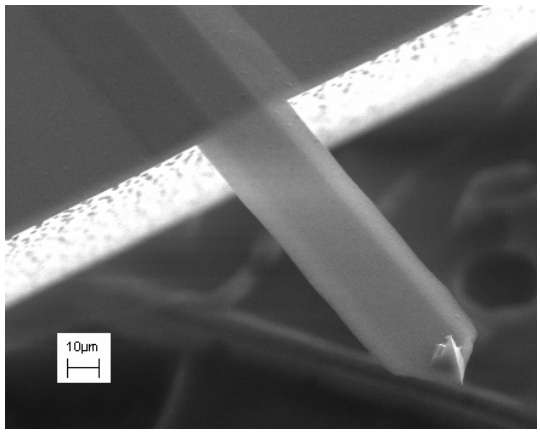

Figure 2.4: Typical atomic force microscope (AFM) cantilever[49]

ing among the first adaptations of the new microstructures. Ideas and applications spread quickly, and before long, a host of geometries (cantilever, plate,[50] diaphragm,[51,52] clamped single beams (bridges),[53–55] or multiple-bridge[56]) is in use sensing a wide range of quantities including temperature and/or humidity,[51,57–59] pressure,[52,60–62]force,[63] tilt,[64,65] radiation,[66,67] magnetic field,[68] alpha particle flux,[69] acceleration,[53,70] charge,[71] elastic properties,[72] surface stresses,[73] targeted chemical binding,[57,74] and biological adsorption,[75,76] as shown with the detection of *Escherichia coli* in Figure 2.6. Other innovations included devices such as microfans,[77] resonant pumps (diaphragm pumps),[14] and optical scanning systems.[78] Stemme's 1991 review of resonant sensors[61] provides an excellent early snapshot of the various sensor geometries, excitation and detection methods.

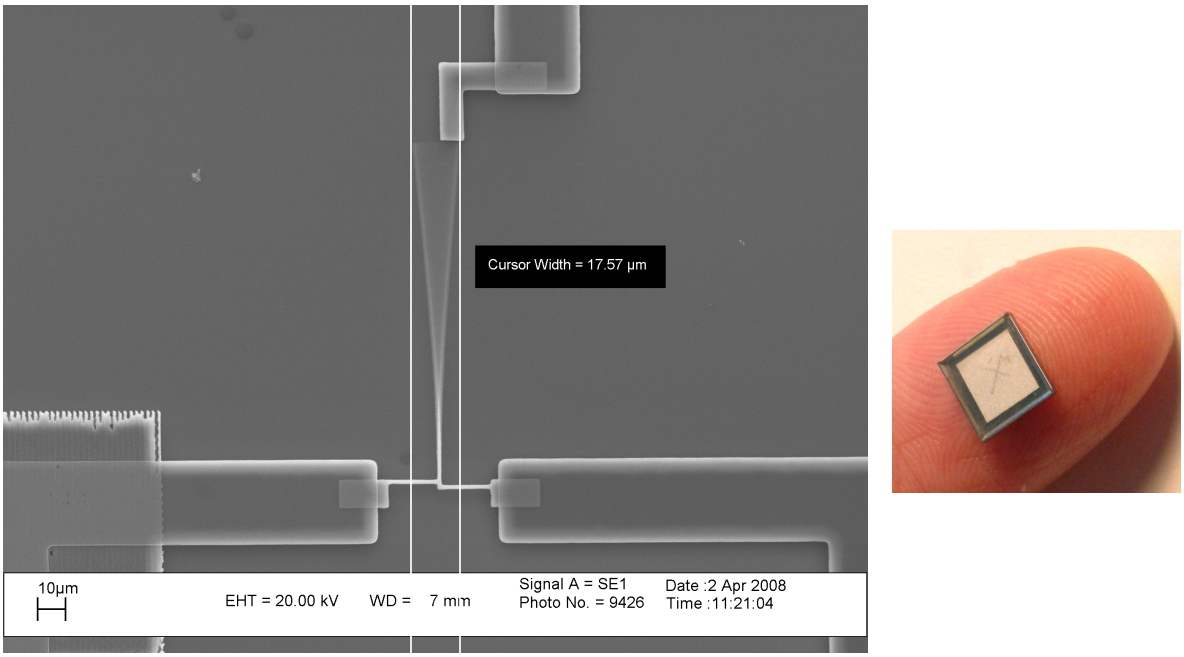

(a) (b)

Figure 2.5: Examples of microdevices. 2.5a. Scanning electron microscope image of a micro-cantilever in resonance, vibrating with a displacement of $\approx 10\mu$m.[79] 2.5b. A bubble tolerant micropump.[80]

In a filtering application, sensitivity to disorder is a hurdle to overcome. On the other hand, sensitivity to minute changes or differences becomes the fundamental advantage in the mass detection game. One of the first resonant mass sensors is a microbridge structure for vapor detection reported by Howe[54] in 1986. As with the filtering application, advances in manufacturing processes enabled the downward spiral in the scale of the devices and corresponding increase in sensitivities. Beginning in the early 90's with examples like Prescesky's sub-nanogram resonant silicon cantilever biosensor,[81] the limit of mass detection has steadily progressed downward through pico-,[82] femto-[15,75,83] and attogram scale detection.[74,84,85] As early as 2006, zeptogram-scale capability is reported for xenon and nitrogen gas detection[86,87] a mere 15 years after the "official birth" of the zeptogram[88] (10^{-21}g). As of 2012, even the yoctogram (10^{-24}g) has now been employed as a unit of actual sensed mass.[7]

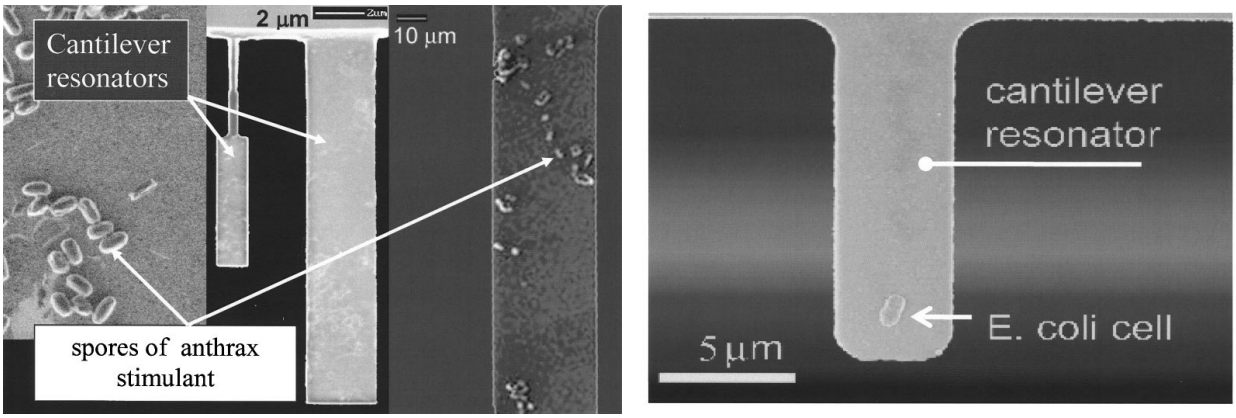

Figure 2.6: (left) Reprinted with permission from Lavrik, N. V., Sepaniak, M. J., & Datskos, P. G. (2004). Cantilever transducers as a platform for chemical and biological sensors. *Review of Scientific Instruments*, 75(7), 2229-2253. ©2004 American Institute of Physics. (right) Reprinted with permission from Ilic, B., Czaplewski, D., Zalalutdinov, M., Craighead, H. G., Neuzil, P., Campagnolo, C., & Batt, C. (2001). Single cell detection with micromechanical oscillators. *Journal of Vacuum Science & Technology B: Microelectronics and Nanometer Structures*, 19(6), 2825-2828. ©2001, American Vacuum Society.

2.2.1 Resonant sensor function

At the most basic level, a sensor is any device that exhibits a meaningful response to some change of state. Physical, chemical, or biological stimuli change a structure in a way that can be measured using optical, electronic, and other methods. One of the simplest mass sensors is a single cantilever which undergoes a predictable static deflection when loaded. Another simple mass sensor also involves our lowly cantilever. The sensing component (beam) is now set into motion, vibrating in a linear regime. When the beam changes in some way, the measured resonant response changes. Most often, the beam change is an increase in mass with corresponding decrease in resonant frequency as depicted in Figure 2.7. The shift may also result from changes in resonator stiffness or even mass loss[89] through a variety of processes including physisorption, chemisorption, evaporation, stress stiffening[90] or temperature shift.[91,92] For a simple cantilever vibrating in its fundamental flexural mode, the change in mass, Δm, is related to the change in frequency, δf, by

$$\Delta m = \frac{-2M}{f_0}\delta f \tag{2.1}$$

where M is the mass of the cantilever, and f_0 is the original resonant frequency. This resonance shift sensing paradigm is successful and ubiquitous due to the precision with which vibration frequency can be measured and the well understood limits of the approach.[93–97]

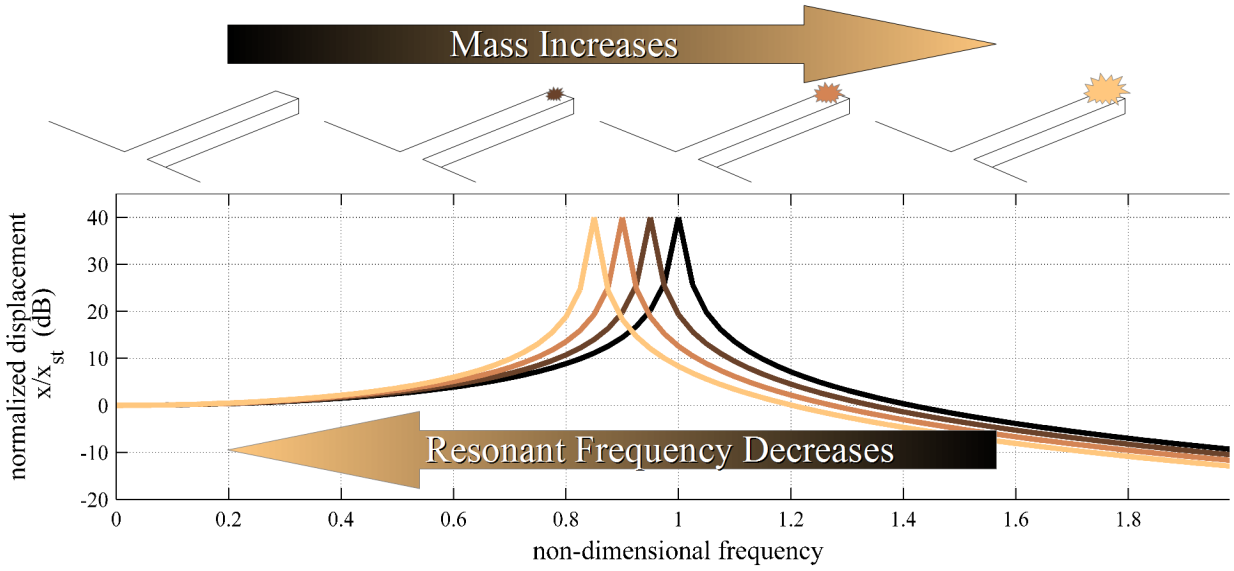

Figure 2.7: An illustration of the frequency decrease corresponding to mass increase in a resonant structure. The amount of added mass can be inferred from the frequency shift, as given in Equation 2.1.

2.2.2 Functionalization

In addition to the advantage of the well understood sensitivity, these devices can be given specificity by functionalizing the sensor surface. For large particles and substances that occur in sufficiently high concentrations, selective affinity for a particular measurand can be accomplished using various coatings.[54,66,98–101] These coatings include thiols,[102,103] siloxanes,[104] enzymes,[105] hydrogels, antibodies[106,107] and common polymers like polymethylmethacrylate, polystyrene, or polyurethane.[108] Chemical, biochemical, and geometric design[109–111] can combine for elegant solutions to the problem of specific analyte detection. Nano- or mesoporous materials can increase

the binding surface area of a sensor in cases with sufficiently small target substances.[112] The techniques, tricks, and pitfalls of surface functionalization, though fascinating and central to the ultimate utility of many devices of this kind, are beyond the scope of this work.

2.2.3 Scope and impact of applications

Resonant sensors have been designed to operate in a range of pressures from several atmospheres[62] to ultra-high vacuum and in a wide variety of environments including air[113–115] water,[89,116,117] and various solutions[118,119] (including biological[120–123]). Liquid environments pose a particular challenge for resonant operation due to the considerable dissipation and correspondingly low-Q resonant responses.[124] A decrease in quality factor increases the minimum resolvable resonance frequency shift, which decreases the sensitivity of the cantilever sensor.[120] One solution by Burg and colleagues is piping the liquid of interest through a microchannel in a resonant structure, maintaining the Q of similar structures without the microchannels. Specific molecules, cells, nanoparticles and changes in density have been detected with this technique.[123,125–127] Actuation and transduction in these devices can be acheived through a variety of methods including electromagnetic,[128,129] optical,[130,131] ultrasonic[115] thermal,[132–134] piezoelectric,[46,56,135] and piezoresistive.[136] A number of researchers have pushed downward in scale to the border between that which is mechanical and quantum.[137–142] Several others have developed techniques allowing for observation of quantum effects[137,143,144] and electron spin.[145,146]

Due to the wide range of operating environments and configuration options, the possible applications for this class of sensor span many industries and disciplines. Public health and military concerns often overlap and include detection of chemical or biological agents and monitoring of water supply or air quality. Relevant studies have included detection of anthrax simulant[15](Figure 2.6, left), trinitrotoluene deflagration,[89] dimethylmethlyphosphonate (a sarin gas precursor),[99] mercury vapors,[134,147] pesticides,[148] volatile organic compounds[149] like toluene,[150] and hexavalent chromium in ground water.[151] Industrial applications include manufacturing pro-

cess or quality control (monitoring product composition) and worker safety (air and water quality assessment).[51] Potential uses in the food and beverage industry also include safety and quality monitoring. One researcher reports on the detection of trimethylamine, which is an ammonia derivative and indicator of fish freshness.[112] Medical applications could enable rapid point-of-care assessment of simple analytes (glucose[105]) or ions (calcium[152] as well as more complex biological species (C-Reactive Protein,[153] Immunoglobulin-M[2] or Immunoglobulin-G[154,155]), cancer markers (Prostate Specific Antigen and Cancer Antigen 125)[156]), or other agents of clinical or diagnostic interest.[75,76,106,121,157–162]

2.2.4 Multi-mode sensing and sensor arrays

The current work builds on and connects several related research threads: using multiple sensing elements in arrays, the coupling of sensing elements, and using vibration information from the coupled system modes instead of relying on individual resonator frequency shifts. This section reviews related work in each of these threads, and closes with a discussion of the research on amplitude based sensing that is the immediate precursor to this work.

Many researchers demonstrate enhanced mass detection sensitivities when using vibration modes other than fundamental bending: lateral and torsional,[163] second bending,[114,162] fifth bending,[158] lateral,[164] or a combination of modes.[2,72,73,115,132,134,158,165–168] The issue of the position of the added mass on the cantilever has been investigated in a number of ways. Dohn demonstrated that position of a single bead can be deduced using resonant frequency shifts from multiple bending modes and showed positional dependence of increased sensitivity.[169–171] Other researchers have investigated the potentially confounding effects of mass location and stiffness changes along the cantilever.[101,172]

Another logical extension of the concept of a cantilever as a sensor is the simultaneous use of mulitple cantilevers. Battiston, Lang et. al. report the use of an uncoupled array of 8 cantilevers with specific coatings as the basis of an artificial nose.[3,149,173,174] That system detects chemical

vapor using both static[4] and dynamic[3] response monitoring. The pattern of responses among the 8 coated cantilevers allow for differential discrimination of complex vapors. Another relatively early use of multiple cantilevers is in a CMOS array for the detection of volatile organic compounds.[150] Yue et al.[121] measure static deflection in a liquid environment to detect binding of DNA strands in a ten element cantilever array to show feasibility of large scale multiplexing of bioassays. Dhayal used both static bending and higher bending modes in a cantilever array and demonstrated non-uniform binding of bacteria to the cantilever surface. Other recent advances include self-sustained actuation and parallel readout in a cantilever array[175] and a capacitive CMOS MEMS resonant sensor array.[176]

2.2.5 Coupled arrays and amplitude-based sensors

Yet another segment of research aims to exploit the collective system behavior observed when these micromechanical structures are coupled together. Numerous researchers[177–187] have studied the system shown in Figure 2.8b that has multiple small oscillators attached to a larger, primary oscillator. DeMartini[188,189] uses a system of this type with four subordinate oscillators for mass detection, relying on frequency shifts observed in the response of the primary mass to detect mass changes on the subordinates.

Spletzer[190,191] also uses coupled arrays of resonators for mass detection but implements the arrays with a fundamentally different sensing paradigm. The approach of DeMartini couples individual resonators through a single large shuttle mass. Detection of mass changes using system frequency response requires that the system response has well-isolated resonant peaks that are dominated by motion in only one of the subordinate resonators. That condition requires that the subordinate resonators are both sufficiently different and have sufficiently high Q (light damping). In other words, the DeMartini approach must have fully localized system modes. Glean[179] also uses localized modes in cantilevers coupled through a primary structure to identify changes in resonator mass. In contrast, the approach used by Spletzer employs the presumption of identi-

cal array elements coupled only to neighboring elements, as in Figure 2.8a. Changes in system mass are identified and pinpointed by observing vibration localization through changes in system eigenmodes. A similar approach by Thiruvenkatanathan uses electrical coupling between pairs of resonators to identify changes in resonator stiffness[192] and mass.[193] The electrical coupling offers not only the possibility of much smaller coupling ratios than the mechanical coupling in the work of Spletzer, but also the ability to easily manipulate the amount of coupling.[194]

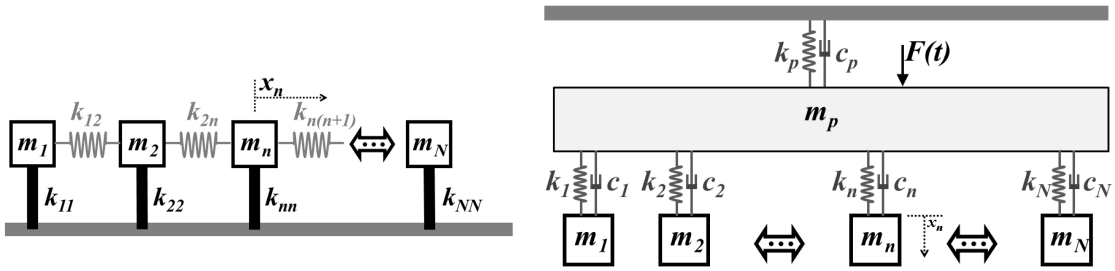

(a) (b)

Figure 2.8: Two coupling arrangements for SDOF oscillators: 2.8a. Nearest neighbor coupling, used in this work, Spletzer,[191] and Thiruvenkatanathan.[193] 2.8b. Coupling through a primary base structure. This basic arrangement is used in Glean[178,195] and DeMartini.[188]

The theoretical limits of detection with the amplitude based mass detection approaches used by Spletzer, Thiruvenkatanathan and the current work are less well established and are more subject to issues related to the chosen measurement method than those based on resonant frequency shift measurement.[93–95] A related question of how accurately amplitudes must be measured to accurately calculate system mass information is addressed in our work with numerical simulations, presented in Section 4.3. Thiruvenkatanathan notes the advantages of common mode rejection and increased sensitivity in amplitude based sensors as compared to frequency shift sensors.[196] That work[196] presents expressions for the fundamental measurement limit in shape-based sensors. In addition, it includes a thorough treatment of the ultimate sensitivity considering both intrinsic and extrinsic noise sources as well as a discussion of the limitations in such coupled dynamic systems due to the inherent bandwidth.

CHAPTER 3

BACKGROUND: PERIODIC AND NEARLY PERIODIC SYSTEMS, DISORDER, AND LOCALIZATION

Chapter Introduction

This chapter discusses periodic and nearly periodic systems and how the amount of disorder in such systems affects the distribution and transfer of energy into, out of, and within them. Sections 3.1 and 3.2 are a general introduction to this class of systems and localization phenomenon. Section 3.3 summarizes previous work using one- and two-dimensional paddle oscillators in a filtering application. The localization phenomenon is the connection between these different lines of inquiry; work in each area informs and imparts a greater significance to the others when that link is acknowledged and understood.

3.1 Periodic Systems

Generally, a periodic system is one with some sort of feature that repeats in space. This work is primarily concerned with an array of cantilever beams. The collective behavior of the cantilevers or any set of identical coupled structures generalizes for both linear or radial geometries and across many orders of magnitude on the size scale (Figure 2.2). That fact gives our array of cantilevers (Figure 3.1b) some perhaps unexpected siblings like bridges, antennae, trusses and turbines, as well as collections of carbon nanotubes or atomic lattices(see Figure 3.1). One important distinction in these coupled periodic systems is the nature of the link between the individual elements.

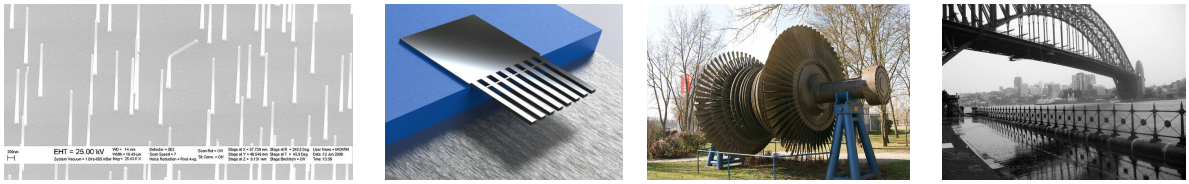

(a) (b) (c) (d)

Figure 3.1: A variety of periodic systems. (3.1a) Nanowire structures, $\approx$ 100 nm in diameter.[49] (3.1b) Eight element coupled cantilever array. (3.1c) A turbine on display at a German power plant.[197] (3.1d) Sydney harbor bridge.[198]

One manner of coupling is through a primary or central structure, as in the turbine (Figure 3.1c) or the subordinate oscillator arrays (Figure 3.2b) studied by many researchers including Vignola,[177] Glean,[179] Pierce,[199] Strasberg and Feit,[181,182] and Akay and Carcaterra.[185,200,201] The other coupling method (Figure 3.2a), uses direct connection between adjacent elements. These connections may be one dimensional—creating a simple linear chain, as in our arrays or a multispan beam on regularly spaced supports—or multidimensional, as in trusses or atomic lattices.

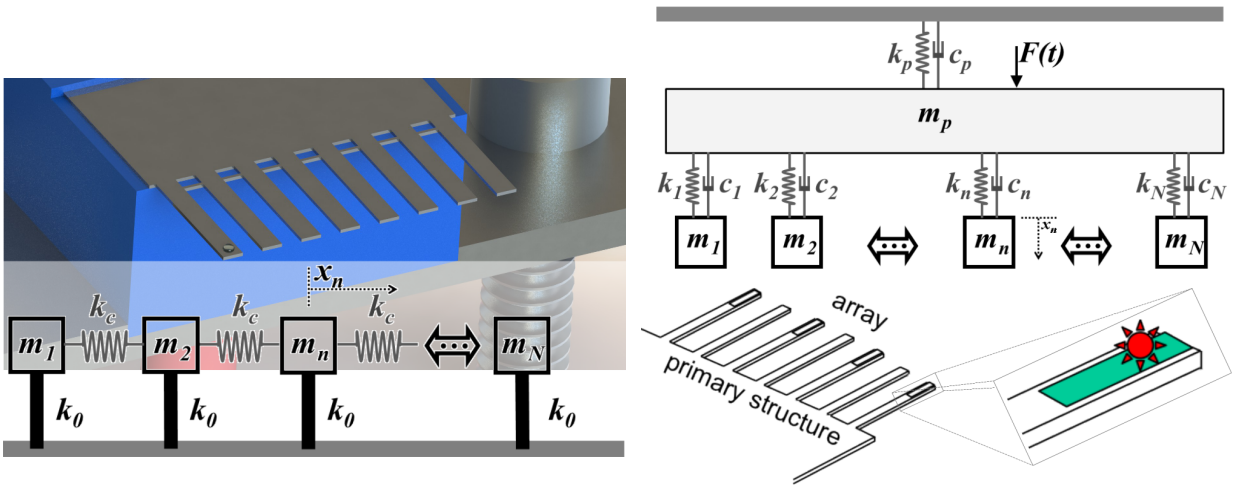

(a) (b)

Figure 3.2: Cantilever array based mass sensors. Lumped element model and schematic for two coupling arrangements. 3.2a. Nearest neighbor coupling in an N-degree of freedom mass-spring system with inherent element stiffnesses k_0 and coupling element stiffnesses k_c. Spacing between adjacent elements is d. 3.2b. An N-element system with coupling through a primary base structure.

Understanding the behavior of a nearly periodic structure first requires an understanding of what is expected for the periodic one. We begin by considering the fundamental unit of our array: a single cantilever beam. The lumped element model of this single cantilever is taken to be a simple mass-spring system, which has a single resonant frequency, f_0. With this mass-spring as our fundamental unit, our system model, shown in Figure 3.2a, is a chain of N units with identical masses, m, and identical inherent element stiffnesses, k_0. The size of this fundamental unit, or spacing from one mass to the next, is the distance d. Each unit is coupled only to the nearest neighbor element with springs of equal coupling stiffnesses, k_c. An important array characteristic is the ratio of coupling stiffness to element stiffness. This coupling ratio, R, is given by

$$R = \frac{k_c}{k_0} \tag{3.1}$$

Behavior of this system is examined from a wave propagation standpoint.[202] The lowest possible energy state occurs when the system vibrates with no disturbance of the coupling springs from equilibrium. This is the case of rigid body motion (Figure 3.3, Inset 1), which corresponds to a propagating wave with infinite wavelength, λ. The reciprocal of wavelength is the cyclic wavenumber or spatial frequency [1], $a = 1/\lambda$. Figure 3.3 shows the frequency of system response shapes, f, as a function of the spatial frequency of the responses, expressed in terms of the length of the fundamental unit in our system, d. The frequency of this lowest energy system response (at $a = 0$) occurs at the natural frequency of the isolated spring-mass, f_0. At the opposite extreme, the shortest wavelength allowable in our discretized medium is $\lambda = 2d$. In the case of an infinite chain, adjacent oscillators are at maximum displacement with opposite signs, every coupling spring experiences maximum displacement, and the corresponding spatial frequency represents the highest frequency wave admissible in this system, $a = 1/2d$. The system is a filter with pass band ranging

[1] The spatial frequency (cyclic wavenumber), a, is related to the angular wavenumber, k, used in acoustics such that $k = 2\pi a$. In other words, a is to k as f is to ω.

from f_0 to $f_{\max}$. The dotted gray line $(a < 0, a > 1/2d)$ shows that the response frequencies are actually periodic in a. Other out-of-band waves will be aliased to one of the discrete allowable frequencies in the pass band.

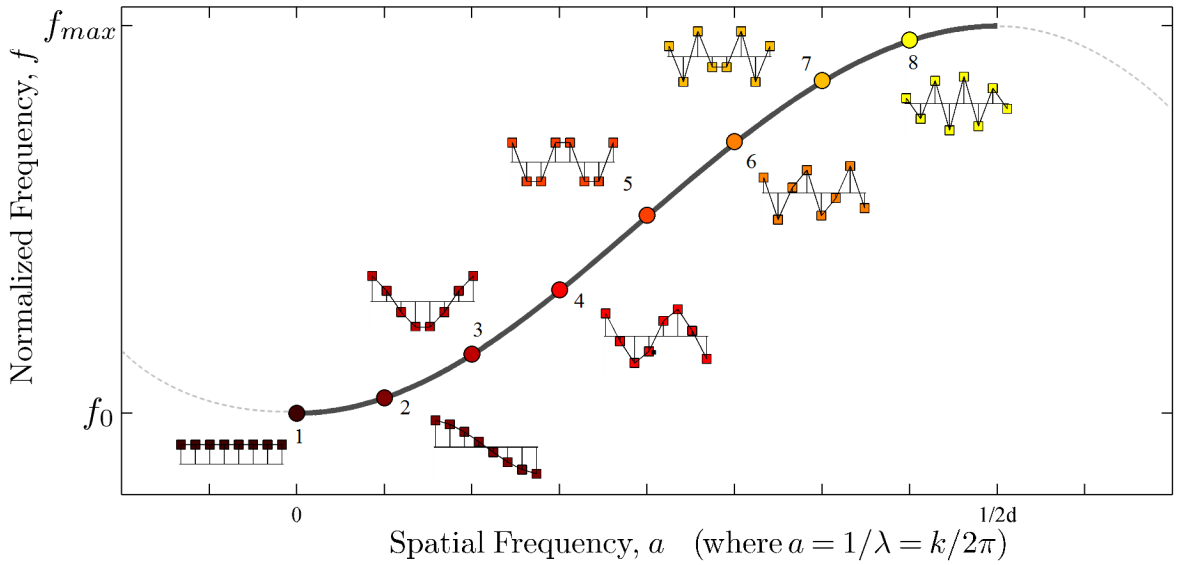

Figure 3.3: Response frequencies as a function of wave spatial frequency, illustrating the pass band of a mechanical filter. Allowable frequencies and corresponding mode shapes in an eight-element linear chain of coupled SDOF oscillators with inter-oscillator spacing d.

A system of N coupled elements has N degrees-of-freedom that translate into N possible responses at the N system resonant frequencies within the pass band. As $N \to \infty$, the system tends toward behavior of a continuous system, which is represented by the black curve in Figure 3.3. For $N < \infty$, the system is a digitized or discrete counterpart to a continuous medium. For our system of eight, the system resonant frequencies are represented by the filled circles in Figure 3.3. Our system is finite with the end oscillators free beyond the end of the chain. Note that the displacements for the end elements in the inset shape for mode eight (yellow) are considerably less than the “maximum and opposite" case in the infinite chain. Unlike in the infinite counterpart, there are not four full waves in the distance of $8d$, but somewhat less than four, indicating a wavelength of

somewhat longer than $2d$ and therefore $a < 1/2d$). The coupling springs are in less than maximal displacement, resulting in the lower corresponding frequency[2].

We return briefly to travelling waves in order to transition the discussion to the topic of disorder. This travelling wave perspective is particularly suited to considering the filtering application of arrays because the primary concern for a filter is the amount of energy transferred with no distortion from the input to the output. A perfectly periodic chain has lossless in-band transmission within the oscillator chain because the impedance does not change across the array; the only boundary is the end of the finite chain. The system can also be considered from a standing wave perspective. The sum of the forward and backward propagating waves create a standing wave pattern. In the perfectly periodic case, the amplitude of the sum of the two waves varies sinusoidally along the elements of the system. The inset mode shapes of Figure 3.3 illustrate this behavior. Each subsequent mode shape is a sinusoid of higher frequency. The next section will discuss the effects of introducing disorder into the system.

3.2 Disorder and Localization in Vibration

The pioneering work in the study of localization began in the 1950's at Bell Laboratories in New Jersey. In 1958, Philip Anderson[3] and colleagues put forth an explanation of electron diffusion in the presence of disorder.[204] One of the early examples of an engineering structure's behavior being investigated from a vibration localization standpoint was the occurrence of rogue blades in turbomachinery.[205] Other research that initiated the formal study of localization phe-

[2]Conversely, in a finite chain of oscillators with the end elements coupled via springs to ground, rigid body motion is impossible (the end springs would stretch), resulting in an upward shift of the system frequencies

[3]Incidentally, his work was initially ignored by the folks in solid and structural mechanics and almost everyone else, but ultimately earned Anderson the 1977 Nobel Prize in Physics.[203] As of this writing, that 1958 paper has been cited over 7000 times, but was cited only 80 times by 1970 and just 600 by 1980.

nomena in mechanical systems used weighted strings, pendula,[206] and coupled SDOF oscillator chains.[207]

Any imperfections or variation in the components of a coupled structure destroys the periodicity. These differences may be due to unavoidable manufacturing variability, inhomogeneities in a material, or disorder created due to adhesion of an analyte of interest on the surface of a cantilever. The dynamics of the structure change as the perfect periodicity is disrupted. Vibration energy no longer propagates evenly, but becomes trapped or localized in certain areas of the structure. The physical resonator variation can be characterized by the standard deviation σ, which may represent mass or stiffness disorder. In this work, we consider only mass variation,σ_m. The ratio of system disorder relative to coupling strength, (σ_m/R), is a generalized indicator of disorder and will factor heavily in later sections of this work. As disorder increases or coupling decreases, energy becomes increasingly localized,[208] and the response shapes will bear less resemblance to the harmonic case. In the extreme, virtually all the vibration energy is held in a single area or discrete element of the system. The cantilever array in Figure 3.4a is a perfectly periodic system responding with an extended mode shape at the fourth system resonance. Disorder in the masses of the cantilevers results in localization such as that shown in Figure 3.4b. In this example, much of the energy is localized in cantilevers 4,5, and 6 with essentially no motion in cantilevers 1, 2 and 8.

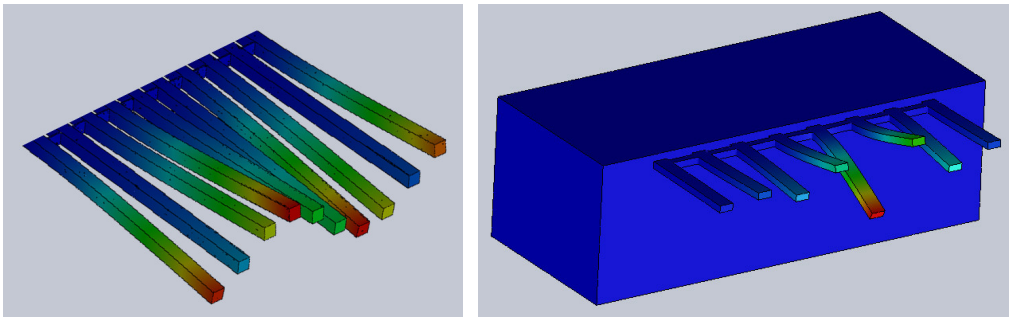

(a) (b)

Figure 3.4: Extended (3.4a) and localized (3.4b) modes

The issue of localization can also be addressed from a traveling wave perspective.[209–213] Given a disturbance incident on one side of a periodic structure, how much energy reaches the other end[214]? As discussed in Section 3.1, a disturbance traveling in a finite medium with no discontinuities or loss mechanisms reaches the end with no attenuation, or loss of vibration energy. The corresponding standing wave is the sum of one forward propagating wave and one backwards propagating wave reflected with no loss or distortion at the end of the array. The first column of shapes in Figure 3.5 illustrates this perfectly periodic case for a system with five oscillators. When any forward propagating wave encounters a boundary between areas of different impedance, the wave is partially transmitted and partially reflected, according to the relative impedance on either side of the boundary.[215] The physical variation in the array—the disorder—creates the impedance mismatches.

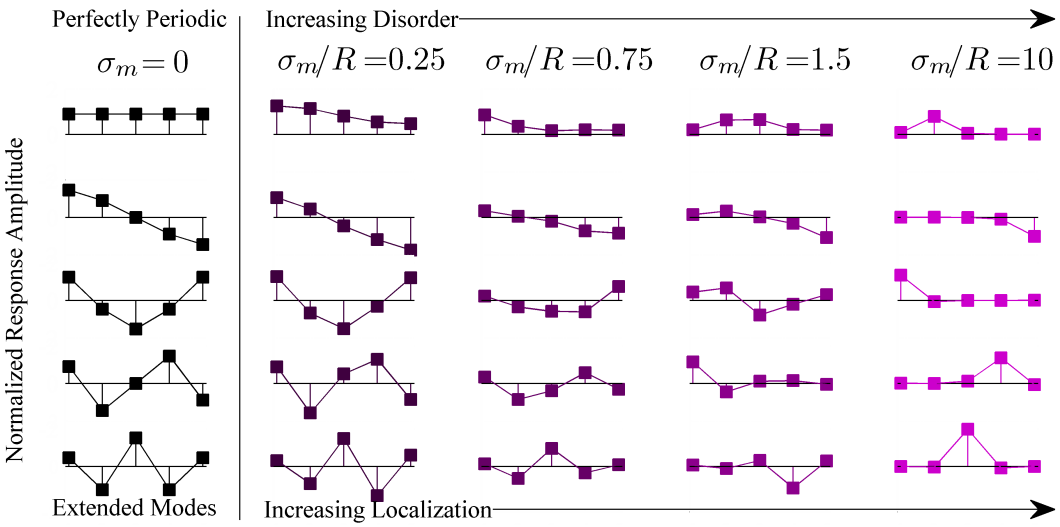

Figure 3.5: Increasing localization occurs with greater normalized mass disorder σ_m/R.

If an impedance mismatch is isolated and trivially small ($\sigma_m/R \ll 1$), very little of the energy is reflected and most is transmitted unaffected to the end of the medium. The standing wave pattern is essentially unchanged and the response remains extended (Figure 3.5, Column 2). Each discontinuity can be considered as a new vibration source, with a forward and backward wave originating at each discontinuity due to partial reflection and transmission. As the magnitude or

number of the impedance mismatches (discontinuities) increase, the number and amplitude of the reflected waves increase. The standing wave pattern (mode shape), which is simply the sum of all the waves in the medium, begins to bear little or no resemblance to the harmonic, ideal case. Each column of responses in Figure 3.5 illustrates the effect of increasing disorder on the resulting mode shape. Values of $\sigma_m/R < 1$ correspond to cases with largely extended modes and little localization. For $\sigma_m/R > 1$, localization becomes more pronounced. The degree of localization distinguishes the nearly- or almost-periodic (a.p.) systems from both the perfectly periodic and the highly disordered. In the almost periodic and lightly coupled case, the energy loss due to localization is on average exponential,[216] giving rise to the concept of equivalent damping due to disorder.[209]

Basically, a set of coupled structures can have responses that fall anywhere on a continuum with fully extended harmonic modes at one extreme to a fully localized, single-element response at the other extreme. The prototype sensor in this work begins with the presumption of fully extended modes. The addition of disorder disrupts those responses. In other words, the detection of the *increase in localization* signals the increase in mass. By constrast, in the work of Glean,[179] the sensor elements are fully localized at the outset. The increase in disorder causes crosstalk between neighboring elements. In this case, the detection of a *reduction in localization* signals the change in mass. It has been demonstrated[196,217] that in the highly sensitive, lightly coupled case (that will demonstrate largely extended modes) the changes in the eigenvectors resulting from a given change in mass are orders of magnitude larger than the concomitant shifts in resonance frequencies.

Localization is the mechanism that allows the detection of mass changes using either amplitude or frequency shift measurements. It is a limiting factor in the work to use micro-and nanoscale structures as filters. Localization also plays a key role in a related class of systems mentioned in Section 2.2.5 and pictured in Figure 3.2b. Collaborators here in the Center for Acoustics, Vibrations and Structures[177,179,180] and a number of other researchers[181,182,185–187] have investigated how the flow of energy within the system is affected by the physical characteristics of the subor-

dinate structures. In the same basic way that disorder creates apparent damping in the linear chain of SDOF oscillators, the addition of numerous small substructures can create apparent damping and dramatically alter the response of the primary structure.[177,180,185,200,201] Glean[195] suggests using changes in the time domain response of such a system to detect changes in resonator mass. Another exciting possibility is the application of these subordinate arrays of oscillators to resonant systems as outlined in Vignola[177] to allow for specific control of desired response characteristics in either frequency or time domain. Study of any aspect of the localization phenomenon, like the sensitivity analysis and experimental investigation in the current work, provides additional scaffolding for those efforts.

3.3 Filters: One- and Two-Dimensional Arrays of Paddle Oscillators

This section describes a set of numerical and experimental studies on the use of one- and two-dimensional arrays of oscillators as mechanical filters.[212,218] Simulation work explores filter performance—the degree of localization—with varying disorder and array size. Two mesoscale prototype filter designs were fabricated and characterized using a scanning laser Doppler vibrometer.

3.3.1 Filters: Simulation

An array of identical coupled mechanical resonators, like that shown in Figure 3.2a, will have a characteristic resonant frequency band, ($\Delta = \omega_2 - \omega_1$), that depends on the coupling ratio, $R = k_c/k_0$. As discussed in Section 3.1, the lower bound of the band is the resonant frequency of an isolated oscillator, given by $\omega_1 = \sqrt{k_0/m}$. The upper bound is given by $\omega_2 = \omega_1\sqrt{1+4R}$.[209] If we consider a normalized case with $\omega_1 = 1$, in an array with light coupling ($R \ll 1$), the upper bound of frequency is given by $\omega_2 \approx 1 + 2R$. In other words, the normalized bandwidth, $\Delta \approx 2R$. Arrays with a smaller coupling ratio have narrower array bandwidth. Likewise, two arrays that have the same coupling ratio, R, will have the same passband. An ideal filter has a high, flat response within

the desired frequency range (minimal passband ripple) and a sharp transition to the low response in the stopband (rolloff). An array with a larger number of identical resonators, N, in that passband has a larger number of peaks packed into the band or, in other words, a higher modal overlap.[177] The closely packed narrow peaks improve passband ripple and out-of-band rolloff.

In a perfect array or any perfectly periodic system, there is no variation in the resonators. The system modes will be harmonic, spatially extended and will occur at frequency intervals as indicated in Figure 3.3. The existence of inevitable variation in mass or stiffness moves this mechanical filter to the nearly-periodic regime. The physical variation causes the changes in response shapes as shown in Figure 3.5 along with corresponding shifts in the system resonant frequencies. The shifts manifest as localization of vibration, which reduces filter performance, as shown in Figure 3.6.

Figure 3.6 illustrates the effect of both σ/R and number of resonators on filter performance. In a linear chain of oscillators (an $N \times 1$ array), localization causes significant filter degradation if $\sigma/R > 1$. Designs with a narrow passband (low R) are more sensitive to variations in the individual resonators.[209] This effect is illustrated in the three blue curves across the top of Figure 3.6, which represent a (5×1) array as oscillator variation (σ/R) increases from 0.25 to 1.5. These σ/R values also correspond to the mode shape representations in Figure 3.5.

Two-dimensional arrays, as pictured in Figure 3.7b, offer multiple paths for energy propagation, resulting in decreased vibration localization.[212] Strong coupling (higher R) along the M dimension (see Figure 3.7c) allows multiple resonators to freely share energy across a wide frequency band (larger Δ), while weak coupling (smaller R) in the other direction allows the array to act as a filter with the desired narrow passband. The M resonators along each strongly-coupled row act together as a single resonator; the variation among rows is lower than the variation among individual resonators by an amount proportional to $\sqrt{M}$. The scatter plot in Figure 3.6 quantifies the reduction in frequency shift as the M dimension increases. Degradation in filter performance is correlated with the shifts in passband resonant frequencies relative to an ideal (perfectly periodic)

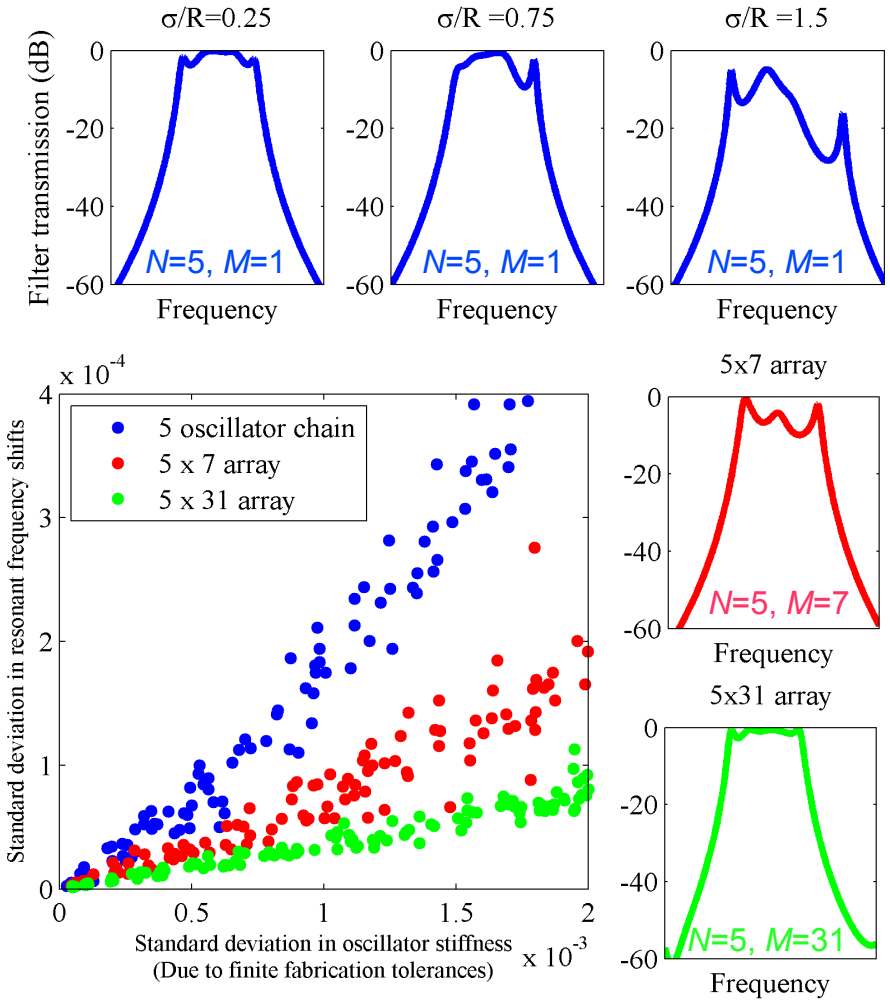

Figure 3.6: Simulation results showing the effects of disorder and array size on bandpass filter performance.

array. For a given level of resonator variation, the passband resonant frequency shifts are smaller for arrays with larger number of resonators.

3.3.2 Filters: LDV measurements and finite element analysis

Two mesoscale prototypes have been used for investigation of the effect of disorder on microscale array performance: a (5×1) and a (5×7) resonator array configuration. These prototypes are cut from 255 μm silicon wafer stock into arrays of 6 mm square paddles. Table 5.1 lists

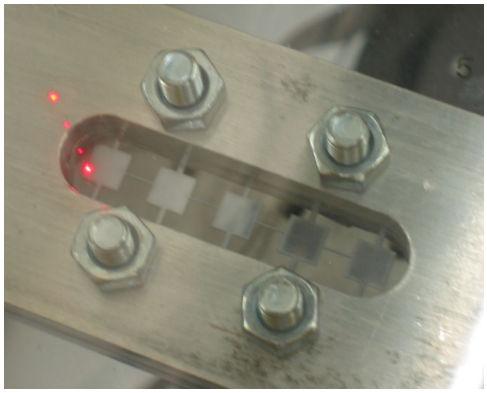

(a) One-dimensional chain of paddle oscillators clamped during LDV measurement.

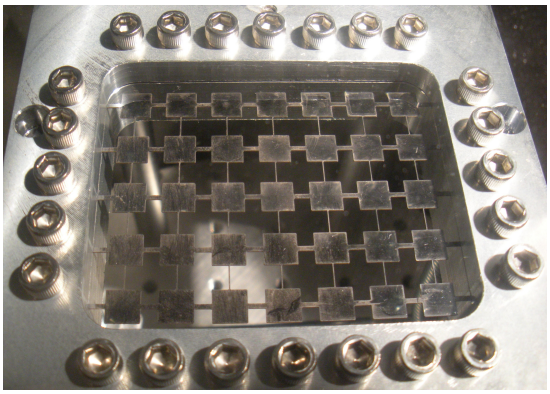

(b) Photograph of two-dimensional paddle oscillator array shown clamped for LDV measurement

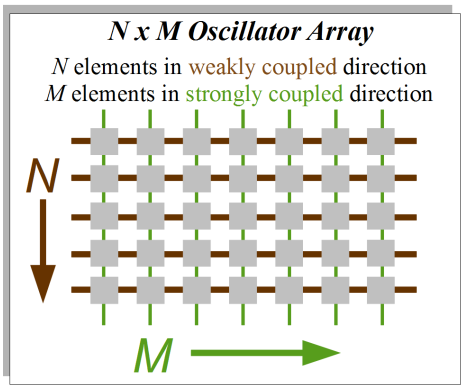

(c) Diagram of strong and weak coupling in a two dimensional array of paddle oscillators

Figure 3.7: Mesoscale filter prototypes: Linear chain and two-dimensional array. In the two-dimensional array, note the thicker horizontal beams in the *M* direction, providing the stronger coupling.

the material property detail. The prototypes are pictured in Figure 3.7. Strong coupling beams are 4.5mm $\times$ 875μm; weak coupling beams are 3mm $\times$ 188μm. The choice of a mesoscale prototype allows comparison of near-perfect arrays to arrays with intentional and controllable resonator variation. SolidWorks software tools (Dassault Systèmes SolidWorks Corp., Waltham, MA) are used for the finite element analysis. A description of the LDV measurement system is included in Section 5.1. The LDV scan resolutions are 1 mm in both the x and y dimensions and 1 Hz in frequency.

Figures 3.8a and 3.8b are frequency spectra generated by exciting the system inertially with a pure tone and sweeping the excitation frequency over the band of interest. The one-dimensional chain of five resonators has five modes in the distinct passband (Figure 3.8a). Likewise, Figure 3.8b shows that the (5×7) array has 35 distinct modes in 7 groups of 5. In the two-dimensional case, driving the 7 (or M) resonators along the edge with the proper relative amplitudes and phases would allow an individual group of 5 modes to be selected, resulting in a single narrow passband.

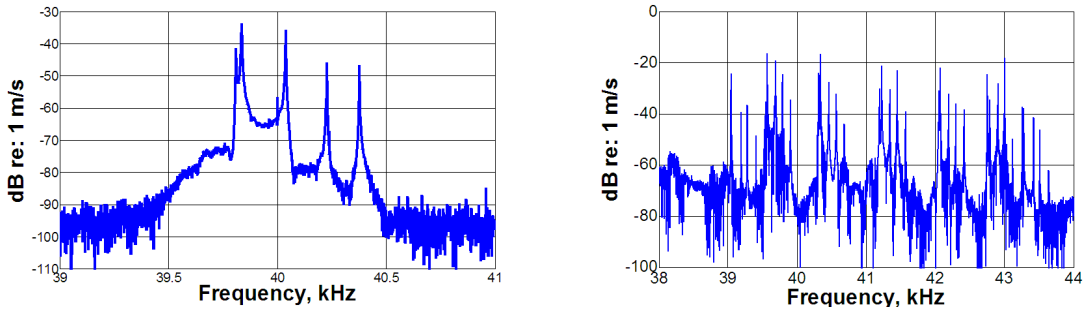

(a) 5×1 array response (b) 5×7 array response

Figure 3.8: Frequency response of a linear chain (3.8a) and a two-dimensional array (3.8b) of paddle oscillators

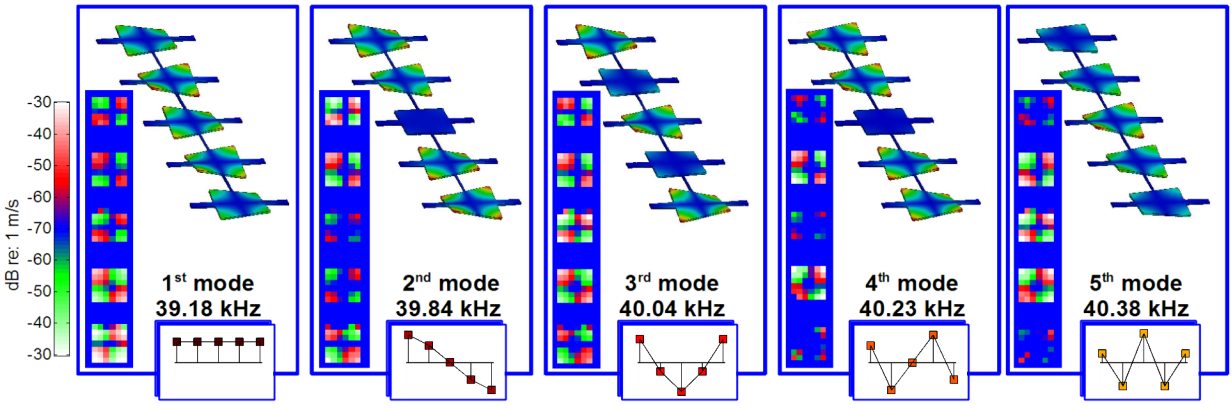

Figure 3.9: LDV measurements and finite element prediction of the first 5 mode shapes in a 5X1 linear array of paddle oscillators.

Figures 3.9 and 3.10 show the predicted mode shapes from finite element frequency analysis paired with spatial frequency plots from an LDV scan of the prototypes. Inset in Figure 3.9

are the simple 5 oscillator mode shapes corresponding to the more complex motion in the paddle oscillators. At first glace, the inset mode shapes may not seem to match the finite element rendering or LDV scans, but the comparison must be made for the coupling beams (that correspond to the coupling springs in a lumped element model), not the motion of the paddles themselves. The torsion in the coupling beams provides the coupling stiffness. In the first mode, neighboring edges of paddle pairs move such that no coupling beams are strained, just as no coupling springs are displaced in the lumped element representation. Similarly, in the 5th mode, adjacent paddles move such that all 5 coupling beams are in torsion, providing maximum stiffness and therefore the highest frequency. In the spatial frequency plots, blue indicates little or no motion; red and green indicate larger relative motion and opposing phase (If red is up, green is down). In the rendering of the finite element results, blue indicates no motion and red indicates maximum motion with direction evident from the deformation. In both the chain and the two-dimensional array, the measured results match expected mode shapes. Note in the second mode of the (5×1) array, the node on the center paddle of the finite element result corresponds to lower amplitude (less color intensity) in the LDV result. In the fifth mode of the(5×1) array, the first and fifth paddle should be low amplitude according to the finite element model and the simple mode shape. The LDV result does indicate lower amplitude for the end paddles. Likewise, the nodal line along the center row of the second mode of the (5×7) prototype is clear in both Figure 3.10d and 3.10c. Correlation of the measured response shapes to the finite element model indicates the ability to fabricate near-perfect arrays at the chosen size scale. These results also demonstrate feasibility of discerning vibration localizations due to introduced disorder at this size scale.

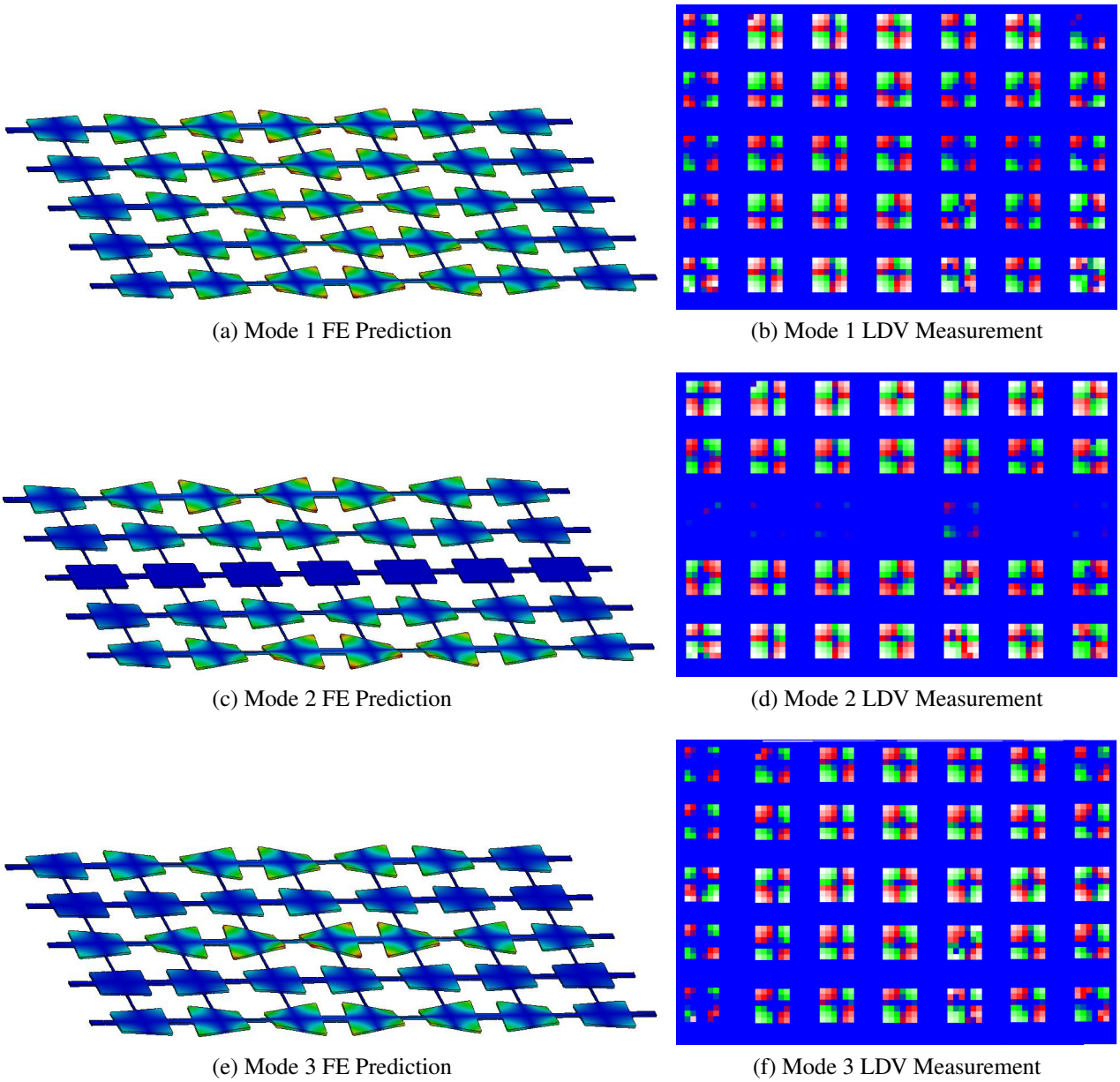

(a) Mode 1 FE Prediction

(b) Mode 1 LDV Measurement

(c) Mode 2 FE Prediction

(d) Mode 2 LDV Measurement

(e) Mode 3 FE Prediction

(f) Mode 3 LDV Measurement

Figure 3.10: Finite element prediction (SolidWorks) and LDV measurement of three modes of a 7×5 element two-dimensional array of paddle oscillators.

CHAPTER 4

PROTOTYPE MASS SENSOR: SYSTEM MODEL, NUMERICAL SIMULATIONS, AND SENSITIVITY TO NOISE

Chapter Introduction

We use arrays of coupled linear resonators and an inverse eigenvalue problem approach to identify the distribution of mass in a resonator array using one or more mode shapes of the system. Numerical simulation is used to explore the sensitivity of the mass identification to measurement noise. The intent of these simulations is to examine the effect of measurement noise on the accuracy of a system mass identification method that uses response shapes as input. In practice, the response shapes will be obtained by measuring the vibration amplitude of each element in a sensor array. In this numerical investigation, the responses are simulated by calculating system eigenvalues and eigenvectors. The eigenvectors are summed with simulated measurement noise, and then used as input to a system mass identification calculation. This process allows for comparison of the original known system mass matrix with that calculated using the simulated noisy measurement. Section 4.1 presents the N-DOF linear model that is the basis of this work and outlines the key assumptions. Section 4.2 details the particulars of the numerical simulation, and Section 4.3 then summarizes the key findings regarding sensor behavior in the presence of measurement noise.

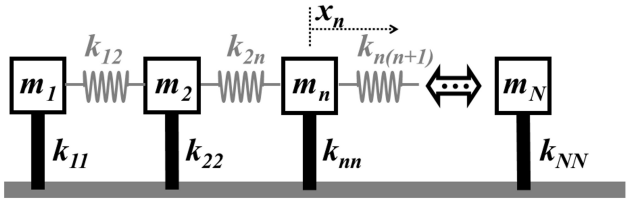

Figure 4.1: N-degree of freedom mass-spring system with inherent element stiffnesses k_{nn} and nearest neighbor coupling elements with stiffnesses $k_{n,n+1}$.

4.1 Basis

We begin with an undamped N degree-of-freedom system of coupled masses, represented by Figure 4.1 and governed by the system of equations, Equation 4.1.

$$\begin{aligned} m_1\ddot{x}_1 &= -k_{11}x_1 - k_{12}(x_1 - x_2) \\ m_n\ddot{x}_n &= -k_{nn}x_n - k_{n-1,n}(x_n - x_{n-1}) - k_{n,n+1}(x_n - x_{n+1}) \\ m_N\ddot{x}_N &= -k_{NN}x_N - k_{N-1,N}(x_N - x_{N-1}). \end{aligned} \tag{4.1}$$

The n^{th} element has mass m_n, stiffness k_{nn}, and is coupled via spring only to the nearest neighbor masses (i.e., those with subscripts $n-1$ and $n+1$). We consider the case of nominally identical resonators, with mass $m_n = m_0$ and stiffness $k_{nn} = k_0$ for all n. Coupling strength is uniform such that $k_{n-1,n} = k_{n,n+1} = k_c$ for all n. Equation (4.1) is nondimensionalized by dividing by k_0 and rescaled in time using the nominal frequency of a single uncoupled resonator, $\omega_0 = \sqrt{k_0/m_0}$. The result can be written in matrix form as $\mathbf{M}_0\ddot{\mathbf{x}} + \mathbf{K}\mathbf{x} = \mathbf{0}$, where the nominal mass matrix $\mathbf{M}_0$ is the identity, $\mathbf{I}$, and the nondimensional stiffness matrix $\mathbf{K}$ is

$$\mathbf{K} = \begin{pmatrix} 1+R & -R & 0 & \cdots & 0 \\ -R & 1+2R & -R & \ddots & \vdots \\ 0 & \ddots & \ddots & \ddots & 0 \\ \vdots & \ddots & -R & 1+2R & -R \\ 0 & \cdots & 0 & -R & 1+R \end{pmatrix} \tag{4.2}$$

with nondimensional coupling strength (coupling ratio), $R = k_c/k_0$.

We account for variations in resonator mass by replacing the nominal mass matrix, $\mathbf{M}_0 = \mathbf{I}$, with a general mass matrix,

$$\mathbf{M} = \mathbf{I} + \begin{pmatrix} \delta m_1 & 0 & 0 \\ 0 & \ddots & 0 \\ 0 & 0 & \delta m_N \end{pmatrix} \tag{4.3}$$

where each δm represents a relative mass variation. Such variations occur due to fabrication tolerances or addition of mass on a resonator during sensor use. Solving the generalized eigenvalue problem, $(-\omega_j^2\mathbf{M}+\mathbf{K})\mathbf{u}_j = 0$, gives the set of N system natural frequencies, ω_j, and corresponding mode shapes, $\mathbf{u}_j$. The N mode shapes can be assembled into a response matrix $\mathbf{U}$.

Given any mode shape, $\mathbf{u}_j$, and associated natural frequency, ω_j, the inverse problem can be solved to recover the system masses. If the system eigenvectors and eigenvalues are known with zero uncertainty, any of the N eigenvector-eigenvalue pairs will yield the system mass matrix with no error. In practice, mode shapes cannot be measured directly but must be deduced from measurements of a system's response. Any measurement of a physical system will contain some amount of noise, and the forced response typically contains contributions from multiple modes.

If the damping in the system is sufficiently light, each resonance of the forced response will be dominated by a single system mode. This occurs when the frequency separation between adjacent resonant peaks is large relative to the width of each peak. For lightly coupled arrays, the over-

all nondimensional bandwidth is approximately twice the nondimensional coupling strength,[209] $\Delta \approx 2R$, so the light damping assumption requires that the resonance quality factor $Q \gg N/2R$. Microscale or nanoscale resonators fabricated from silicon have been demonstrated with sufficiently high Q that this criterion can be met even for arrays with relatively narrow bandwidths.[219–221] For this investigation, we assume light damping and focus on the effects of measurement noise.

4.2 Numerical Simulation Algorithm

This section uses the model described in the previous section to investigate the behavior of arrays used as mass sensors. A range of values of initial mass disorder variation σ_{mass}, array size N, and coupling strength R, are used to generate system responses. The simulated system responses are summed with varying levels of simulated measurement noise and used as input to the inverse problem to calculate the system masses. Section 4.2.1 describes the inverse problem used to calculate system masses. Section 4.2.2 uses a selection of simulation results to present the weighted averaging method used for mass calculation. Section 4.2.3 details the addition of the simulated noise to the measurements and describes the overall simulation algorithm.

4.2.1 Mass calculation: Inverse problem using measured response shapes

Consider a response shape $\mathbf{u}_{\text{noisy}}$ that is an imperfect measurement of a single system mode shape $\mathbf{u}_j$. The use of $\mathbf{u}_{\text{noisy}}$ as input to the inverse problem will result in inaccurate calculation of the actual system mass variations. We distinguish the *calculated* mass variations, Δm_n from the *actual* mass variations, δm_n. The matrix of calculated mass variation calculated using a noisy measurement of a system mode is

$$\Delta\mathbf{M} = \begin{pmatrix} \Delta m_1 & 0 & 0 \\ 0 & \ddots & 0 \\ 0 & 0 & \Delta m_N \end{pmatrix} \tag{4.4}$$

such that

$$\left[-\omega_j^2(\mathbf{I}+\Delta\mathbf{M})+\mathbf{K}\right]\mathbf{u}_{\text{noisy}}=0 \tag{4.5}$$

where each Δm_n approaches the corresponding δm_n in the limit of decreasing measurement noise (i.e., as $\mathbf{u}_{\text{noisy}} \to \mathbf{u}_j$). Because $\Delta\mathbf{M}$ is diagonal, Eq. (4.5) can be rearranged to yield N uncoupled equations for the mass variations:

$$\Delta m_n = \frac{\left([-\omega_j^2\mathbf{I}+\mathbf{K}]\mathbf{u}_{\text{noisy}}\right)_n}{\omega_j^2\left(\mathbf{u}_{\text{noisy}}\right)_n} \text{ for } n=1\ldots N \tag{4.6}$$

where $(\bullet)_n$ indicates the n^{th} element of the vector quantity in parentheses. This calculation can be performed using $\mathbf{u}_{\text{noisy}}$ corresponding to *any* system mode shape $\mathbf{u}_j$ for $j=1\ldots N$. The difference between the true mass of a given oscillator and the calculated mass is the error due to the noise. Since the actual nondimensional mass is given by $1+\delta m_n$ and the calculated mass by $1+\Delta m_n$, the magnitude of the error in the calculation is $|\delta m_n - \Delta m_n|$.

4.2.2 Weighted averaging

The accuracy of Δm_n calculated using a measurement of the j^{th} mode depends strongly on the amplitude of resonator n in the j^{th} mode, since, for a given absolute level of noise, resonators with higher response amplitude have lower relative noise. Figure 4.2 shows system response matrices, $\mathbf{U}$, for perfectly periodic arrays with $N=4,5,6$ and 8 oscillators. Each column represents a response shape $\mathbf{u}_j$. Each pixel in a column represents the oscillator amplitude for that mode. White pixels indicate nodes, or points of zero amplitude while shades of red or green indicate motion in opposing directions. Note that in the $N=4$ and $N=8$ arrays, there are no nodes—amplitudes are moderate throughout the response matrix $\mathbf{U}$. Addition of noise to these responses will have a roughly uniform effect across all oscillators. In contrast, oscillator 3 in the $N=5$ array has amplitude nulls in the second and fourth mode and mode 3 in the $N=6$ array has amplitude nulls on

the second and fifth oscillators. For the $N = 5$ case, calculation of the mass of oscillator 3 using $\mathbf{u}_2$ or $\mathbf{u}_4$ is subject to substantial error with even a small amount of noise. Likewise for the $N = 6$ mass calculations using the third mode. Due to the shape symmetry, perfectly periodic arrays with 2^n elements will naturally be less subject to noise contamination because there are no null points in the response matrix.

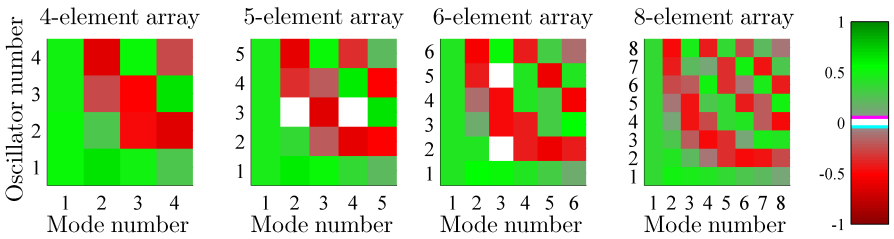

Figure 4.2: Response matrices, $\mathbf{U}$, for perfectly periodic systems with a range of array size, N. Responses $\mathbf{u}_j$ with amplitude nulls are more subject to mass calculation errors due to measurement noise.

As a practical matter, however, perfectly periodic arrays are somewhat of a mythical creature in an experimental environment. Even when, as in our case, extreme care is taken to construct a prototype with virtually no initial mass disorder, the perfect periodicity is disrupted the moment the analyte of interest is introduced into the system. Figure 4.2 depicts perfectly periodic arrays. Recall from the discussion in Section 3.2 that mass disorder in the resonators can have dramatic effects on the response amplitudes. These impacts are shown for varying amounts of normalized mass disorder in Figure 4.3. Significant localization can drop the amplitude of many of the resonators.

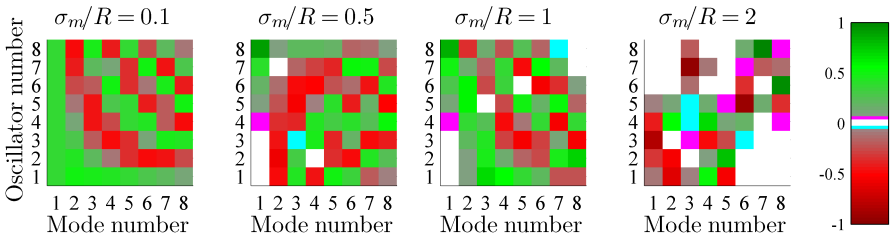

Figure 4.3: Response matrices, $\mathbf{U}$, for a range of normalized mass disorder amounts σ_m/R. Responses $\mathbf{u}_j$ with amplitude nulls are more subject to mass calculation errors due to measurement noise.

Measurement of any quantities near zero in a noisy environment is problematic, and in cases like those in Figure 4.3, several pixels of zero or near zero amplitude contribute proportionally more noise effect to the final mass calculation. A weighted average of results from multiple modes can be used to improve accuracy of the mass calculation. The weighting capitalizes on the fact that high amplitude response occurs on different resonators in different modes. Ideally, all N modes of the system can be used, and $\overline{\Delta m_n}$ is the weighted average mass variation of resonator n. The N different Δm_n values calculated using individual modes $j = 1 \ldots N$ are weighted according to the corresponding amplitude in the response matrix $\mathbf{U}$. A detailed explanation of the weighting method is given in Section 6.1.2. The amplitude based weighting minimizes the impact of the noise. These simulations investigate the effect of both mass disorder and noise level.

4.2.3 Mass calculation with simulated measurement noise

To explore the sensitivity of this mass calculation method to noise, we conduct numerical simulations spanning a wide parameter space for array size, N, coupling ratio, R, standard deviation σ_{mass} of array mass disorder δm, and amount of measurement noise. The basic simulation procedure is shown in Figure 4.4 and parameter values are detailed in Table 4.1.

Table 4.1: Simulation parameter ranges.

Parameter	*Range*	*# of Values*
Mass Disorder, σ_{mass}	10^{-6} to 0.5	30
Noise Level, σ_{noise}	10^{-12} to 0.5	15
	Values	
Coupling Ratio, R	0.1, 0.001	
Array Size, N	5, 10, 25, 50, 100, 250, 500, 1000	
Simulation Iterations, h	100	

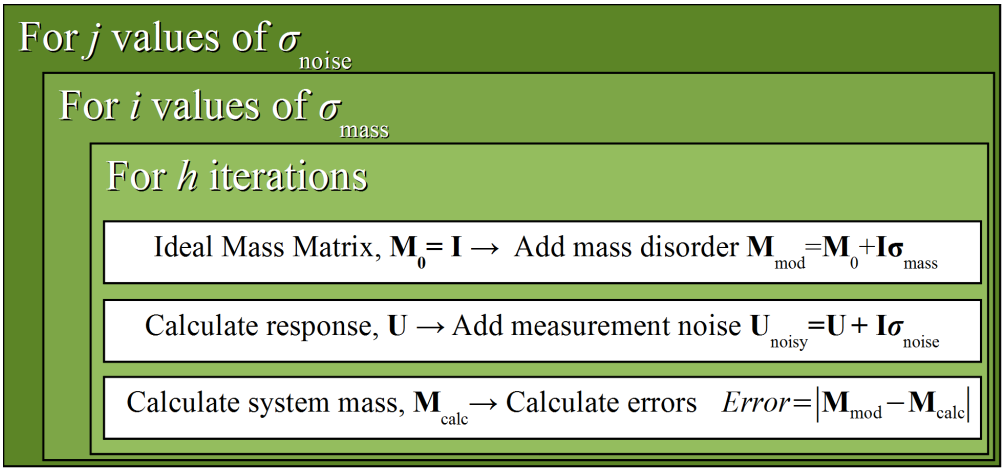

Figure 4.4: Steps of the numerical simulation. Table 4.1 contains detail of the parameters ranges and values used.

The procedure, depicted in Figure 4.4, is as follows. For a given combination of parameters, a mass matrix $\mathbf{M}_{\text{mod}}$ is created using random values for δm_n from a normal distribution with standard deviation σ_{mass}. The generalized eigenvalue problem is used to obtain the matrix of mode shapes, $\mathbf{U}$, and corresponding natural frequencies, ω_j for $j = 1 \ldots N$. In order to simulate measurement noise with a level specified relative to the vibration energy in the array, the modes shapes (columns of $\mathbf{U}$) are each normalized to have unit RMS amplitude, and then each element of $\mathbf{U}$ is perturbed by a random amount $\delta_{\text{shape},nj}$ drawn from a normal distribution with standard deviation σ_{noise}:

$$\mathbf{U}_{\text{noisy}} = \mathbf{U} + \begin{pmatrix} \delta_{\text{shape},11} & \cdots & \delta_{\text{shape},1N} \\ \vdots & \ddots & \vdots \\ \delta_{\text{shape},N1} & \cdots & \delta_{\text{shape},NN}. \end{pmatrix} \tag{4.7}$$

The resulting matrix, $\mathbf{U}_{\text{noisy}}$, is the simulated measurement data representing noise-contaminated approximations of all N system mode shapes obtained from measurements of the system response, the columns of which are then used as input to the inverse problem, Eq.(4.6). The weighted average of mass calculations using all N columns of $\mathbf{U}_{\text{noisy}}$ is a single value $\overline{\Delta m_n}$ for each of the N

resonators that varies depending on the particular random numbers used for δm_n and $\delta_{\text{shape},nj}$. To examine the trends in mass calculation error as functions of σ_{mass} and σ_{noise}, we repeat the process for h iterations and calculate the standard deviation σ_{error} of all $N \times h$ error values. As $N \times h$ becomes large, mean error approaches zero because $\delta_{\text{shape},nj}$ are drawn from a population with zero mean.

The standard deviation of the mass identification errors, σ_{error}, is a function of the particular parameter values used. We define sensitivity to noise as the ratio of the standard deviation of mass identification error to the standard deviation of the simulated measurement noise,

$$\text{Sensitivity, } S = \frac{\sigma_{\text{error}}}{\sigma_{\text{noise}}}, \tag{4.8}$$

and explore how the sensitivity S varies with array size N, coupling ratio R, and standard deviation of mass disorder, σ_{mass}. The sensitivity is the relationship between the accuracy of resonator amplitude measurement and the accuracy of system mass identification.

4.3 Conclusions from Simulation: Sensitivity to Noise

Figure 4.5 shows sensitivity to noise, S, in terms of mass disorder for eight values of array size, N, and two coupling ratios, R. We generalize the results by normalizing the mass disorder by the nondimensional coupling ratio. For low mass disorder, σ_{mass}, or strong inter-oscillator coupling, R, the sensitivity of mass identification is independent of normalized mass disorder level. When the normalized mass disorder levels are sufficiently high, the sensitivity to noise rises with increasing mass disorder.

In nearly periodic systems, disorder (deviation from periodicity) causes energy localization[204] to a degree that depends on the ratio of disorder to coupling ratio.[216] For sufficiently high σ_{mass}/R, the system modes become localized to the extent that only a portion of the array responds with significant amplitude in any given mode. Since measurement noise on *all* resonators contributes

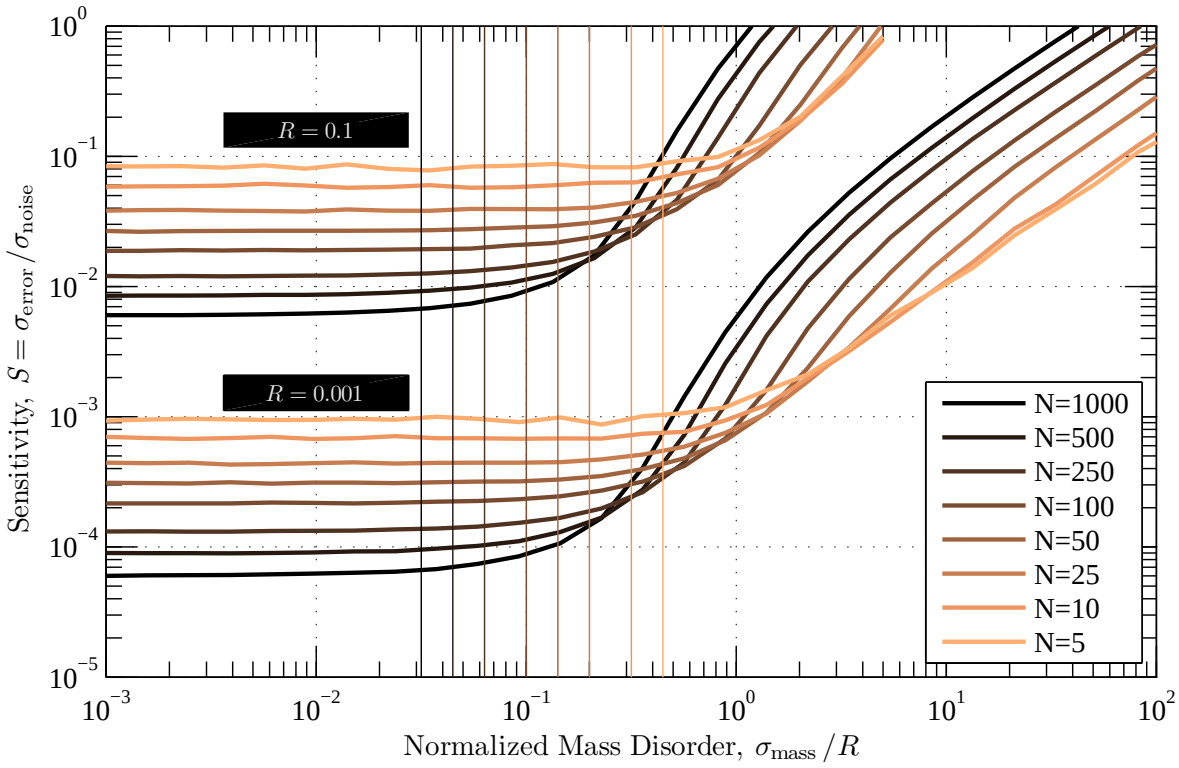

Figure 4.5: Sensitivity of the mass identification technique to measurement noise, as a function of mass disorder. Results are shown for arrays of various size N, and for two values of nondimensional coupling ratio R. The mass disorder (the standard deviation σ_{mass} of the nondimensional resonator masses) is normalized by the nondimensional coupling ratio R, giving a quantity proportional to localization length. The values at which $(\sigma_{\text{mass}}/R) = 1/\sqrt{N}$ are indicated by vertical lines for each value of N.

to errors in mass identification, a large number of resonators with negligible amplitude results in decreased accuracy.

For large N, deviations from periodicity in a nominally periodic array cause spatial amplitude decay that is on average exponential, with a coefficient that is proportional to $(\sigma_{\text{mass}}/R)^2$ as long as damping-related attenuation is relatively small.[222] Thus, the transition from the low-mass-disorder behavior to the behavior characteristic of significant mode localization occurs at a value of (σ_{mass}/R) proportional to $(1/\sqrt{N})$, indicated in Fig. 4.5 by vertical lines.

Thus, the sensitivity to measurement noise is independent of the amount of mass variation as long as the mode shapes are not significantly localized. In this case, large arrays of lightly-coupled resonators have the lowest sensitivity to measurement noise. In cases where mass disorder induces significant localization, smaller arrays are preferable. There is therefore an optimum array size N for any combination of mass disorder and coupling ratio such that the localization length is comparable to the size of the array. Similarly, for any given array size N and level of mass disorder

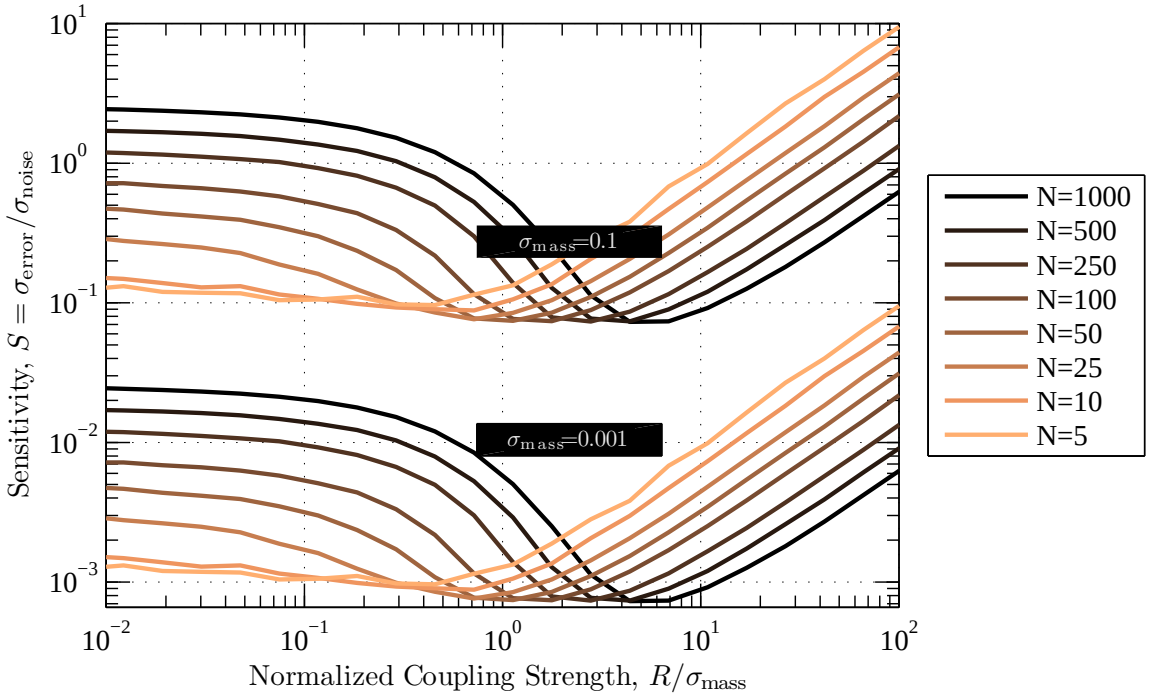

Figure 4.6: Sensitivity of the mass identification technique to measurement noise, as a function of coupling ratio. Results are shown for arrays of various size N, and for two values for standard deviation σ_{mass} of nondimensional mass disorder. The nondimensional coupling ratio R is normalized by σ_{mass}, giving a quantity reciprocal to the abscissa of Fig. 4.5.

σ_{mass}, there is a nondimensional coupling ratio R that will result in the lowest sensitivity to noise. This is illustrated in Fig. 4.6 which shows sensitivity to noise, S, in terms of nondimensional coupling ratio, R, for the same eight values of array size, N, and two values for standard deviation of mass disorder, σ_{mass}. Here, the nondimensional coupling ratio is normalized by the level of

mass disorder. In general, decreasing coupling ratio reduces the sensitivity of mass identification to measurement noise until the optimal value is reached. If N is small, reduction of coupling below the optimal value results in a gradual increase in sensitivity to noise. For larger arrays, the increase in sensitivity to noise becomes more pronounced. The normalized coupling ratio at which the sensitivity to noise is minimized depends on the array size N.

From a practical standpoint, a sensor can be designed with a desired coupling ratio and number of resonators, but mass disorder levels may be limited by manufacturing tolerances or set by the amounts of measurand accumulating on sensor surfaces. The sensitivity to noise can be minimized by selecting an appropriate combination of array size and normalized coupling ratio. The minimum achievable value of sensitivity is a function of the mass disorder level. The model analyzed here assumes variation only in resonator masses. Similar analysis could be used to generalize the results to include variations in elastic properties, including inherent resonator stiffness and coupling ratio.

CHAPTER 5

PROTOTYPE MASS SENSOR: EXPERIMENTAL TECHNIQUES FOR VALIDATION OF MODEL

Chapter Introduction

This chapter begins with a description of the measurement system used to test the prototype sensors in Section 5.1. A description of the two sensor designs and the basis used to select sensor geometry is found in 5.2. General procedures for sensor preparation, addition of mass to the cantilevers, and other experiment details are found in Section 5.3.

5.1 Microscope Scanning Laser Doppler Vibrometer System

The measurement system is a robust, flexible tool for measurement of vibration phenomena over a wide range of size and frequency scales. The system, shown in Figure 5.1, is built around a laser Doppler vibrometer and three orthogonal linear positioning stages. Custom LabVIEW and MATLAB software integrates control of all laser positioning, sample excitation, and data acquisition functions. Figure 5.2 shows a schematic of system components and signal routing. The hardware accommodates target objects up to the size of the 200 mm^2 horizontal stage travel if pressures below atmospheric are not required. For pressure dependent protocols, a vacuum chamber is used, and test specimens may range up to the size of the chamber's 9" optical window (Figure 5.1c). In the downscale direction, the sample size is limited by the resolution of the positioning stages, laser spot size, and an upper limit of 60 MHz acquisition rate. For this work, the prototype

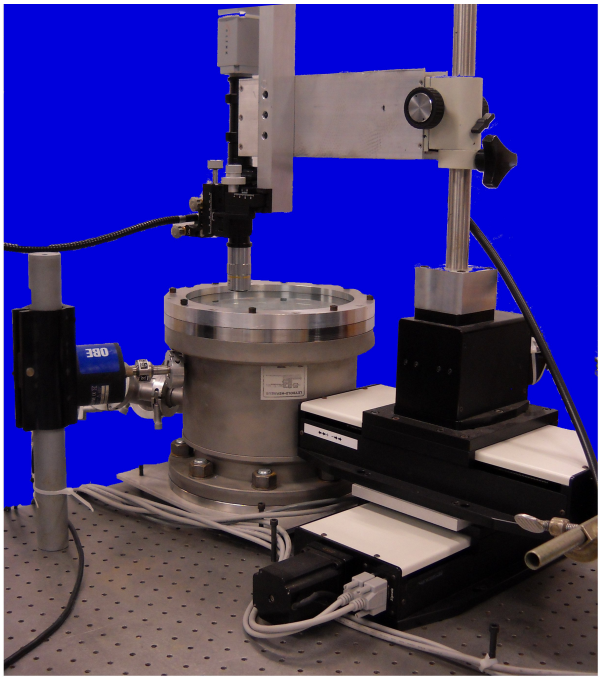

(a) Stages, optics, and vacuum chamber.

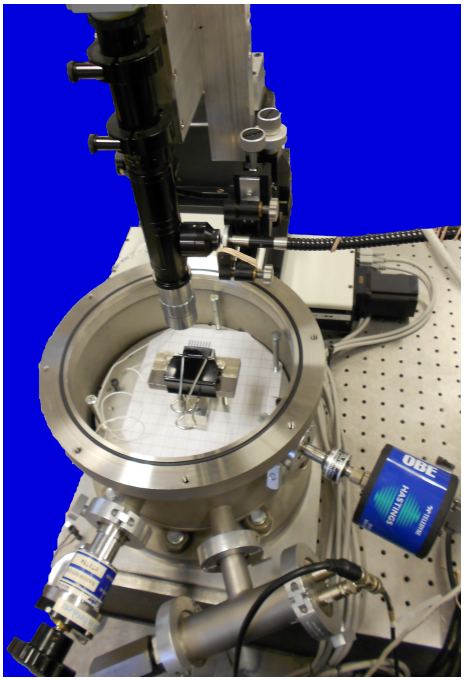

(b) Large array in place.

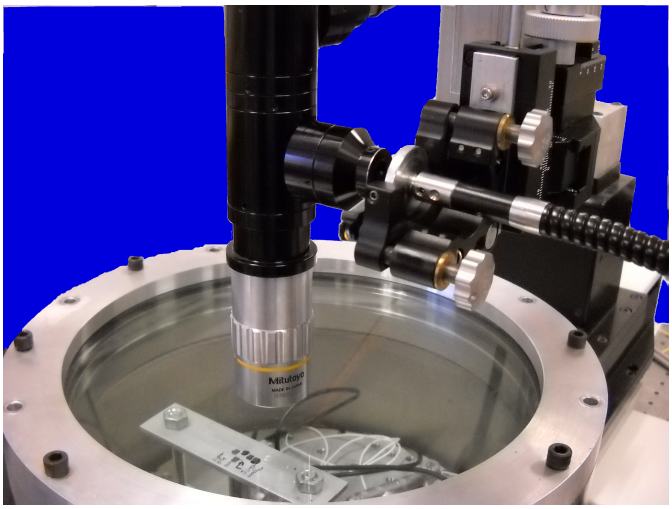

(c) Configured for vacuum measurements.

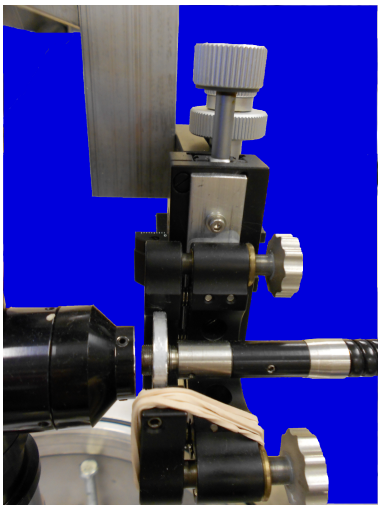

(d) Fine focus, beam steering.

Figure 5.1: Components of the microscope based scanning laser Doppler vibrometer system. 5.1a: Linear positioning stages with optical components positioned over vacuum chamber. 5.1b: Large format sample in place for measurement. Connection to vacuum pump, electrical pass-through and Hastings pressure sensor are visible (CCW around the outside of the chamber). 5.1c: System configured with microscale sample under vacuum. LDV measurements are made through the glass lid. 5.1d: Close view of the custom interface between the vibrometer fiber and the optical stack. The typical threaded connection is replaced by a shortened optical collector and positioning stages to suspend the fiber end and allow for fine tuning of beam focus.

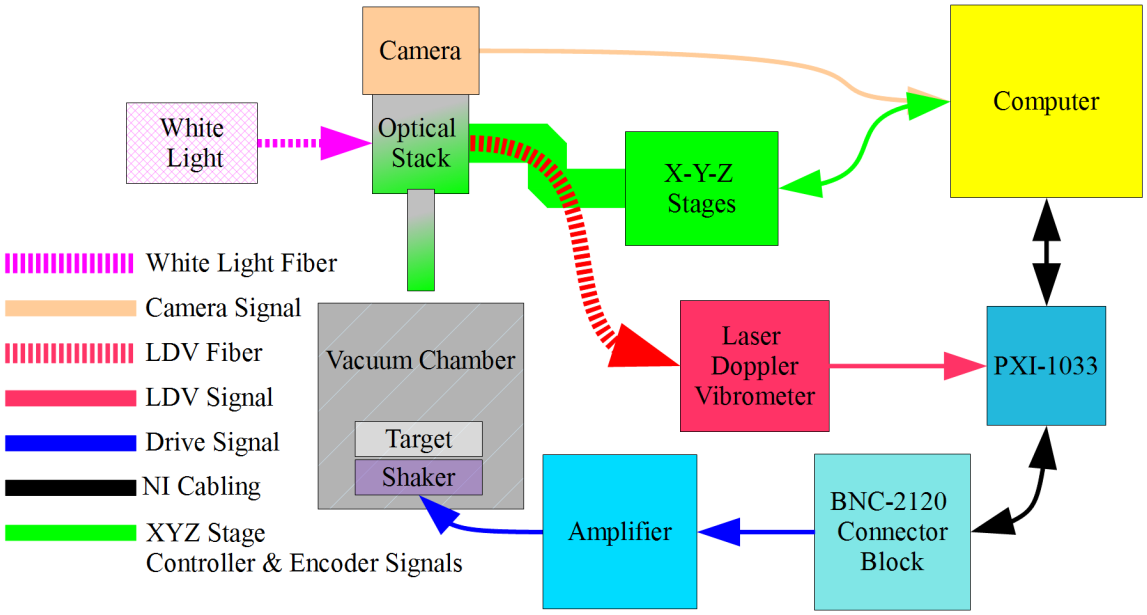

Figure 5.2: Schematic of microscrope scanning laser Doppler vibrometer system

sensors are sized such that frequencies are in the kHz range, and the 2x and 5x objectives create a laser spot size of approximately 10-25 μm. A detailed description of system components and capabilities follows.

5.1.1 Motion hardware

The backbone of the system is the positioning stages (Newmark, Rancho Santa Margarita, CA). Two NLS8 stages with 200 mm of travel provide motion in the horizontal plane, along axes denoted X and Y. Those stages are instrumented with optical linear encoders. Lead screw resolution is 0.1 μm with a stated uni-directional repeatability of 1 μm for the screw and 0.2 μm for the encoder. The lift stage is an NVS-12, which has a 25 mm travel range with 20 nm resolution. An NSC-G4-E motor controller with an RS-232 connection to a computer is used via the LabVIEW software to control stage motion. See Figure 5.1a.

5.1.2 Optical hardware

An OFV-3001 Vibrometer Controller and OFV-512 Fiber Interferometer (Polytec GmbH, Waldbronn, Germany) are the vibration measurement components of the system. An Infinitube dual port system (Edmund Optics, Barrington, NJ), a Fiber-Lite PL-800 illuminator (Dolan-Jenner, Boxborough, MA), and a selection of objectives from 2x to 50x (Mitutoyo, Aurora, IL) are the remainder of the optical system components. A PL-B776U camera (PixeLINK, Ottawa, ON) allows microscope image capture and/or video concurrent with LDV measurements. An additional camera (DCS-900 webcam, D-Link, Fountain Valley, CA) is mounted at a fixed location above the vacuum chamber to allow for still image capture with a wide field of view and live feed to assist the operator with preliminary positioning for a scan. The interface between the vibrometer fiber and the optical stack is a custom assembly designed to suspend the fiber end in the appropriate location relative to the the collector (Figures 5.1c and 5.1d). The collector (Edmund Optics, 59-721) has been shortened and the fiber end mounted to an assembly of multiple small manual positioning stages that allows for fine control of beam orientation and focus. The assembly includes a U-100A mirror mount (Newport Corporation, Irvine, CA), which holds the modified vibrometer fiber end, and three orthogonal linear stages each with 2-3 cm of travel (Figure 5.1d).

5.1.3 Environment control hardware

The system has several environmental control and monitoring features. The positioning stages and vacuum chamber are secured on a vibration isolation table (Newmark, Irvine, CA). A vacuum chamber and vacuum pump (PC-200, Precision, Winchester, VA) allows for experimental pressures ranging from atmospheric to millitorr levels. A pressure sensor (HPM-2002-OBE, Teledyne-Hastings, Hampton, VA) and thermocouple in the chamber enables pressure and temperature monitoring. Multiple electrical pass-through connections allow for a variety of actuation or sensing configurations inside the chamber. See Figure 5.1b. In this work, a piezoelectric stack actuator (P25/10, Piezosystem Jena, Jena, Germany) is used for sample excitation. See Figure 5.9a.

5.1.4 Signals hardware

National Instruments (Austin, TX) data aquisition hardware is connected to the control computer through a PCIe MXI-Express card. A PXI-1033 chassis contains a PXI-5105 digitizer card, PXI-6251 digitizer card, and BNC-2120 connector block. The PXI-5105 is used for high speed (60 MS/s, 12 bit) acquisition. The PXI-6251+BNC-2120 (1MS/s, 16 bit) serves multiple functions. The analog output capability is used for excitation signal generation, while the lower acquisition speeds are sufficient for monitoring and recording quantities like pressure, temperature, and vibrometer signal strength. The excitation signals are generated using the LabVIEW control software and routed through an amplifier (Model 7600, Krohn-Hite Corporation, Brockton, MA).

5.1.5 System software

A custom LabVIEW software interface provides for centralized control of all motion, data acquisition, excitation, environmental monitoring functions. The single interface allows for synchronized acquisition of LDV and environmental data at individually selected data rates. For example, while sampling an LDV signal at 40 kHz in a scan pattern that takes 4 hours to complete, temperature can be recorded every 5 minutes while pressure can be recorded at 1 Hz. The LabVIEW code operates the system in three modes: a manual motion control mode, a manual measurement mode, and an automated scan mode. The first two modes allow for preliminary testing to tune and confirm parameters used for an automated scan. Manual motion mode allows the user to move the stages to desired coordinates as well as change the motion profile (speed and acceleration) of the stages. Manual measurement mode is used for adjustment of vibrometer settings, data acquisition parameters, and selection of the excitation waveform.

Additional MATLAB software complements the LabVIEW to accomplish several other tasks. One tool writes excitation waveforms that can be adjusted with a wide array of parameters including frequency range, duty cycle, amplitude, duration, windowing, and excitation type (chirp, band-limited noise, tone, etc.). Another tool generates the list of motion instructions for the stages,

referred to in this work as path files, based on the desired scan geometry and resolution. Yet another tool maps the vibrometer signal strength over a particular area of interest, allowing optimization of the selected measurement locations. The MATLAB and LabVIEW software are complementary and, taken together, simplify the design and execution of complex LDV scans.

5.2 Prototype Mass Sensor Design

This section first details the materials used for prototype production. The remainder of the section discusses the basis for the design geometry. In Section 5.2.2, a mass-spring model is used to formulate an expression for the expected coupling ratios based on the array geometry. This expression is used to choose array designs with a range of coupling ratios. The array design considerations and final array drawings are included in Section 5.2.3.

5.2.1 Sample material

Two prototype sensor designs were fabricated. Both array designs were fabricated from silicon wafer stock with an IR ($\lambda = 1064nm$ wavelength) laser table with high precision X-Y stages (Laserod, Torrance, CA). Stock for the first set of sensors was 255 μm thick single-side polished wafer manufactured by Mitsubishi with characteristics summarized in Table 5.1[1]. The second prototype is a larger overall design and is cut from stock with a 500 μm thickness. The increase in scale is intended to reduce the relative magnitude of dimensional variation from manufacturing imperfections.

[1]This 255 μm silicon stock is also used to manufacture the coupled paddle array oscillators discussed in Section 3.3

Silicon Wafer Specifications	
Manufacturer:	Mitsubishi
Orientation:	<111>
Diameter:	100 mm
Thickness:	255 & 500 μm
Resistivity:	0.1-0.16 Ω·cm
Grow Method:	Czochralski
Dopant:	Phosphorus
Density:	2.33 g/cm^3

Table 5.1: Properties of the silicon stock used in manufacture of the cantilever arrays.

5.2.2 Planar cantilever array coupling ratio

This section details the derivation of an equation that represents the coupling ratio, R, for a planar array of coupled cantilever beams connected by smaller coupling beams as shown schematically in Figure 5.3. The corresponding mass-spring system model is shown in Figure 5.4. In order to relate the geometry, material properties, and location of the coupling beams shown in Figure 5.3 to a representative coupling stiffness k_c in the mass-spring model, we consider the vibration energy such that the model mass displacement y corresponds to cantilever tip displacement w. We assume a perfectly periodic mass spring system in which coupling stiffnesses, element stiffnesses, and masses are equal. Referring to Figure 5.4, we define these system parameters such that for coupling stiffness $k_{12} = k_{n(n+1)} = k_c$, for element stiffness $k_{11} = k_{nn} = k_0$, and for mass $m_1 = m_n = m_0$. We scale the model element mass m_0 and element stiffness k_0 values to match the physical system. The model coupling stiffness parameter k_c (and resulting coupling ratio $R = k_c/k_0$) can then be found by considering the effect of a coupling beam as a function of its stiffness and the location x_c at which it is attached to the cantilever. This approach is described in detail here.

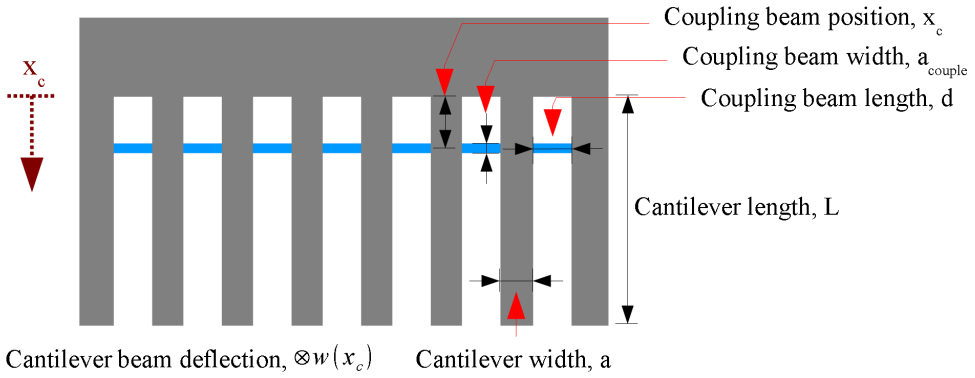

Figure 5.3: Schematic of an eight cantilever array with small coupling beams (shown in darker blue) near the base of the cantilevers. The nomenclature shown is used for the coupling ratio derivation in Section 5.2.2

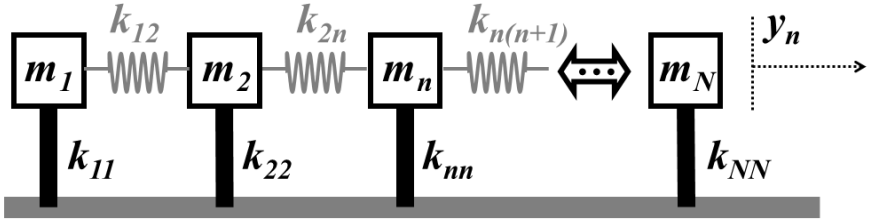

Figure 5.4: Mass spring system. Each of the n masses, m_n, undergoes displacement y_n and has an inherent element stiffness k_{nn}. Coupling stiffness between elements is $k_{n(n+1)}$. For this case the system is assumed to be perfectly periodic such that $k_{12} = k_{n(n+1)} = k_c$, $k_{11} = k_{nn} = k_0$, and $m_1 = m_n = m_0$

Energy of cantilever beam in fundamental flexural vibration

In general, the fundamental flexural mode of a cantilever can be modeled by any mass-spring system for which k/m is the square of the cantilever's fundamental natural frequency. We specifically scale k and m so that the vibration energy in the model matches that of the physical system. Generally, beam deflection is given by Equation 5.1 and velocity is given by Equation 5.2. In these expressions, A is the vibration amplitude and ψ is a given response shape.

$$w(x,t) = A\psi_n(x)sin(\omega_n t) \tag{5.1}$$

$$\dot{w}(x,t) = \omega_n A\psi_n(x)\cos(\omega_n t) \tag{5.2}$$

For a cantilever beam with width a, thickness b, and length L, and density ρ, the kinetic energy is given by

$$\begin{aligned} T_{beam} &= \frac{1}{2}\int_0^L \rho ab\dot{w}^2\,\mathrm{d}x \\ &= \frac{1}{2}\rho ab\int_0^L \dot{w}^2\,\mathrm{d}x \\ &= \frac{1}{2}\rho abA^2\omega_n^2\int_0^L \psi_n^2\,\mathrm{d}x \end{aligned} \tag{5.3}$$

From Ginsberg,[223] expressions for natural frequency and mode shape for a cantilever beam are given by

$$\omega_n = \sqrt{\frac{EI}{\rho AL^4}}\alpha_n^2 \tag{5.4}$$

$$\psi_n(x) = \left[\sin\frac{\alpha x}{L} - \sinh\frac{\alpha x}{L}\right] + R_n\left[\cos\frac{\alpha x}{L} - \cosh\frac{\alpha x}{L}\right] \tag{5.5}$$

where $I = ab^3/12$ is the cross sectional moment of inertia of the cantilever. We consider the first mode, in which $\alpha_1 = 1.8751$ and therefore

$$R_1 = -\left[\frac{\sin\alpha + \sinh\alpha}{\sin\alpha + \sinh\alpha}\right] = -1.3622 \tag{5.6}$$

If the amplitude, A, is presumed to be unity, the response at the cantilever tip is

$$\psi_1|_{x=L} = [\sin\alpha - \sinh\alpha] + R_1[\cos\alpha - \cosh\alpha] = 2.7244 \tag{5.7}$$

To instead normalize tip displacement to unity, the amplitude must be given by

$$A = \frac{1}{\psi_1|_{x=L}} = 0.367 \tag{5.8}$$

Relating the corresponding elements

We consider a model in which the displacement, y, of the mass in the mass-spring system corresponds to the displacement of the tip of a cantilever, $w(L)$. For sinusoidal motion of a single element in the model that has displacement amplitude, y , the element velocity has amplitude ωy. The kinetic energy in a single model element is then $\frac{1}{2}m\omega^2 y^2$. As shown in Equation 5.8, when displacement amplitude $A = 0.367$, the cantilever tip displacement $w(L)$, and corresponding model displacement y, are both unity. Equation 5.9 relates the mass-spring energy on the left to that of the cantilever (from Equation 5.3) on the right.

$$(\text{mass}-\text{spring}) \qquad \frac{1}{2}m\omega^2 y^2 = \frac{1}{2}\rho abA^2\omega_n^2 \int_0^L \psi_n^2 \, \mathrm{d}x \qquad (\text{cantilever}) \tag{5.9}$$

$$m = \rho ab(0.367)^2 \int_0^L \psi_n^2 \, \mathrm{d}x \tag{5.10}$$

By numerical integration:

$$m = 0.25\rho abL \tag{5.11}$$

The mass spring must have the same natural frequency as the fundamental mode of the cantilever, ω_1. It follows that the corresponding spring constant k is given by:

$$k = \omega_1^2 m \tag{5.12}$$

In the mass-spring model, each coupling stiffness k_c is a spring whose deflection is the difference between the displacement of adjacent elements $(y_{n+1} - y_n)$. In the physical system, however,

the coupling beams are attached not to the cantilever tips, $x = L$, but to a location x_c closer to the cantilever root. The model coupling stiffness k_c must therefore account for the fact that the deformation of the coupling beam is smaller than $(y_{n+1} - y_n)$ by a factor $\psi(x_c)/\psi(L)$.

$$\text{displacement, } q = \frac{\psi(x_c)}{\psi(L)}(y_{n+1} - y_n) \tag{5.13}$$

There are several assumptions at work. We assume that the coupling beams are sufficiently short with respect to the cantilevers that a quasi-static treatment is appropriate. We assume zero slope for both ends of the deformed coupling beam as well as a displacement equal to $w(x_c)$ of the cantilever at the connection point. In other words, the motion of the array cantilevers displaces the coupling beam endpoints by the amount $w(x_c)$ with no rotation. If a section is taken at the midpoint of the coupling beam that has length d, each half-beam can be modeled as a cantilever with length $d/2$. The tip displacement for the half-beam is then equal to half of the overall coupling beam deformation, which is half of the difference between the attachment point deformation $w(x_c)$ of two adjacent cantilevers, and thus half of the quantity q from Equation 5.13. The quasi-static stiffness of a cantilever of length $d/2$ is

$$k = \frac{3EI_c}{(d/2)^3} \tag{5.14}$$

where I_c indicates the cross-sectional moment of inertia of the coupling beam. The elastic modulus E is the same as that of the array cantilevers since the sensor cantilevers and coupling beams are fabricated from a single piece of material. It follows that the force, F_c, exerted on each of the adjacent array cantilevers at the attachment location of the coupling beam (x_c) will be the stiffness (Equation 5.14) multiplied by the displacement (half of q, Equation 5.13).

$$F_c = \left(\frac{3EI_c}{(d/2)^3}\right)\frac{1}{2}\left(\frac{\psi(x_c)}{\psi(L)}(y_{n+1} - y_n)\right) \tag{5.15}$$

Because this force is applied to each array cantilever at location $x = x_c$, it has the same effect on the cantilever as a force $\frac{\psi(x_c)}{\psi(L)}F_c$ applied at the tip ($x = L$). Thus, the coupling beam can be modeled as a spring whose two ends are displaced by y_n and y_{n+1} respectively and whose stiffness is

$$k_c = \left(\frac{3EI_c}{(d/2)^3}\right)\frac{1}{2}\left(\frac{\psi(x_c)}{\psi(L)}\right)^2 \tag{5.16}$$

The coupling ratio, R, is this coupling stiffness k_c divided by the element stiffness k given by Equation 5.12:

$$R = \frac{k_c}{k} = \frac{\left(\frac{3EI_c}{(d/2)^3}\right)\frac{1}{2}\left(\frac{\psi(x_c)}{\psi(L)}\right)^2}{\omega_1^2 m} = \frac{\left(\frac{12EI_c}{d^3}\right)\left(\frac{\psi(x_c)}{\psi(L)}\right)^2}{\omega_1^2\,(0.25\rho abL)} \tag{5.17}$$

Given that $\omega_1 = 1.8751^2\sqrt{\frac{EI}{\rho AL^4}}$, Equation 5.17 simplifies to yield

$$R = \left(\frac{48}{1.8751^4}\right)\left(\frac{I_c}{I}\right)\left(\frac{L^3}{d^3}\right)\left(\frac{\psi(x_c)}{\psi(x_L)}\right)^2 \tag{5.18}$$

5.2.3 Array design

With Equation 5.18 and the material properties of silicon, the effect of changes in array geometry are easily explored. Figure 5.5 shows two plots to illustrate the effect of coupling beam width, length, and nondimensional location along the cantilever on the coupling ratio, R. Both plots consider the same basic array geometry over the same range of coupling beam locations. Figure 5.5a shows multiple curves for different coupling beam lengths (which correspond to different pitches, or spacing between neighboring cantilevers). The shortest coupling beam (black curve) demonstrates the highest coupling. Increasing beam length decreases coupling, though coupling beams must remain sufficiently short to maintain accuracy of the quasi-static bending assumption. Figure 5.5b shows the effect of different coupling beam widths. In this case, the narrowest beam (black curve) has the lowest coupling. As expected, the wider coupling structures stiffen the system.

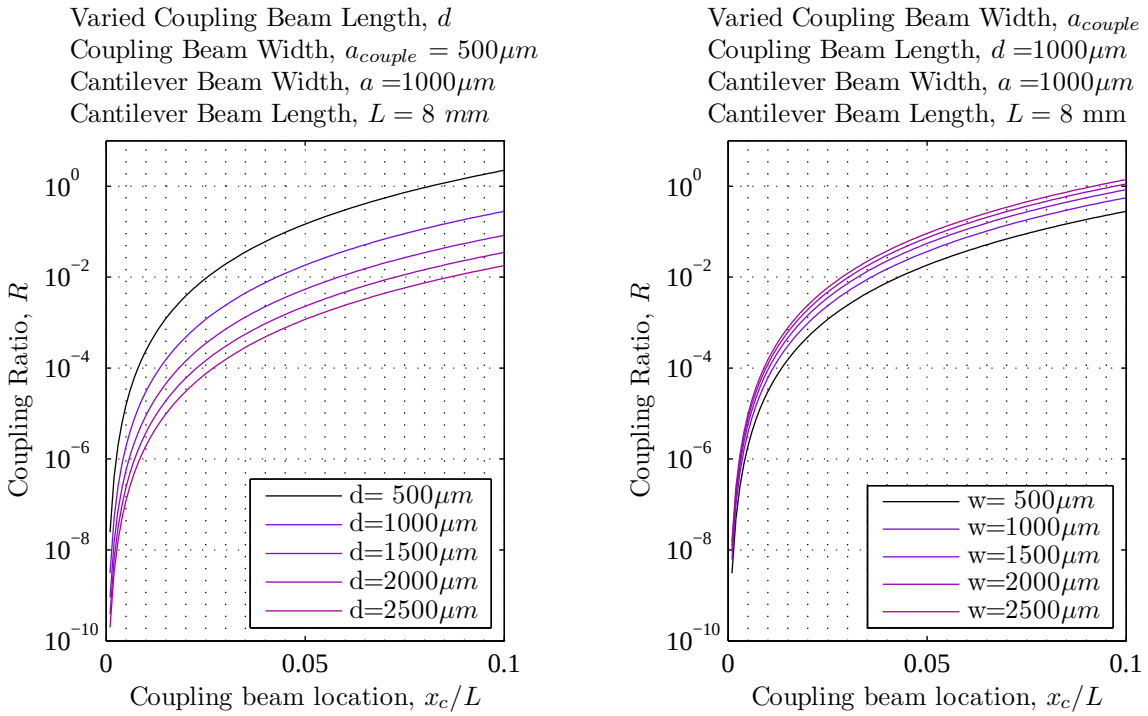

(a) Coupling decreases with longer coupling beams

(b) Coupling increases with wider coupling beams

Figure 5.5: These plots show the coupling ratio predicted by Equation 5.18 for a range of coupling beam locations from zero (the cantilever base) to 10% of the length for different coupling beam lengths (5.5a) or widths (5.5b)

Equation 5.18 was used to determine relative array geometry that would provide a range of coupling ratios that spans multiple orders of magnitude. That information, along with the minimum feature size capabilities specified by the laser fabrication vendor, allowed the conversion of the nondimensional results from Equation 5.18 to prototype array designs with physical dimensions. Both prototypes are millimeter scale. For the testing conditions used in this work (ambient pressure and room temperature), results are expected to generalize downscale to moderate microscale.[219] Beyond that, typical difficulties associated with additional reduction in device size and manufacturing repeatability become a concern.

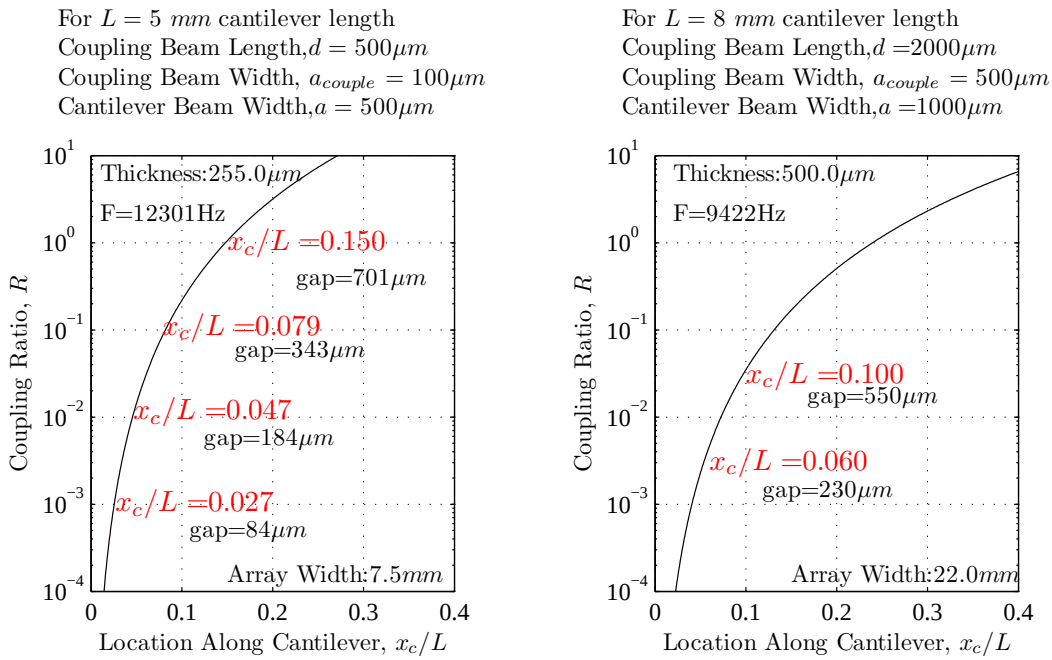

(a) *Small array:* Design points that give coupling strength of approximately $10^{-3}, 10^{-2}, 10^{-1}$, and 1 for given array geometry

(b) *Large array:* Design points that give coupling strength of approximately 0.003 and 0.03 for given array geometry

Figure 5.6: Nondimensional coupling beam locations (x_c/L values in red) and actual feature dimension that provide a wide range of coupling strengths. The gap dimension given is the distance from the cantilever base to the near edge of the coupling beam (the location of coupling beam less half of the coupling beam width, $x_c - 0.5a$).

Figure 5.6 shows the coupling strength curves for the two chosen array geometries–the small array (8 mm wide) in Figure 5.6a and the large array (30 mm wide) in Figure 5.6b. The frequency shown, $\sim$ 12 kHz for the small array and $\sim$ 9 kHz for the large, is the fundamental frequency of a single uncoupled cantilever with the given dimensions. In order to evaluate practicality of possible designs, the nondimensional coupling beam location, x_c/L, is transformed to a gap size instead. The gap dimension takes into account both the coupling beam location and width, to ensure that the design maintains a hole size achievable by the laser cutting process. The four chosen coupling strengths indicated in Figure 5.6a correspond to the four variations in small array design shown in Figures 5.7a to 5.7d. The precise gap dimensions indicated in Figure 5.6 (84, 184, 343, and 701

μm) are used as guidelines for the final selected gap length dimensions of 100, 200, 400 and 800 μm. For the large array (Figures 5.7e to 5.7g), there are three variations–two with coupling beams (at 250 and 1000 μm gap lengths, respectively) and one with no coupling beams. This choice allows an experimental characterization of the lowest practical coupling achievable with a planar array of this basic design, since there will be some amount of unavoidable coupling through the base structure.

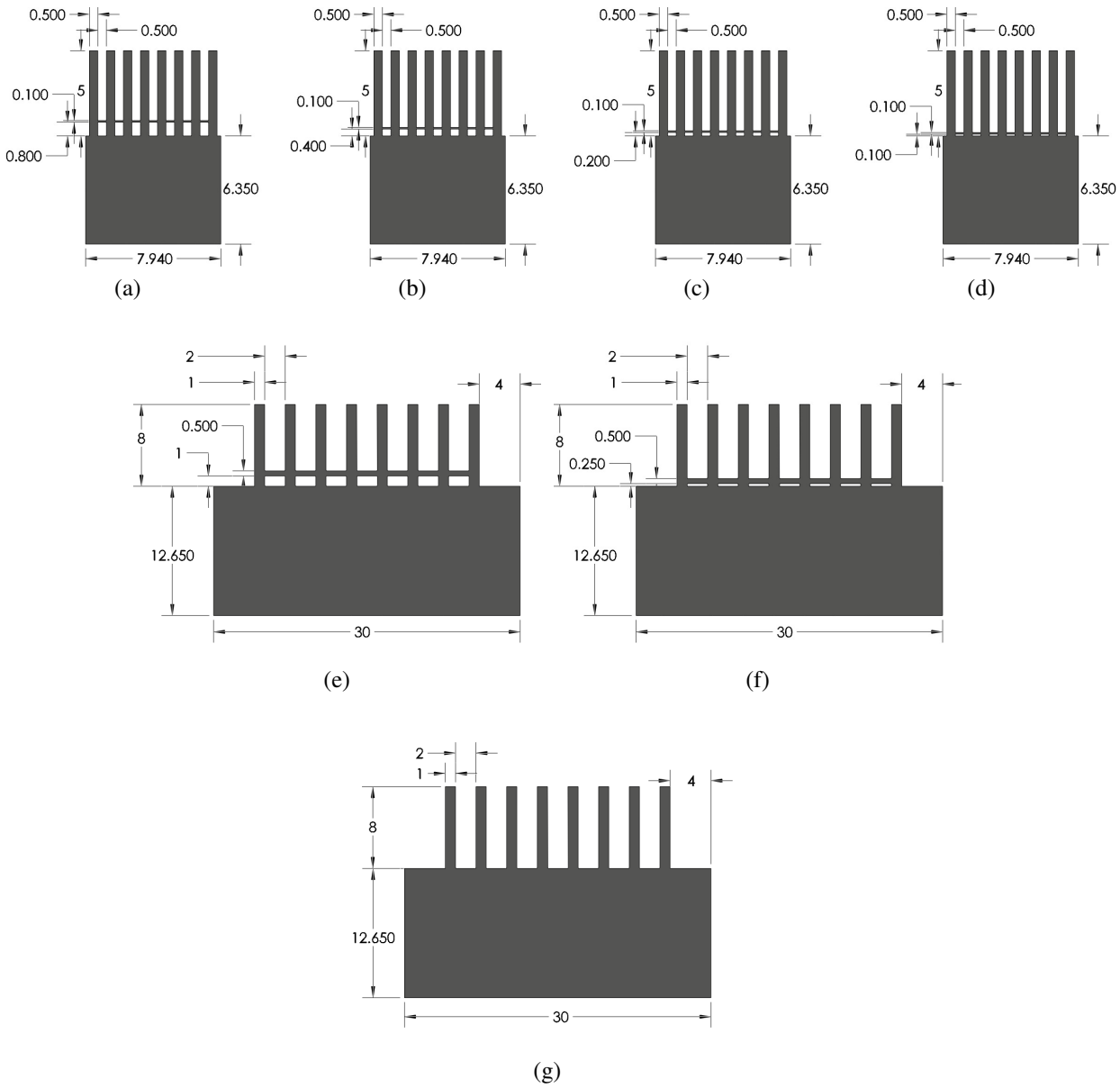

Figure 5.7: Dimensions in mm. Small array design with gap dimensions of 800(5.7a), 400(5.7b), 200(5.7c), and 100 μm(5.7d). Large array designwith the largest dimension between base and coupling beam of 1000μm (highest level of coupling, 5.7e) . The moderate coupling design has a 250 μm gap length (5.7f), and the large design with lowest coupling has no coupling beam(5.7g).

5.3 Sensor Testing Protocols

Section Introduction

This section begins with a clarification of terminology as it will be used in the remainder of this work. A *sensor* is one of the 8-element arrays of cantilevers. The *base* will refer to the portion of the sensor that is not cantilevers, *i.e.*, the silicon material that is the same thickness as the cantilevers and is the attachment point of the cantilevers. The bottom surface of the sensor base is permanently glued to the top surface of a substantially more massive block called an *ingot*. The purpose of affixing a sensor to an ingot is primarily to provide sufficient stiffness to minimize coupling through the attachment. Additionally, the ingot provides a sturdy structure for securing the sensor in the testing fixture and handling the sensor.

A *scan* is defined as a set of LDV measurements made with the sensor in some specified loading state (*e.g.*,"unloaded" or "with one polystyrene sphere on cantilever 2"). The sensor is not moved or modified during a scan. Each scan is made up of a number of individual *measurements* (usually one per cantilever, for a total of 8). The only portion of this work that will address data in a smaller increment than "measurement" will be during the discussion of the data acquisition parameters. In that section, it is acknowledged that each measurement actually consists of some number of individual LDV records that are averaged, and each LDV record in turn contains a large number of individual samples. In any other context in this work, "sample" will serve as a synonym of sensor, rather than refer to individual measured LDV output voltages. Moving back upwards in the size scale, a set of scans will be termed a *study*. A *protocol* consists of executing the same study one or more times on one or more sensors. To summarize with a math analogy, protocol $>$ study $>$ scan $>$ measurement $>$ LDV record $>$ sample. Protocols that are preliminary in nature are designated with numbers. The final set of six protocols are designated with letters: AA, A, B, B2, B3, and E.

Generally, the work flow for testing a sensor is shown in Figure 5.8. A sensor is prepared, a baseline (unloaded) scan is typically completed, the sensor is modified according to protocol

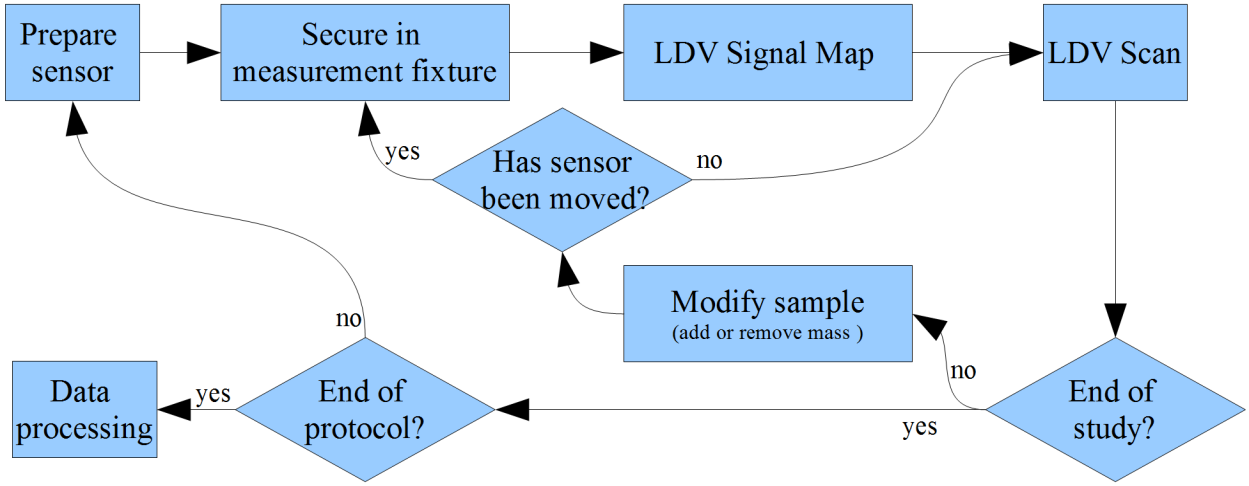

Figure 5.8: Workflow diagram for measurement of the mass sensors.

details, then scanned again in each state specified by the protocol. The sections that follow will detail the various aspects of sample preparation and study execution including initial assembly of the sensors and a summary of study protocols (5.3.1), description of the sensor testing assembly (5.3.1), mapping of vibrometer signal strength (5.3.2), and a description of data acquisition and drive signal parameters (5.3.3). This section concludes with Section 5.3.4, which describes techniques and materials used for mass additions, and includes an examination of the relationship between the amount of added mass and the increase in effective mass of a tip-loaded cantilever.

5.3.1 Sensor descriptions

Several sensor configurations are used in the experiments in this work. A total of four configurations vary in ingot type (aluminum or steel) and array size (small or large). The next section describes the technique for bonding the silicon arrays to the ingot. The tables that follow summarize the characteristics of each of the four types and indicate the sensors used in each measurement protocol. Details of the protocols are addressed in Section 6.2.

Sensor bonding procedure

Every array is rinsed with isopropyl alcohol before being permanently fixed to the ingot. The arrays are attached to the ingots with cyanoacrylate adhesive (Loctite 493). The cyanoacrylate is dispensed on the ingot surface with a pipette for consistency. In order to create a consistent bond between the edge of the ingot and the base of the array nearest the cantilever roots, the volume of cyanoacrylate must be appropriate. There must be sufficient volume to fill the gap between the ingot and array, but not so much that excess overfills the gap along the underside of the cantilever, changing the physical character of the cantilever attachment point. The required volume of cyanoacrylate was optimized by testing various drop sizes and patterns to bond a glass microscope coverslip to a test ingot. For the small arrays, the bonding area is approximately square. A total of 2.5 μL is placed in droplets of 0.5 μL each, with one drop near each corner and one in the center of the bonding area. For the large arrays, the bonding area is more rectangular. Two rows of four 1 μL drops created the best bonding results for the large arrays.

Summary tables: sensor descriptions and protocols

Sensor type 1
Small array, aluminum ingot, cyanoacrylate adhesive

Sensor	**Protocol 1**
	2D scan (for base motion)
g4_03	✓
g4_07	✓
g2_09	✓

Table 5.2: Protocols completed with type 1 sensors. The sensor names identify the sensors in the following way: g*x*_*yy*, where *x* represents gap length (200 μm, 400μm, etc) and *yy* is an ordinal identifier

Sensor type 2
Small array, steel ingot

Sensor	**Protocol 2** Baseline	**Protocol 3** BOE Cleaned	**Protocol 4** Incremental mass	**Protocol 5** Mass on each
g1s1	✓	✓		
g1s2	✓	✓		
g1s3	✓			
g2s1	✓	✓		
g2s2	✓	✓		
g2s3	✓	✓		
g2s4	✓			
g4s1	✓	✓		
g4s2	✓	✓		
g4s3	✓	✓		✓
g4s4	✓	✓		
g4s5	✓	✓		
g8s1	✓	✓		
g8s2	✓			
g8s3	✓	✓		
g8s4	✓	✓	✓	

Table 5.3: Protocols completed with type 2 sensors. The sensor names identify the sensors in the following way: g*x*s*y*, where *x* represents gap length (200 μm, 400μm, etc), s indicates steel ingot and *y* is an ordinal identifier

Sensor type 3
Large array, unsanded steel ingot

Sensor	**Protocol 6** steel sphere $\times 1$
lo01	
md01	
hi01	✓

Table 5.4: Protocols completed with type 3 sensors. Sensor names identify the coupling ratio of the design: *hi* for the arrays with the coupling beam at 1000μm from the base, *md* for the arrays with the coupling beam at 250μm, and *lo* for the arrays with no coupling beam

Sensor type 4
Large array, sanded steel ingot

Protocol:	**AA**	**A**	**B**	**B2**	**B3**	**E**
Sensor	no mass	steel × 4	steel × 4	glass	polystyrene	multiple steel
loa01	✓	✓	✓	✓	✓	✓
loa02	✓	✓	✓			✓
loa03	✓		✓			✓
loa04	✓		✓			
lob01			✓			
lob02			✓			✓
mda01	✓	✓	✓	✓	✓	✓
mda02	✓		✓			✓
mda03	✓		✓			✓
mda04	✓	✓	✓			✓
hia01	✓	✓	✓	✓		✓
hia02	✓		✓	✓	✓	✓
hia03	✓	✓	✓			✓
hia04	✓		✓			✓

Table 5.5: Protocols completed with type 4 sensors. Sensor names identify the coupling ratio of the design: *hi* for the arrays with the coupling beam at 1000μm from the base, *md* for the arrays with the coupling beam at 250μm, and *lo* for the arrays with no coupling beam. The third character (*a* or *b*) designates the assembly batch, and the numerals are an ordinal identifier.

Testing assemblies

All sensors are tested with the same basic hardware that couples the testing assembly to the piezoelectric actuator. A steel interface plate with a slot sized for the ingot is held in contact with the surface of the actuator with two bolts, as shown in Figure 5.9a (small array) and Figure 5.9b (large array). The ingots are held firmly in contact with the interface plate with spring clips (not pictured). A two dimensional LDV scan of three Type 1 sensors shows that resonant behavior of the fixture is not a significant contribution in the frequency band of the sensors. One of the sensors (g4_03) had all 8 cantilevers broken off near the root to be able to compare the case of an ingot+base with no cantilevers to the case of an intact sensor. Another sensor (g2_09) was

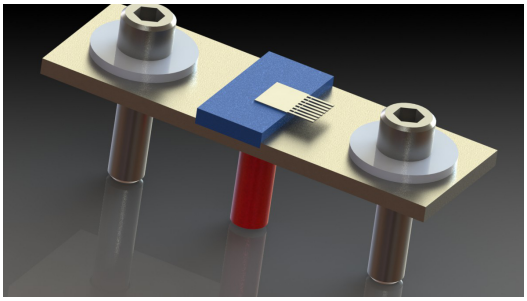

(a) Small array shown positioned in the measurement fixture.

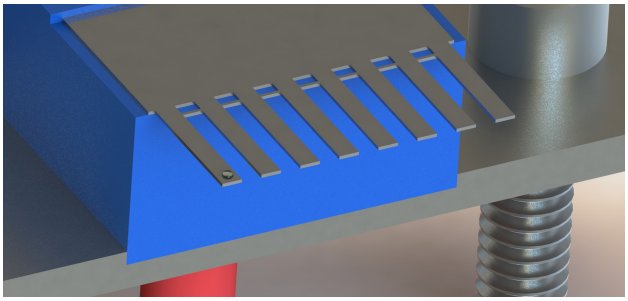

(b) Schematic of the large array in the testing assembly with mass placed on a single cantilever.

Figure 5.9: Testing assembly. Ingot in blue. Piezoelectric actuator in red.

attached to the ingot with additional base overhang to provide another case for comparison. Figure 5.10 shows the results of these measurements. In both sets of frequency response functions (FRFs), the responses measured at the cantilever tips are in gray. The system resonant peaks are clearly visible, and are orders of magnitude larger than the responses measured at the other locations indicated in red, black, or blue. The blue curves correspond to the sensor attached with overhang such that the "Base 1" and "Base 8" measurement locations are not held in place on the ingot but are free to vibrate. The measurement at the back of that sensor with overhang (top plot, blue) is in agreement with the other two cases (top plot, red and black). As expected, in the bottom plot, the motion measured at the "Base 1" and "Base 8" locations shows reduced amplitude peaks matching the first four (or arguably more) system resonances.

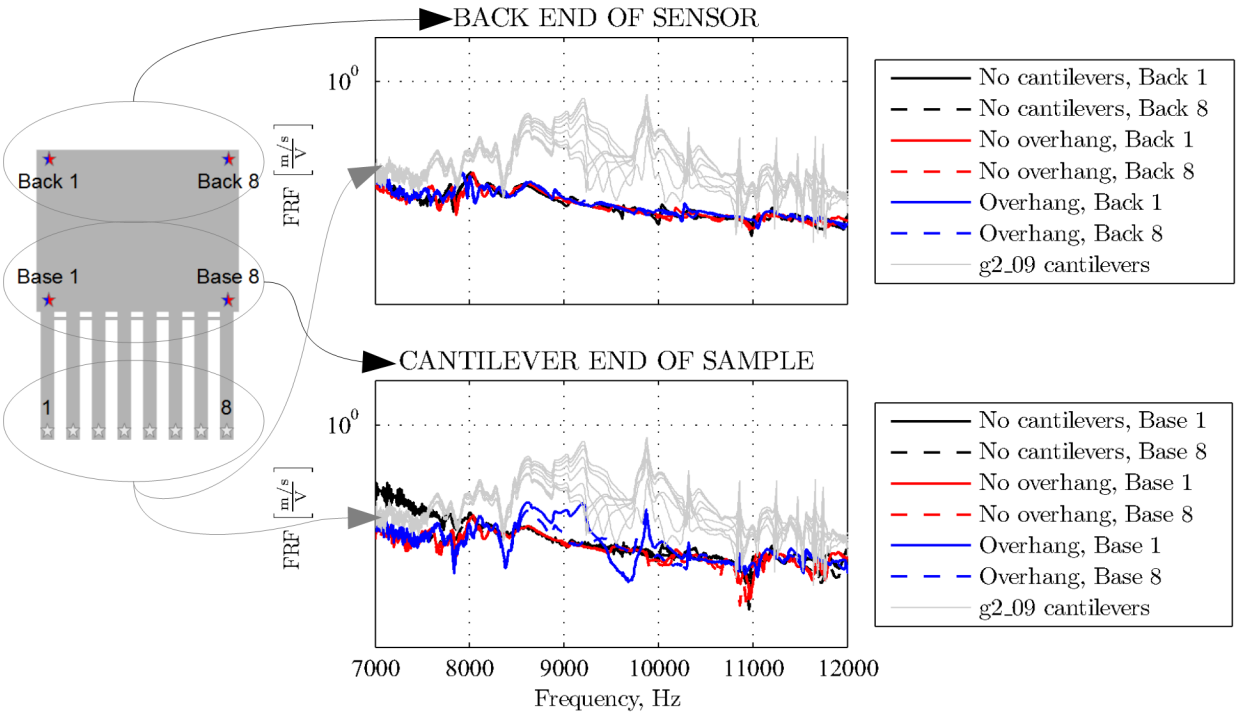

Figure 5.10: Results from Protocol 1. Amplitudes of various locations over the entire sensor surface. The schematic at left shows locations on the sensor measured by LDV to assess the motion of the test assembly compared to that of the cantilevers. The response amplitudes are shown in the plots on the right.

5.3.2 Signal strength mapping procedure

A laser Doppler vibrometer is an interferometer that compares an internal reference beam to a beam that has been reflected from a target surface. One factor that affects the quality of LDV measurements is the proportion of energy incident on the target that is collected on the return. The degree of surface roughness or specularity, target orientation, and even turbulence can contribute to loss of the incident energy. The vibrometer signal strength voltage is an indicator of the proportion of energy return. The automated scan mode of the system is used to record the vibrometer signal strength at each point in a user-defined scan pattern. This set of voltages is a map of signal strength that can be used to select LDV measurement locations. The mapping is a way to ensure that

measurement locations are consistent with respect to the array geometry both when measuring different sensors and when conducting a protocol that requires removing and replacing the same sensor in the testing assembly between scans.

A rectangular scan pattern is defined with sufficient resolution to allow multiple measurements across the width of an individual cantilever. Figure 5.11a shows a typical signal map. The scan pattern measures 10 mm with a spacing of 0.125 mm in the direction across the cantilevers, and 14 mm with a spacing of 0.5 mm in the direction along the cantilevers, for a total of 81×29 locations. Due to the unequal x- and y- dimensions of each pixel, the images in Figure 5.11 are not to scale. The colorbar ranges from black for no detectable signal through red, yellow, and white to the maximum of 5 V. In practice in these types of scans, a signal level of approximately 0.5 V or above produces adequate LDV measurements with minimal averaging. The signal map allows for the precise position of the sensor to be identified with respect to the measurement system stages, thus eliminating the need for highly repeatable manual placement of the sensor in the testing assembly during protocols requiring removal and replacement of a sensor between LDV scans. The signal map is used not only to locate the physical extent of the silicon surface, but also to determine the coordinates of the subsequent LDV measurements. Software allows the scan operator to select measurement points automatically based on a minimum threshold signal level, as shown in Figure 5.11, or manually on a point by point basis. After selection of the desired measurement points, software creates the path file, or list of measurement coordinates, to use for the LDV scan. Figure 5.11 shows data from sensor g2_09, used for the two-dimensional LDV scans of Protocol 1. Figure 5.11b shows the measurement points selected with a threshold signal level of 0.7 V (selected points are white pixels). For the remainder of the studies discussed in this work, the LDV scans are linear with one measurement at the same relative location on each of the 8 cantilevers.

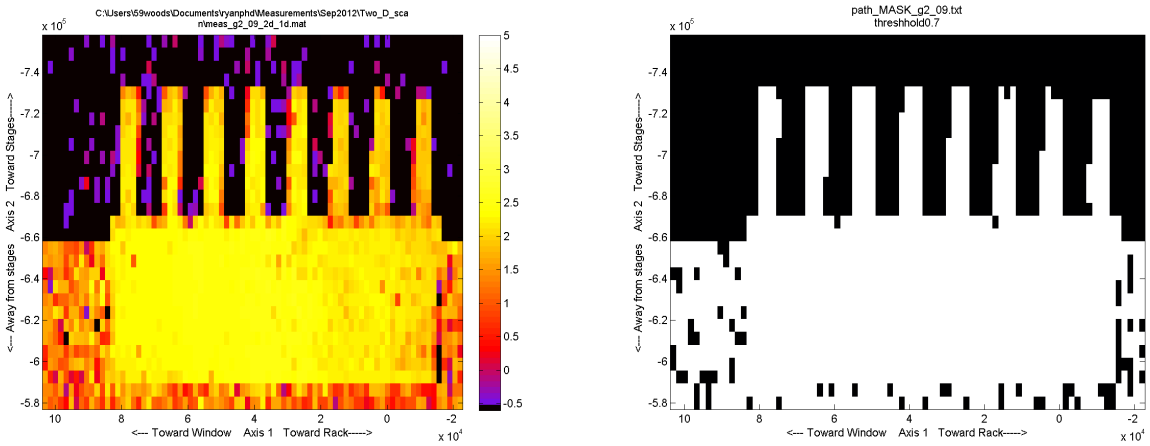

(a) Polytec signal level voltage map (v)

(b) Selected measurement locations

Figure 5.11: A two dimensional scan pattern is used to record the vibrometer signal strength voltages over the face of a sensor. The resulting LDV signal map (5.11a) allows the precise position of the sensor to be identified with respect to the measurement system stages. In 5.11b the measurement locations selected for subsequent LDV measurement (white pixels) are shown for a threshold voltage level of 0.7 V.

5.3.3 DAQ and excitation details

Data acquisition parameters used in the various protocols are summarized below in Table 5.6. A sampling frequency of 100 kHz is used for all protocols, and the excitation in all cases is a frequency modulated (FM) chirp. The choice of frequency content of the chirp differs among the protocols based on the observed ranges of the system responses in preliminary measurements. For example, the chirp band for each sensor used in Protocol 2 was chosen after a manual single point measurement, so as to bracket the observed peak responses. Figure 5.12 shows the actual measured peak frequencies (in color symbols) as well as the upper and lower frequencies of the excitation band (solid black squares) for all of the sensors in type 2. Taken together, these results allowed for selection of a frequency range that would encompass the responses of all of the sensors. For subsequent protocols with the type 2 sensors, a chirp with a 7-20 kHz bandwidth is used. A similar process is used to determine appropriate chirp bandwidth for the remaining work.

Sensor type	Protocol	Description	LDV t_{samp} [s]	LDV N_{avg}	Excitation Band [kHz]	Excitation Duration [ms]	# of studies
1	1	2D scan of base motion	1	5	6-13†	50	1
2	2	baseline	1	10	varied	50	20
	3	HF cleaning	1	10	7-20	5	13
	4	incremental mass	1	10	7-20	5	1
	5	single mass on each	1	10	7-20	5	1
3	6	steel sphere $\times 1$	1	3	7-14‡	100	2
4	AA	baseline	2	5	7-14‡	100	12
	A	350 μm steel $\times 4$	2	5	7-20	100	5
	B	350 μm steel $\times 4$	2	5	9-14	50	14
	B2	glass $\times 7$	2	5	9-14	50	3
	B3	polystyrene $\times 7$	2	5	9-14	50	3
	E	multiple locations	2	5	9-14	50	12

Table 5.6: DAQ and excitation parameters for various study protocols. †‡Nonlinear frequency distributions, as illustrated in Figure 5.15

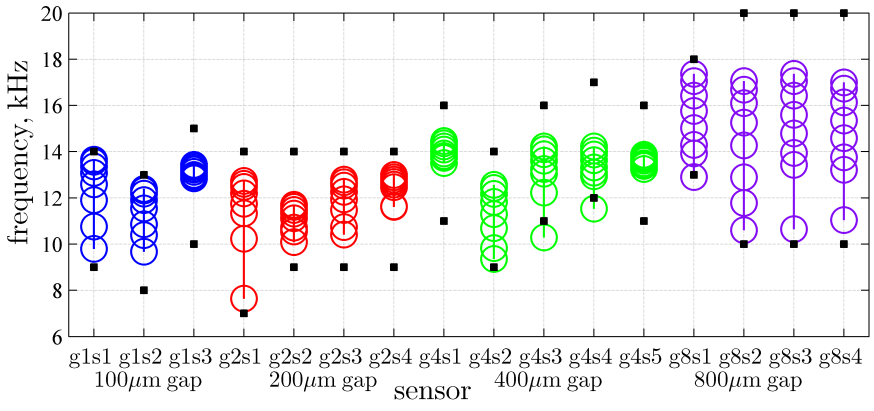

Figure 5.12: Peak frequencies measured in Protocol 2. Excitation frequency range for each individual sensor indicated by the black squares. Excitation bandwidth for additional protocols using this sensor type was selected to be 7-20 kHz, based on the overall range of all sensors.

An observation from the initial measurements of the sensors with the small array design is the significant variation in the bandwidth of the individual sensors, as shown in Figure 5.12. Coupling

strength (and therefore bandwidth) should increase with the larger gap dimension (distance from cantilever root to coupling beam). Significant variation is evident in the bandwidth of the individual sensors, indicative of large variation in the actual coupling strengths of the small array design. The set designed to have the highest coupling (800μm gap) shows the least variation. The bandwidths and fundamental frequency of the remaining three small array designs are highly variable, indicating a larger than intended variation in the actual coupling strengths. This observation motivated the cleaning of the arrays in a HF solution in an attempt to remove any remaining burrs or adhered silicon dioxide remaining from the cutting process. See Section 6.2.3 for additional detail.

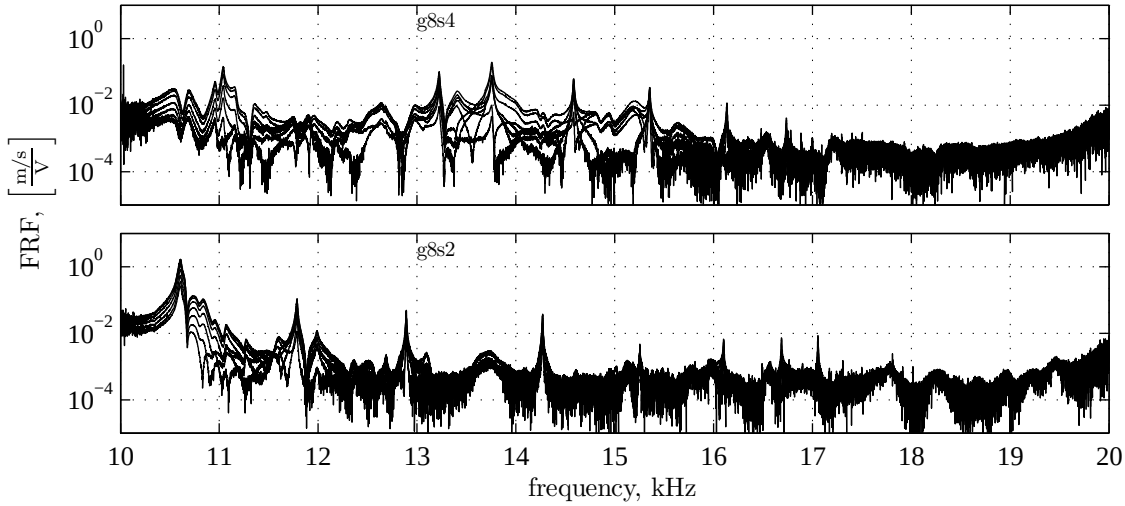

Figure 5.13: Frequency response functions for two sensors in Protocol 2

Two representative FRFs from Protocol 2 are shown in Figure 5.13. There is a distinct difference in the relative amplitudes of the system responses as frequency increases. In both cases, the lower frequency responses have the highest amplitude, however the amplitude of subsequent responses declines more than two orders of magnitude for sensor g8s2. For sensor g8s4, the first three peaks are of rougly comparable amplitude, then decline by slightly more than an order of magnitude for the remainder. In an attempt to ensure response amplitudes that are both above the

noise floor in the higher frequency range and more uniform across the frequency band, nonlinear frequency distributions were used for the excitation chirp profile in some of the subsequent protocols (see Table 5.6).

Figures 5.14 and 5.15 illustrate some of the parameters that define the chirp excitation used in this work. Figure 5.14 shows detail of the duration (5.14, bottom), frequency distribution in time (5.14, upper left), and amplitude spectrum (5.14, upper right) for one of the linear FM chirps. All variations of chirp excitation used in this work have time domain windowing applied, as shown in the bottom plot of Figure 5.14. In contrast, Figure 5.15 shows a nonlinear frequency distribution, with the skew toward the higher frequencies in the band. The intent of the uneven distribution of energy is equalization of the amplitudes of the peaks corresponding to higher order system responses. Ultimately, the mass calculation algorithm depends on relative amplitudes of the eight cantilevers within each response to extract a response shape, so adjusting the relative amplitudes of responses among the system resonances should not compromise mass calculations, as long as each peak is resolvable from the noise.

5.3.4 Addition of mass to cantilevers

Mass is added to the cantilevers for testing by one of two methods: dispensing controlled volumes of solution containing polystyrene microspheres or manual placement of individual dry spheres. The microsphere solution has a known weight-to-volume ratio. The desired mass is added by pipetting a given volume of solution onto the cantilever and evaporating the solvent. A radiant heat source (100 watt light bulb) is placed approximately 20 cm above the sample for gentle heating to ensure thorough evaporation. A variety of dry spheres were used in different protocols: polystyrene, glass, and steel of different diameters. The dry spheres are placed manually with the following technique. A dilute sugar solution (concentration of ~ 0.01 g/mL) is used to secure the spheres to the silicon cantilever surface. A drop (approximately 0.1 μL) of the sugar solution is placed in the desired location near the free end of the cantilever. A syringe with a 31 gauge needle

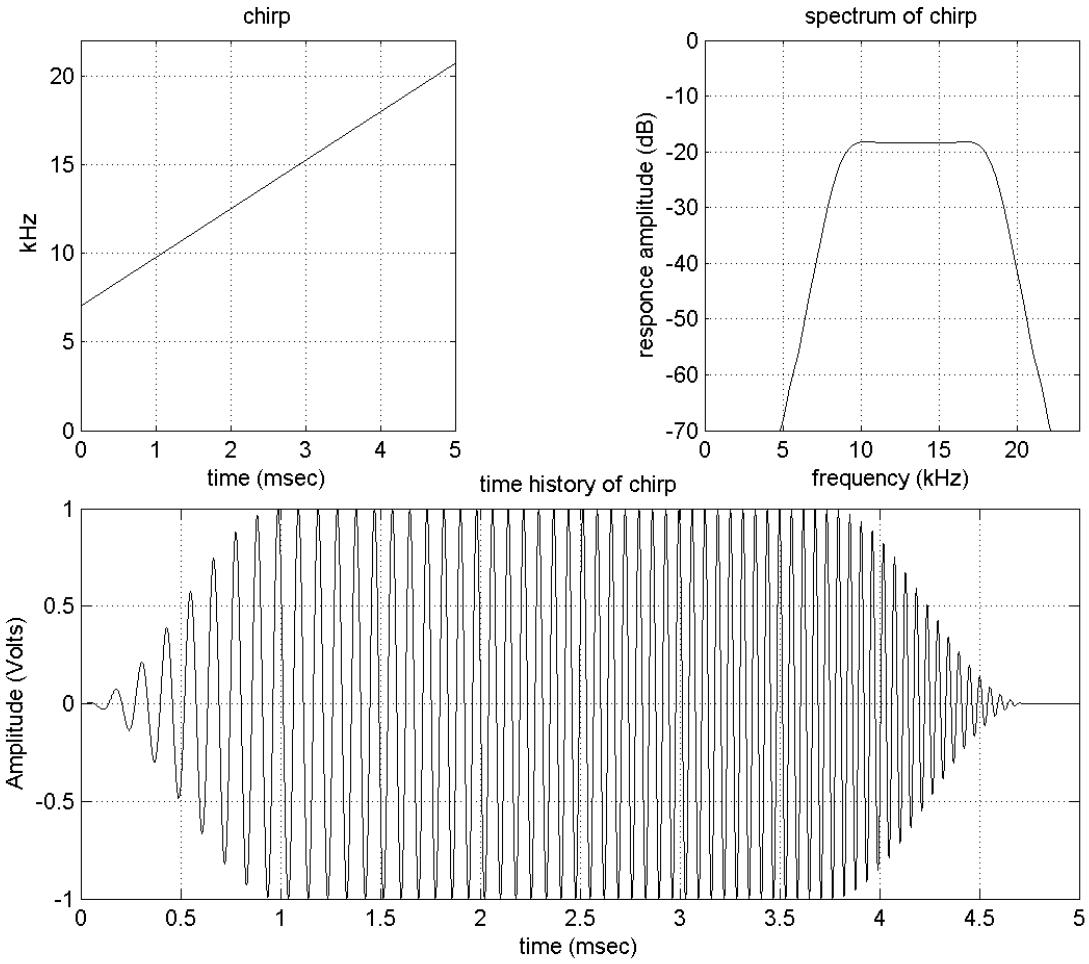

Figure 5.14: Characteristics of chirp excitation used for Protocols 3-5. Duration of 5 ms with a 7-20 kHz bandwidth. Note the linear frequency distribution in time (upper left), corresponding to the flat frequency spectrum (upper right), in contrast to the nonlinear frequency distribution shown in Figure 5.15.

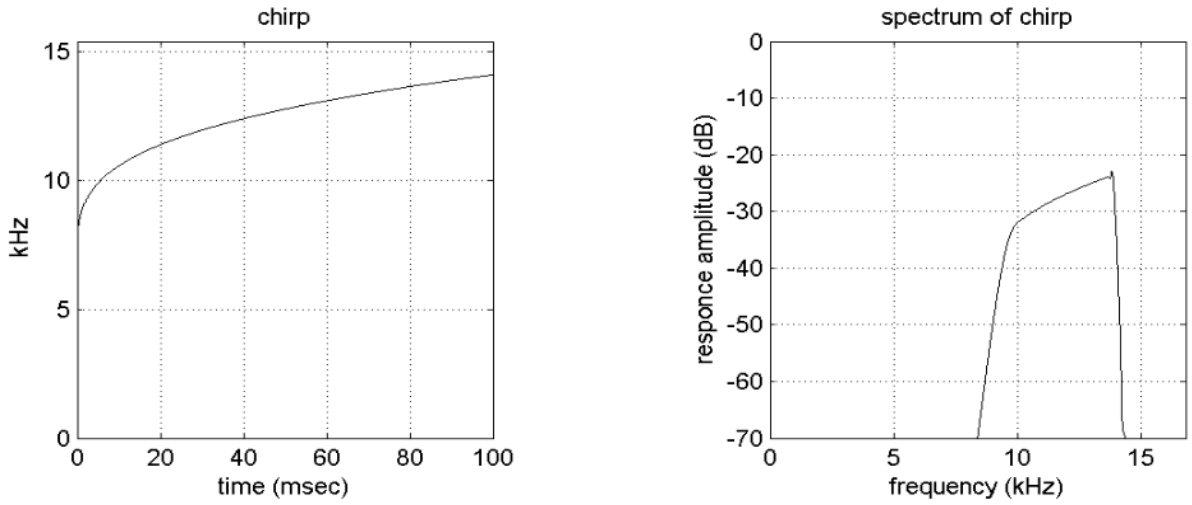

Figure 5.15: Characteristics of chirp excitation used for Protocols 6-10 and A. The nonlinearity in time (left) skews the frequency content, as seen in the spectrum (right), toward the higher frequencies in the range.

(BD Ultrafine II, Becton, Dickinson, and Company, Franklin Lakes, NJ) is used to manipulate individual spheres. The needle tip is wetted by dispensing just enough volume to create a droplet that remains on the needle tip, then withdrawing most of that volume back into the needle. The wetted tip is then used to "trap" a sphere on the needle bevel. See Figure 5.16. The sphere is then transferred onto the sugar water droplet in the desired location on the cantilever tip. The water is allowed to evaporate, leaving sphere secured with the sugar as adhesive. Figure 5.9b in Section 5.3.1 above is a schematic of a large array with a single mass in place on one of the cantilevers. The paragraphs that follow contain a series of calculations for the masses of the cantilevers and spheres. While not directly applicable to the dynamic system, these calculations provide a physical sense of the relative masses of the various components. Section 5.3.4 refers to the formulation of the expression for coupling ratio in Section 5.2.2 to determine the expected slope of an added load/normalized mass curve.

Figure 5.16: Manipulation of spheres using wetted needle. Left and center: Placement of glass spheres on cantilever. Right: Glass sphere held on needle bevel with water.

Cantilever mass

The mass of a single cantilever is determined from geometry and density. For the two different array designs (large and small), one cantilever has volume

$$V_{\text{small}} = (0.5\text{cm})(0.05\text{cm})(0.025\text{cm}) = 6.25 \times 10^{-4}\text{cm}^3$$
$$V_{\text{large}} = (0.8\text{cm})(0.1\text{cm})(0.05\text{cm}) = 4 \times 10^{-3}\text{cm}^3$$

Silicon has density $2.33\frac{\text{g}}{\text{cm}^3}$, so the mass of one cantilever is approximately

$$m_{\text{small}} = V\rho = (6.25 \times 10^{-4}\text{cm}^3)(2.33\tfrac{\text{g}}{\text{cm}^3}) = 1.5 \times 10^{-3}\text{g}$$
$$m_{\text{large}} = (4 \times 10^{-3}\text{cm}^3)(2.33\tfrac{\text{g}}{\text{cm}^3}) = 9.3 \times 10^{-3}\text{g}$$

Steel Spheres			
Diameter [μm]	**Mass [μg]**	**% of Small Cantilever**	**% of Large Cantilever**
300	111	7.4	1.2
350	177	11.8	1.9
400	264	17.6	2.8
450	376	25.1	4
500	515	34.3	5.5
550	686	45.7	7.4

Table 5.7: Mass of steel spheres of various sizes as a percent of cantilever mass.

	Polystyrene		**Glass**		**Steel**	
Diameter [μm]	**Mass [μg]**	%	**Mass [μg]**	%	**Mass [μg]**	%
200	4	0.043	10	0.108	33	0.355
225	6	0.065	15	0.161	47	0.505
250	9	0.097	20	0.215	64	0.688
275	12	0.129	27	0.29	86	0.925
300	15	0.161	35	0.376	111	1.194

Table 5.8: Mass of various spheres as a percent of cantilever mass for the large array design. Steel ($\rho_{\text{steel}} = 7.87\frac{\text{g}}{\text{cm}^3}$), glass ($\rho_{\text{glass}} = 2.48\frac{\text{g}}{\text{cm}^3}$), and polystyrene ($\rho_{\text{PS}} = 1.06\frac{\text{g}}{\text{cm}^3}$)

Dry sphere mass

The steel spheres are cast steel shot (Ervin Industries, AMASTEEL Division, Butler, PA). Sphere sizes were first differentiated using ASTM E-11 test sieves with hole sizes of 500, 425, 355, and 300μm. Glass and polystyrene dry beads (Polysciences, Inc. Warrington, PA) have a stated diameter range of 250-300 μm and 200-300 μm respectively. All dry beads were pre-screened with a linear microscope scale and/or compared to a reference standard sphere to remove outliers for a given mean diameter before use in a protocol. See Figure 5.17a. Table 5.7 lists masses of several steel sphere sizes as well as sphere mass expressed as percentage of cantilever mass for both array sizes. Table 5.8 lists masses of sphere sizes for the different materials used for different protocols in this work. The polystyrene beads allow for addition of miniscule amounts of mass to the cantilevers to create controlled, known amounts of mass disorder.

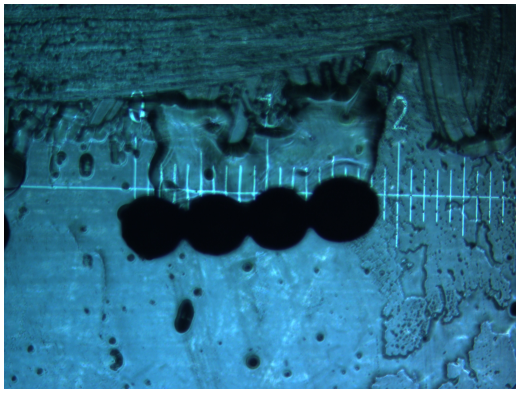

(a)

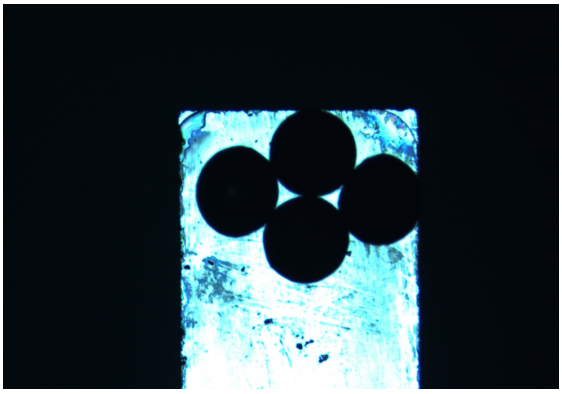

(b)

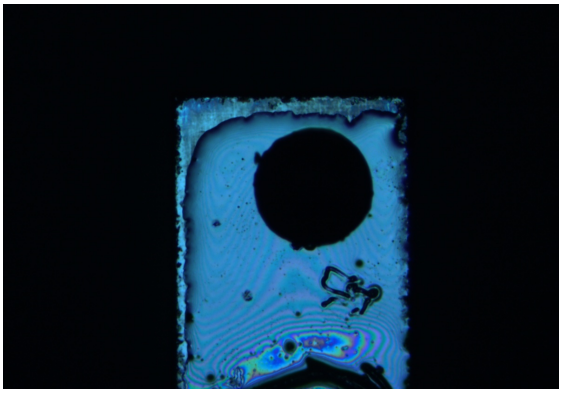

(c)

Figure 5.17: Steel spheres are used as known masses. 5.17a. Steel spheres arranged along the linear scale (100 μm per division) used to select spheres with a desired diameter. 5.17b. Grouping of four steel spheres in place on cantilever. ($D_{\text{sphere}} \approx 300\mu$m). 5.17c. A single steel sphere. Note the visible edge of the drop of sugar water solution used to bind spheres in place ($D_{\text{sphere}} \approx 450\mu$m). Cantilever beam shown in 5.17b and 5.17c is part of a large array and 1000 μm wide.

Polystyrene microspheres solution

The Polybead® microspheres (Polysciences, Inc. Warrington, PA) used in this work are shipped as 2.5%$\frac{w}{v}$ monodisperse solutions. The mass of polystyrene delivered in a 1μL drop of solution is given by $\frac{2.5\text{g}}{100\text{mL}} \times \frac{1\text{mL}}{1000\mu\text{L}} = 2.5 \times 10^{-5} \frac{\text{g}}{\mu\text{L}}$. Therefore, for a single small cantilever with $m_{\text{small}} = 1.5 \times 10^{-3}$g, a 1 μL of microsphere solution corresponds to $\frac{2.5\times10^{-5}\text{g}}{1.5\times10^{-3}\text{g}} = 1.67\%$ of the mass of a small cantilever. Likewise, for the large cantilever with mass, $m_{\text{large}} = 9.3 \times 10^{-3}$g, the 1$\mu$L drop of solution adds $\frac{2.5\times10^{-5}\text{g}}{9.3\times10^{-3}\text{g}} = 0.27\%$ of the large cantilever.

Normalization of added mass amounts

As shown in Section 5.2.2, the mass m for the mass-spring model that gives the model the same vibration energy as the cantilever array is $m = 0.25\rho abL$. Recall from Chapter 4 that the model used as the basis for the mass calculations is scaled or normalized such that $m_0 = 1$. With model mass, $m = 0.25\rho abL$, all masses in the system must be normalized by $0.25\rho abL$ to have the $m_0 = 1$ condition. Therefore, the normalized added mass is

$$m_{\text{norm}} = \frac{m_{\text{added}}}{0.25\rho abL} \tag{5.19}$$

The mass of a single large array cantilever is $m = \rho abL = 9.3 \times 10^{-3}$g , therefore the expected slope is $\frac{1}{0.25\rho abL}$=4.29×10^{-4} $\frac{1}{\mu\text{g}}$.

CHAPTER 6

PROTOTYPE MASS SENSOR: EXPERIMENTAL RESULTS

Chapter Introduction

The purpose of this chapter is the presentation of experimental results. Effective presentation of any results begins with an understanding of the source of the information. Chapter 5 has summarized the physical hardware and procedures for obtaining LDV measurements. This chapter begins with an explanation of the data processing required to calculate the cantilever masses. Results are then presented for individual protocols (6.2), followed by analysis of combined results from the various protocols (6.3). The chapter closes with the important connection linking these experiments to the simulations from Chapter 4.

There is a wide range of data presented in a number of different ways–different loading conditions, different coupling strengths, frequency domain, per load, per cantilever, etc. In an effort for consistency throughout the document, there are some color conventions used for figures representing different types of information. Information relating directly to cantilever motion (FRFs) is shown using the MATLAB copper colormap, ranging from black through shades of copper/orange to represent the eight cantilevers, as in Figure 6.1. The MATLAB cool colormap is generally used to indicate a set of increasing loading conditions, with cyan for the smallest load, ranging to magenta for the largest, as in Figure 6.19. In plots depicting various loading conditions, black open symbols are generally used to represent an unloaded cantilever. The other major distinguishing factor considered in this work is the relative coupling strength, which is generally represented by

blue for low coupling strength, red for the medium R sensors, and green for the high R sensors (with purple for the highest R sensor design for the small sensors, as in Figure 6.8).

Section 6.1 is a detailed description of the calculations used to transform the LDV measurements into cantilever mass estimates. A representative set of data is used to demonstrate the detail of each step of the process. The steps include: phase-normalization of the complex response amplitudes (6.1.1), determination of the weighting factors used for the mass calculation (6.1.2), and normalization of system frequencies, which is inextricably linked to the method for determining the empirical value for the coupling ratio (6.1.3), and finally the mass calculation itself (also 6.1.3).

Section 6.2 describes each of the eleven different study protocols and gives the basic results for each within each subsection. This substantial section introduces terminology and data presentation styles (plotting conventions) used in the remainder of the work. A number of important observations are made from these single-protocol summaries, such as an assessment of the testing assembly, demonstration of basic sensor proof-of-principle, an estimate of the practical limit of detection, and examples of both localized and extended responses.

Section 6.3 presents combined results from the various protocols to make collective observations and highlight sensor behavior. Same-sensor repeatability (Section 6.3.1) is demonstrated, along with a comparison of the relationship between loading and normalized mass for the different protocols (Section 6.3.3). The steel and glass bead loading are compared on the same three sensors in Section 6.3.2. Observed coupling ratios for all sensors are presented in Section 6.3.4.

The last section, Section 6.4, presents the pivotal results from the experimental portion of this work. The section connects the normalized mass disorder and the sensitivity to noise from the numerical simulations in Section 4.3 to the analogous empirical values extracted from the data. The correlation of these measurements with the numerical simulations is shown with a plot of the standard deviation of the mass estimates as a function of normalized mass disorder.

6.1 Data Processing Procedure

This section uses representative data from a large array sensor (Sample ID hia1) to illustrate the data processing required for experimental determination of cantilever masses using the LDV measurement of cantilever response velocities. These response amplitudes are first normalized and used to construct a weighting matrix used for the weighted average of the mass calculations. Coupling ratio determination and frequency normalization are followed by the calculation of the cantilever masses.

6.1.1 Details of processing LDV data

This section details the data processing steps that begin with a set of eight LDV measurements and yield a set of eight predicted mass values. The first step is determining the spectra by FFT of the LDV time domain data. All velocity data presented in this section have a 0.5 Hz frequency resolution and are normalized by the input chirp voltage. A representative set of eight frequency response functions (FRFs) from the AA protocol are shown in Figure 6.1. Any of a number of reasonable peak identification methods may be used to select the eight system resonant frequencies. In this initial proof-of-principle work, location of the eight system resonances is done by simple manual peak selection. In the absence of a clear peak for any given response, an approximation is made based on the expected response frequency.

The system frequencies are grouped into a vector, $\mathbf{f} = [f_1 \dots f_8]$. At any one of these eight system resonant frequencies, the complex amplitudes, $\hat{u}_n$, correspond to the motion of each of the N cantilevers. Taken together, each group of complex amplitudes is the system response shape, $\hat{\mathbf{u}}$, at the j^{th} frequency such that $\hat{\mathbf{u}}_j = \left[\hat{u}_{1,j} \dots \hat{\mathrm{u}}_{8,j}\right]^T$ for $j = 1 \dots 8$. The eight complex response vectors, $\hat{\mathbf{u}}_j$ are gathered into a complex response matrix $\hat{\mathbf{U}}$. In the light damping regime, those response shapes will be close approximations of the system modes, and with little system disorder, the shapes are extended sinusoids.

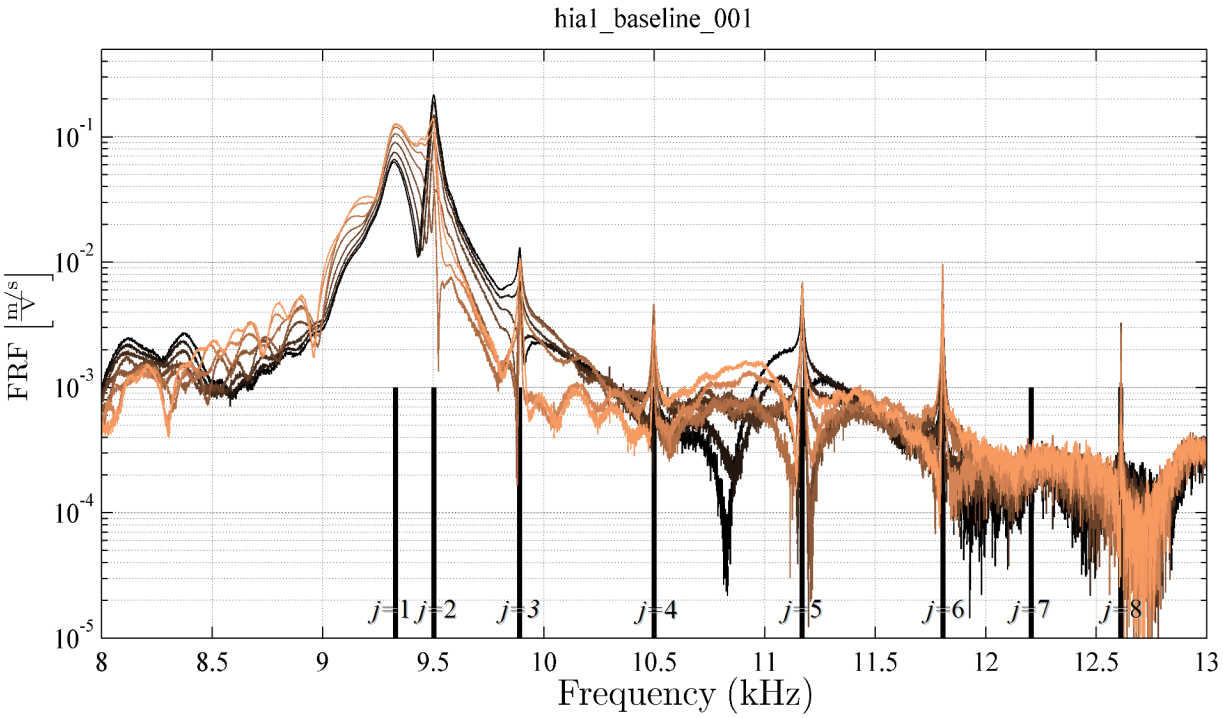

Figure 6.1: The set of eight frequency response functions from an LDV scan with vertical lines indicating selected frequencies for the eight system resonances. Each color represents a single cantilever.

The first column of Figure 6.2 presents these complex responses $\hat{\mathbf{u}}_j$ on the complex plane. The colors in both Figures 6.1 and 6.2 correspond to individual cantilevers. The eight rows represent the system resonances in increasing frequency from top ($j = 1$) to bottom ($j = 8$). Each plot contains one column, $\hat{\mathbf{u}}_j$, of the response matrix $\hat{\mathbf{U}}$. Note that for $j = 4, 6, 8$, in Figure 6.2, responses are both highly linear and pass through the origin on the complex plane. Those same responses exhibit clear, strong peaks in the frequency domain (Figure 6.1, $j = 4, 6, 8$). Also, there is no meaningful peak for the $j = 7$ frequency response, likewise, the complex amplitudes are very small and fall in a cluster away from the origin.

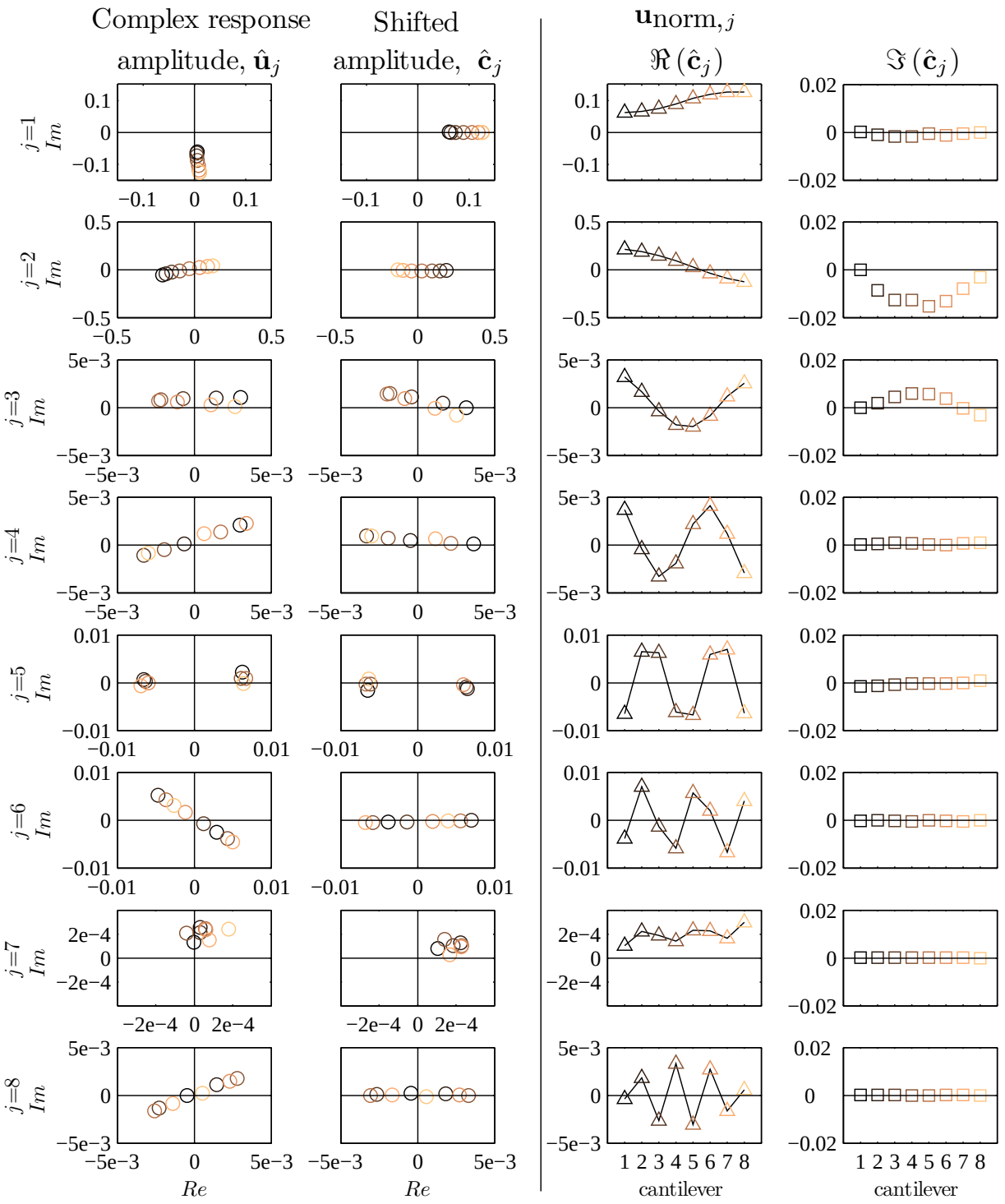

Figure 6.2: Data processing steps: Phase-normalization of complex response amplitudes.

At this point, a reminder of the underlying math, described in Section 4.1 is warranted. System masses are calculated with the inverse problem, Equation 4.6, restated here:

$$\Delta m_n = \frac{\left([-\omega_j^2\mathbf{I}+\mathbf{K}]\mathbf{u}_{\text{noisy}}\right)_n}{\omega_j^2\left(\mathbf{u}_{\text{noisy}}\right)_n} \text{ for } n = 1\ldots N \tag{6.1}$$

The system response $\mathbf{u}_{\text{noisy}}$ and frequency ω_j from Equation 6.1 must be replaced with measured peak frequencies and response shapes that are normalized in a way to allow comparison and generalizations. The frequency normalization is relatively straightforward, and is detailed in Section 6.1.3. The process of phase-normalizing the complex amplitudes $\hat{\mathbf{u}}_j$ requires more consideration and is treated in detail first.

The goal is a process that uses the complex amplitudes to generate a response matrix $\mathbf{U}_{\text{norm}}$ consisting of real numbers that reflect the relative motion of the cantilevers, without loss of relative phase information. Equation 6.2 is applied to the eight complex amplitudes $\hat{\mathbf{u}}_j$ at each frequency (Figure 6.2 Column 1). The effect is a shift in phase such that the complex amplitude with the largest overall magnitude has a phase of zero.

$$\hat{\mathbf{c}}_j = \frac{\hat{\mathbf{u}}_j}{\max\left(\frac{\hat{\mathbf{u}}_j}{\left|\max\left(\hat{\mathbf{u}}_j\right)\right|}\right)} \text{ for } j = 1\ldots N \tag{6.2}$$

The shifted response shape, $\hat{\mathbf{c}}_j$ is now primarily real, and is shown on the complex plane in Column 2 of Figure 6.2. The remaining plots in Figure 6.2 show the real and imaginary components of $\hat{\mathbf{C}}$ with $\Re(\hat{\mathbf{C}})$ in Column 3 and $\Im(\hat{\mathbf{C}})$ in Column 4. After phase normalization, the real portion of each amplitude is assumed to represent response in the dominant mode shape, and the remaining (relatively small) imaginary portions are assumed to be combined contributions to the response from other modes and measurement noise. Thus, the response matrix used in Equation 6.1 for

calculation of system masses is the real part of the shifted response, $\mathbf{U}_{\text{norm}} = \Re(\hat{\mathbf{C}})$. Also, with the exception of the $j = 7$ case, the normalized responses, $\mathbf{u}_{\text{norm},j}$, in Figure 6.2, Column 3 demonstrate expected sinusoidal shapes of increasing spatial frequency as j increases.

Another graphical representation of the response shapes is given in Figure 6.3. The bottom row of line plots is identical to the third column of Figure 6.2. Similar to the color pixel representation of response matrices in Figures 4.2 and 4.3, the top row in Figure 6.3 represents the magnitude of the normalized responses of each cantilever with a color pixel. White indicates little or no motion while red and green indicate opposite direction (if red is up, green is down).

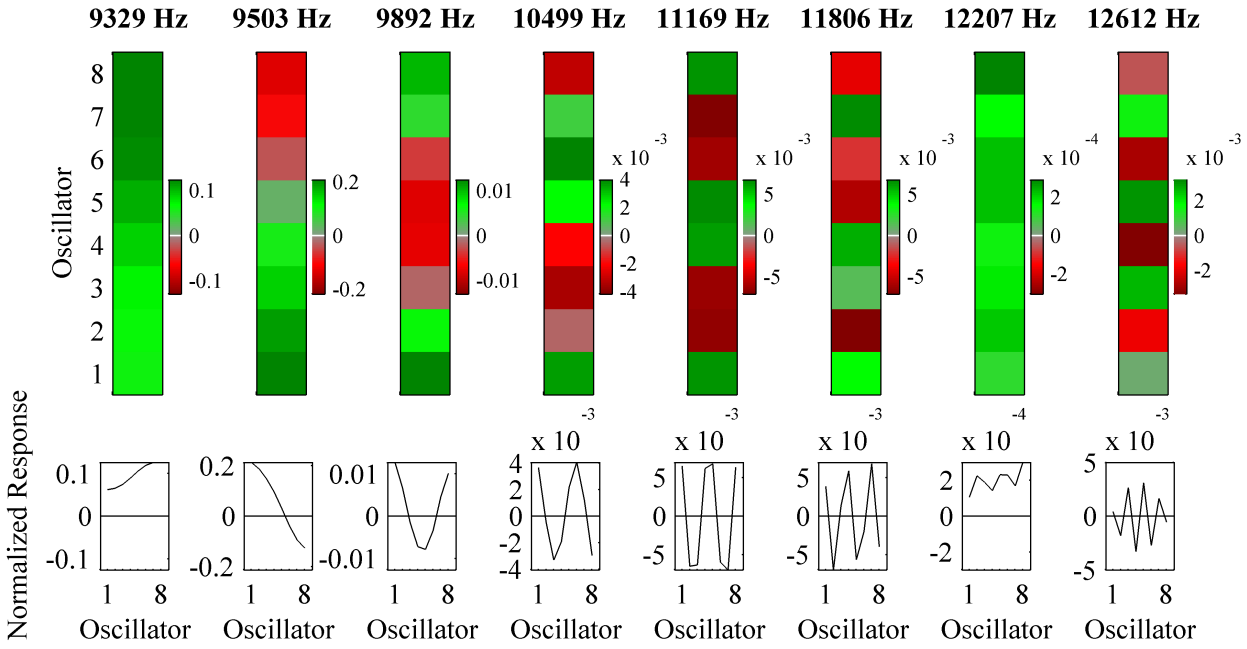

Figure 6.3: Two graphical representations of system response amplitudes

Each response shape $\mathbf{u}_{\text{norm},j}$ (column) is paired with a colorbar indicating the range of magnitudes for that particular response. Note that each colorbar is scaled to a range appropriate for that $\mathbf{u}_{\text{norm},j}$. The lack of alternating red and green pixels in the 7^{th} response highlights the deviation from the expected behavior. This color pixel representation is a powerful visualization tool for the effects of disorder, as shown further in the bottom two panels of Figure 6.4.

The top half of Figure 6.4 shows two FRFs measured on the same sensor under two loading conditions: a baseline measurement with no load in cyan, and with an added mass on cantilever 1 in blue. The two response panels in the bottom half of Figure 6.4 are the responses $\mathbf{U}_{\text{norm}}$, with a $\mathbf{u}_{\text{norm},j}$ in each column, further normalized such that each column has a maximum amplitude of 1. The baseline system response matrix, (corresponding to the cyan FRF) is shown in the bottom left panel. As expected, an addition of mass shifts the resonant frequencies (blue spectra) downward. The downward shift in frequency is dramatic for the fundamental response (from around 9300 Hz down to around 8800 Hz), undetectable at this axis scaling for the highest frequency peak (around 12.6 kHz), and varies proportionately for the peaks in between. In addition, the spread of amplitudes in the fundamental peak is evident in the blue FRF, but is better illustrated in the response panel (bottom right). After the addition of mass, oscillators 5, 6, 7 and 8 have dramatically reduced amplitude in $\mathbf{u}_{\text{norm},1}$ and the inflection point in $\mathbf{u}_{\text{norm},2}$, indicated by the change from red pixels to green, has shifted dramatically. In the case without mass, the inflection for the second response ($\mathbf{u}_{\text{norm},2}$) is between oscillators 4 and 5; with mass, the inflection in the second response occurs between oscillators 1 and 2. Changes of this nature are less easily discerned directly from the spectra.

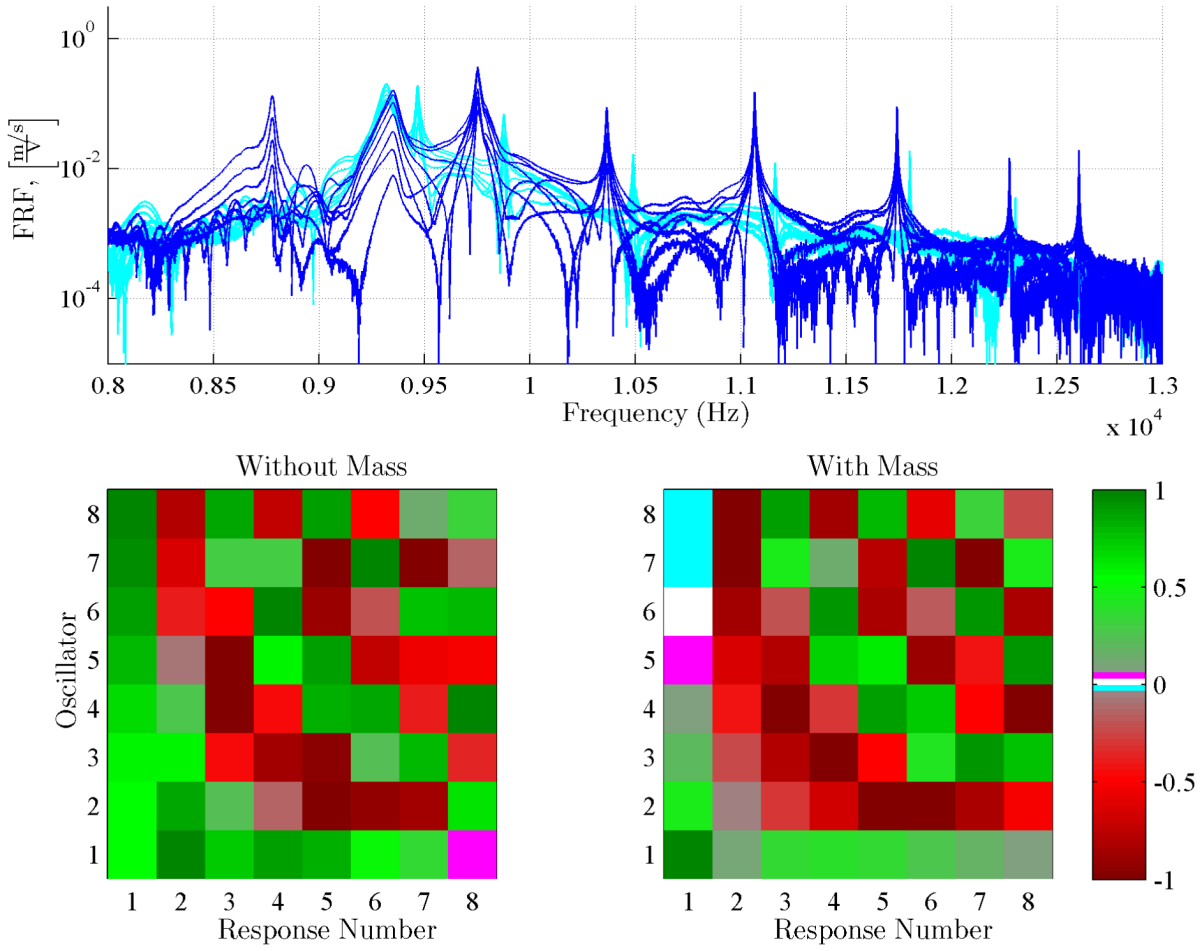

Figure 6.4: Changes in spectra and response shape with added mass. Unloaded array FRF in CYAN, FRF of array with mass in BLUE.

6.1.2 Weighting factor determination

Having introduced this visual representation of system motion, we return to the process of calculating system masses with these measured system responses. This section has presented a method of taking the complex response amplitudes $\hat{\mathbf{U}}$ and phase-normalizing to yield a matrix of 8 fully real response shapes $\mathbf{U}_{\text{norm}}$. Equation 6.3 takes a single response shape and frequency to generate a set of predicted system masses. The 8 response shapes will generate 8 predictions that may vary wildly. Consider the consequence of using Response 1 from the case with mass added

in Figure 6.4 when the measurement is made in an environment with noise. Judicious application of weighted averaging can capitalize on areas of the array with strong response, and minimize the effect of noise when measuring the small amplitudes on resonators 5-8.

$$\Delta m_n = \frac{\left([-\omega_j^2 \mathbf{I} + \mathbf{K}] \mathbf{u}_{\text{norm}} \right)_n}{\omega_j^2 \left(\mathbf{u}_{\text{norm}} \right)_n} \text{ for } n = 1 \ldots N \tag{6.3}$$

Figure 6.5 returns to the plots of the real and imaginary parts of the phase shifted response amplitude. A weighting factor matrix W is defined as the ratio of the absolute value of the normalized response to the root-mean-square amplitude of the imaginary part of the response. Placing the term based on the size of the imaginary part of the response in the denominator diminishes the influence of responses with considerable noise or non-dominant modal content.

$$\mathsf{W} = \frac{\left| u_{\text{norm}_{n,j}} \right|}{\text{RMS}\left(\Im \left(\hat{\mathbf{C}}_j \right) \right)} \tag{6.4}$$

This weighting factor lessens the influence of responses with generally low amplitudes as well as cantilevers at or near nodes in a given response shape. See Table 6.1 and the corresponding plots in Figure 6.5. For example, the response for $j = 7$ has the overall smallest amplitude and has uniformly small weighting factors (See Table 6.1, in (MAGENTA)). On the other hand, the for $j = 8$ response is overall somewhat stronger than the $j = 7$ case, but cantilevers 1 and 8 are near zero amplitude. The corresponding weighting factors are 4.1 and 5.7 respectively (See Table 6.1, in (CYAN)), several times smaller than for the other elements in that response shape, which range from 16.2 to 32.9. The effect of the denominator term is illustrated well by the response for $j = 2$. The plot of $\mathbf{u}_{\text{norm},2}$ appears to be a "clean" second mode with a strong amplitude. However, the considerable imaginary part discounts the quality of the information, leaving the weighting factors smaller, particularly for the middle cantilevers, $n = 4 \ldots 7$ (See Table 6.1, in (RED)) .

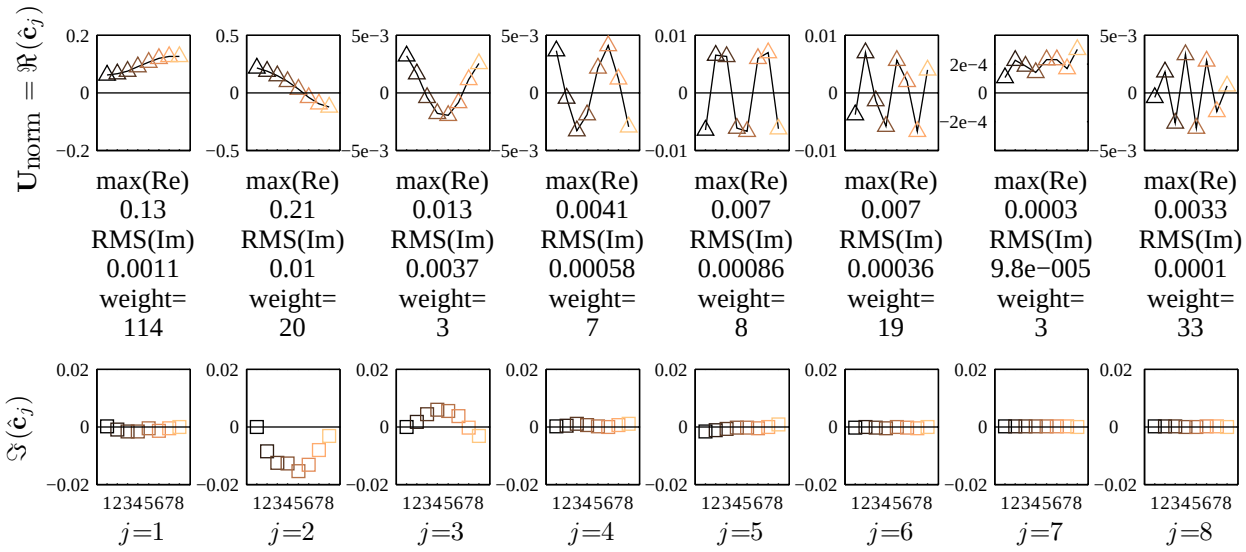

Figure 6.5: Data processing steps: normalization of complex response amplitudes

		Response							
		j=1	j=2	j=3	j=4	j=5	j=6	j=7	j=8
Cantilever	n=1	55.8	20.3	3.4	6.3	7.5	10.5	1.0	4.1
	n=2	58.8	17.9	1.7	0.81	7.5	19.1	2.2	18.1
	n=3	67.2	14.0	0.41	5.7	7.3	3.7	1.9	26.3
	n=4	80.6	9.0	1.9	3.3	7.1	16.0	1.4	32.9
	n=5	95.4	2.8	2.1	3.7	7.8	15.4	2.3	30.6
	n=6	107.4	3.7	0.9	7.0	6.9	5.4	2.3	27.3
	n=7	113.5	9.0	1.2	2.0	8.1	18.7	1.7	16.2
	n=8	114.3	12.1	2.7	5.1	7.3	10.7	3.0	5.7

Table 6.1: Element weighting factors for mass calculation

6.1.3 Coupling ratio determination, frequency normalization, mass calculation

Armed with the set of weighting factors in Table 6.1, a matrix of normalized response amplitudes, $\mathbf{U}_{\text{norm}}$, and Equation 6.3, two quantities remain to be determined before mass calculations can be made: coupling ratio, R, and a normalized frequency vector. The frequency vector is de-

termined during the process for extracting the coupling ratios. Coupling ratio is determined as follows.

Recalling from Section 3.3.1 that the bandwidth $\Delta = \sqrt{1+4R}$, extracting the bandwidth from the measured frequencies yields the coupling ratio. However, as mass is added to the system, resonant frequencies shift, with the most pronounced shifts occurring in the lower modes. As the higher modes are proportionally less affected by such shifts, the high frequency responses, $f_4 - f_8$, are used in this process with the intention of making the determination of sensor R independent of loading condition.

A bisection method approach is used to match an ideal frequency distribution to the measured frequencies using three successive pairs of frequencies. The highest frequency f_8 is normalized to the ideal frequency distribution $f_8 \longrightarrow f_8^{\text{n}}$ and successively paired with three other frequencies (f_4^{n}, f_5^{n}, and f_6^{n}) to make three estimates for R. Figure 6.6, left, shows this frequency curve "fit" using the f_8–f_5, pairing. In other words, an estimate of R is determined from the normalized Δ of the ideal frequency distribution, when the conditions of $f_{\text{ideal},5}^{\text{n}} = f_{\text{exp},5}^{\text{n}}$ and $f_{\text{ideal},8}^{\text{n}} = f_{\text{exp},8}^{\text{n}}$ are imposed. The estimate is repeated when forcing equality between normalized measured data and the ideal for f_8^{n}–f_4^{n} and f_8^{n}–f_6^{n}. Again, the 8^{th} frequency is used as an anchor point because of the substantially lower observed shift in f_8 over the course of the preliminary measurements. The three estimates for R are averaged for use in the subsequent mass calculations. The frequency vector used for mass calculations is the experimental vector normalized such that $f_{\text{ideal},8}^{\text{n}} = f_{\text{exp},8}^{\text{n}}$.

The right plot in Figure 6.6 shows the resulting calculated masses, with each color curve representing the calculated mass for each resonator based on a given response shape. The color of the curves in Figure 6.6 right correspond to the weighting factors highlighted in Table 6.1. The triangles are the weighted average mass for each cantilever. For example, the green curve, based on $\mathbf{u}_{\text{norm},4}$ indicates a large mass for cantilever 2. Referring back to Table 6.1, the weighting factor $W_{2,4}$ is only 0.81. Referring further back to Figure 6.5, an examination of the plot of $\mathbf{u}_{\text{norm},4}$ reveals that the second resonator has an amplitude of nearly zero. The implication is that the wild outliers

for calculated mass of oscillator 3 using $\mathbf{u}_{\text{norm},3}$ and oscillator 2 using response $\mathbf{u}_{\text{norm},4}$ have little impact on the final mass calculation due to the weighting matrix. Similarly, the uniformly low weighting factors for all elements of $j = 7$ (Table 6.1, magenta) minimizes impact of the skewed mass values generated from $\mathbf{u}_{\text{norm},7}$ (Figure 6.6 right, magenta curve) on the final mass calculations (triangles).

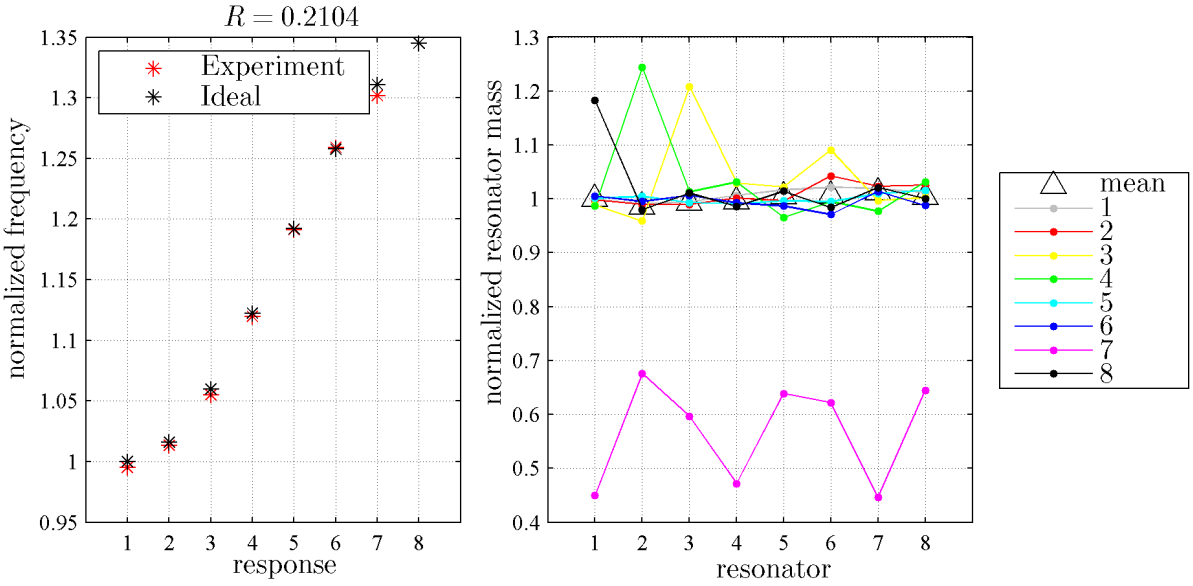

Figure 6.6: Mass and coupling ratio determination

6.2 Results and Discussion: Specific Study Protocols

Each of the eleven subsections summarizes the key findings of an individual protocol. A short synopsis of each protocol is given here in the section introduction as a table of contents specifically for this section.

6.2.1 Protocol 1: Small array, two-dimensional scan

The primary purpose of this preliminary study is the vetting of the testing assembly. Results from the measurement of a number of locations, both on the cantilevers and on the silicon base of the array, gives assurance that the frequency range of interest in this work does not contain interference from resonances of the testing structure. This protocol has been discussed in detail

in Section 5.3.1 and 5.3.2. The important result, that the base response is flat and well below the response of the cantilever tips, is shown in Figure 6.7.

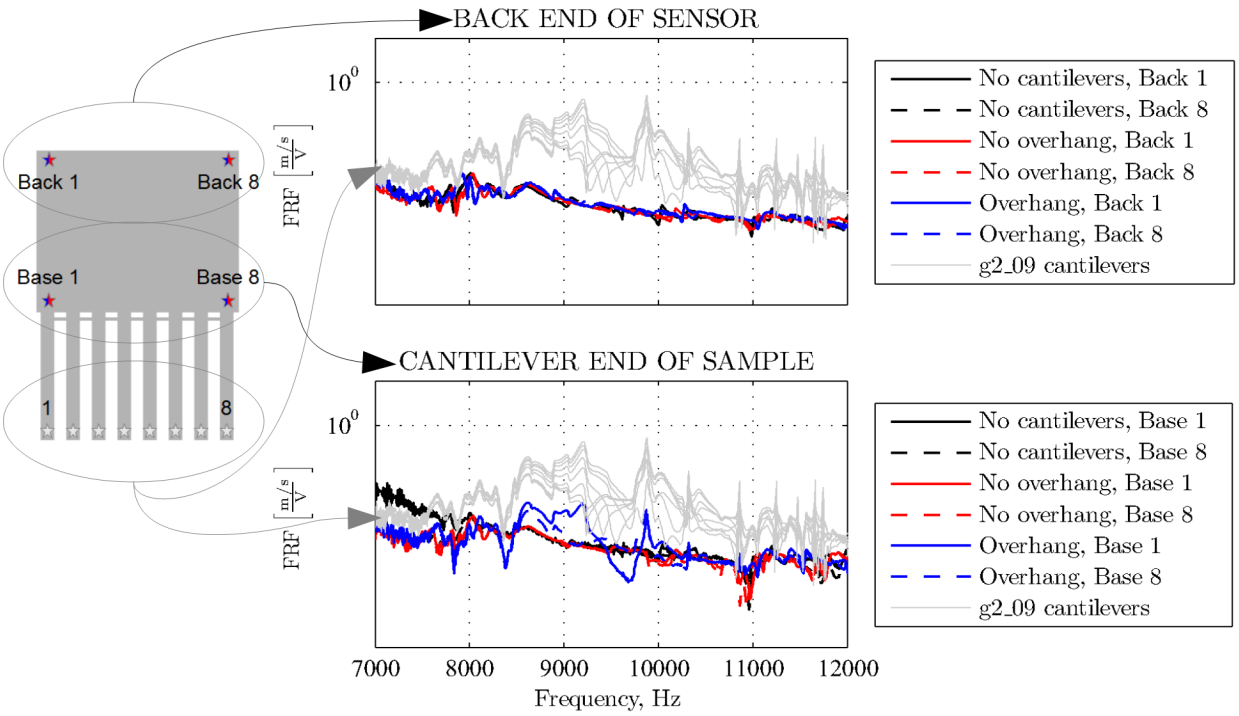

Figure 6.7: Results from Protocol 1. Amplitudes of various locations over the entire sensor surface. The schematic at left shows locations on the sensor measured by LDV to assess the motion of the test assembly compared to that of the cantilevers. The response amplitudes are shown in the plots on the right.

6.2.2 Protocol 2: Small array, baselines

The purpose of this preliminary study, discussed previously in Section 5.3.3, is the determination of the range of frequencies observed in the small array sensors such that excitation parameters for subsequent protocols can be determined. As shown in Figure 6.8, with the exception of the highest coupling sensors (800 μm gap), the variation in both fundamental frequency and sensor bandwidth is substantial. Excitation frequency range for each individual sensor indicated by the black squares. Excitation bandwidth for additional protocols using this sensor type was selected to

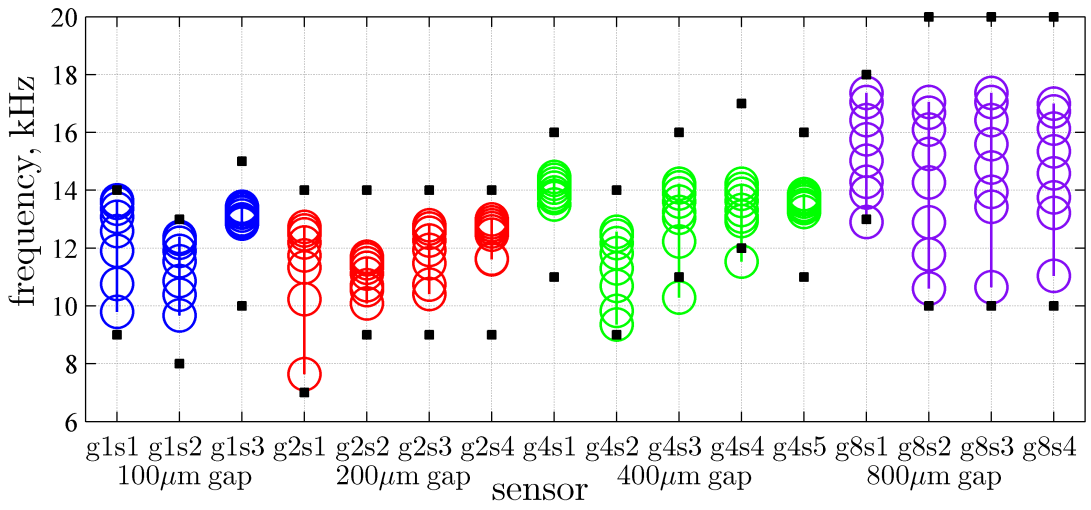

Figure 6.8: Peak frequencies measured in Protocol 2. Excitation bandwidth is bracketed by ■ for each sensor.

be 7-20 kHz, based on the overall range of all sensors. Coupling strength (and therefore bandwidth) should increase with the larger gap dimension. Significant variation is evident in the bandwidth of the individual sensors with 100, 200, 400 μm gap length, indicative of large variation in the actual coupling strengths of most of the samples of the small array design.

6.2.3 Protocol 3: Small array, BOE cleaning

After noting the variability of peak frequencies in the results of Protocol 2, the sensors were subjected to a 5 minute buffered oxide etch (BOE) cleaning process. Three of the samples were damaged during the cleaning process, leaving a total of 13 sensors with paired scans (before and after BOE). Figures 6.9 and 6.10 illustrate the slight differences in sensor behavior between the two states. Figure 6.9 is an updated snapshot of the baseline results presented above in Figure 6.8. The damaged sensors are removed from the plot and the results from Protocol 3 scans are now included. The open circles represent the frequencies from the Protocol 2 scans (before BOE), while the smaller, filled circles represent the frequencies from the Protocol 3 scans (after BOE).

A few shifts in fundamental frequency are evident (notably in sensors g8s3 and g8s4), but there is not a substantial change in bandwidth, peak frequency distribution, or fundamental frequency.

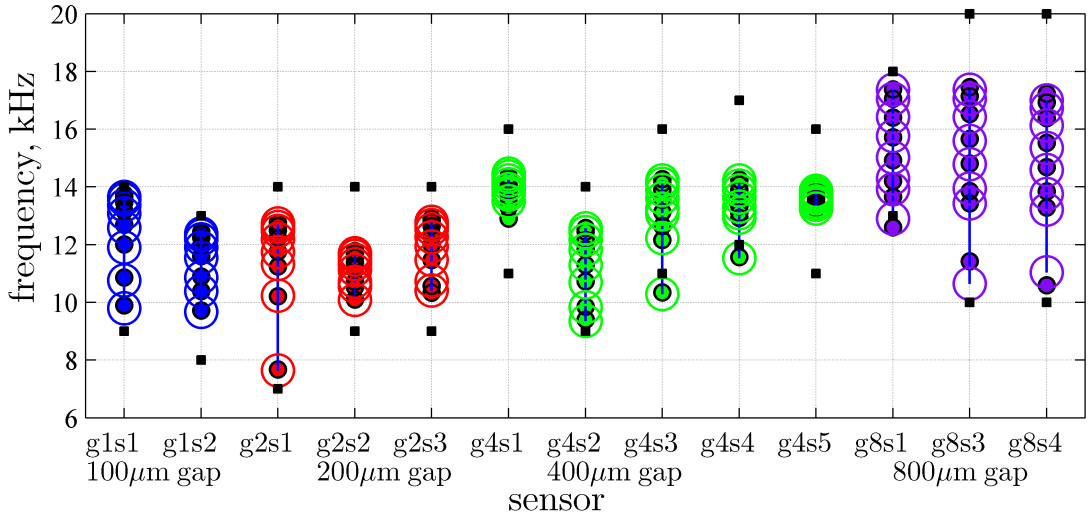

Figure 6.9: Protocol 3 Results: Peak frequencies before ◯ and after • BOE cleaning. Excitation bandwidth bracketed by ■ for each sensor.

On the other hand, Figure 6.10 shows that the cleaning process did make a statistically significant difference in the mass calculations from the 13 sensors common to Protocols 2 and 3. A two-tailed two-sample t-test with assumed unequal population variance yields a probability $p = .011$ that the difference in the population means is zero. The standard deviations are 0.012 and 0.008 respectively. The BOE cleaning process does reduce the standard deviation of the mass estimates within a given sensor, however, the wide variation in actual bandwidth is an unanticipated result.

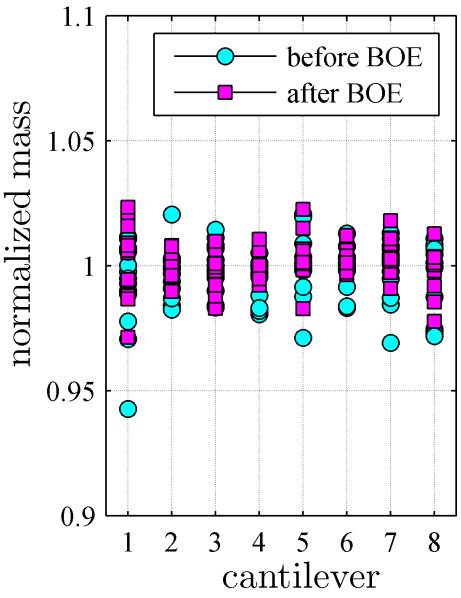

Figure 6.10: Protocol 3 Results: Mass calculations before ($\sigma = 0.0122$) and after ($\sigma = 0.0087$) BOE cleaning procedure. The two sets have $p = .011$ of belonging to populations with the same mean.

6.2.4 Protocol 4: Small array, incremental additions

This protocol is a preliminary experiment that uses a single Type 2 sensor and evaluates the addition of mass using 7 incremental volumes of solution containing 45 μm polystyrene microspheres. See Section 5.3.4 for detail regarding the methods for mass addition. An extreme loading case using four steel spheres with a total mass of about 80% that of the cantilever is also included. The LDV scan consists of 8 measurements, one measurement point per cantilever, and a scan is completed for each of the 8 loading conditions. The unloaded states for this sensor from Protocol 2 (baselines) and Protocol 3 (BOE cleaning) are included in the analysis for a total of 10 states.

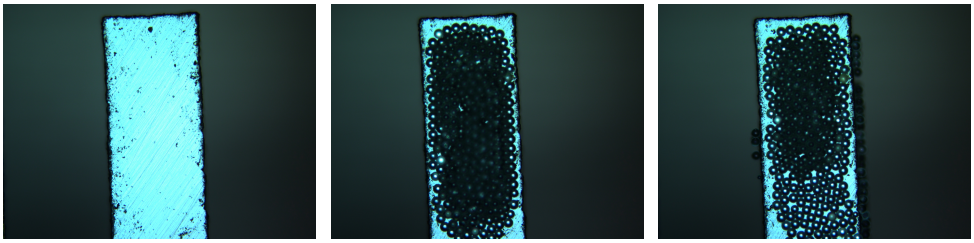

(a) Silicon cantilever beam before mass addition. Beam is 500 μm wide

(b) Cantilever with 12.5 μg

(c) Cantilever with 25 μg

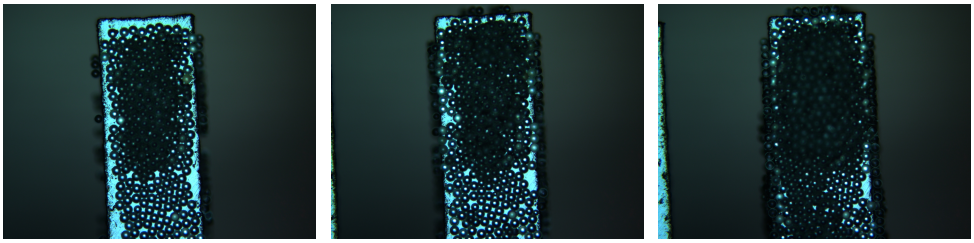

(d) Cantilever with 37.5 μg

(e) Cantilever 50 μg

(f) Cantilever with 62.5 μg

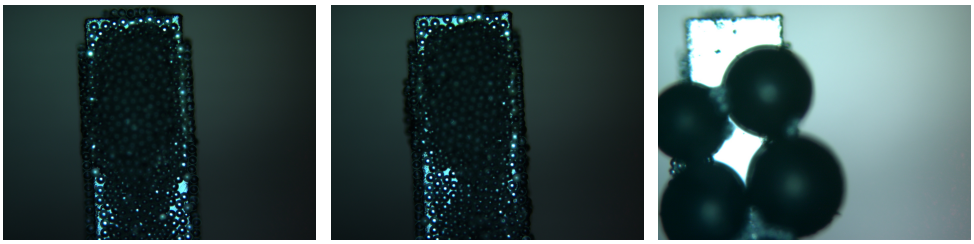

(g) Cantilever with 75 μg

(h) Cantilever with 100 μg

(i) Cantilever with $\approx$ 1200μg

Figure 6.11: 6.11a-6.11h Incremental addition of mass using 45 μm polystyrene microspheres. 6.11i Assortment of four 250-500 μm steel spheres on a single cantilever.

Figures 6.11b to 6.11h show the cumulative addition of 0.5μL of microsphere solution in each photograph, corresponding to 12.5μg of added mass per addition. That 12.5μg corresponds to approximately 0.83% of the actual mass of the small cantilever, or an estimated 3.6% change in effective mass per drop, according to the formulation described in Section 5.3.4. Additional drops bring the total added mass to 100μg, which is an estimated change in effective mass of 12.7%.

Empty circles in Figure 6.12 (and any black line empty symbols throughout this chapter) correspond to a measurement made with no load on that particular cantilever. Each scan consists of a measurement on all eight of the cantilevers, so in this protocol cantilevers 2-8 are unloaded for

all 10 scans. As mentioned, the two empty circles for cantilever 1 correspond to the Protocol 2 (baseline, no load) and Protocol 3 (BOE cleaned, no load) scans. The filled circles in Figure 6.12 correspond to the subsequent mass additions. Loading states are assigned color values that transition smoothly from cyan for 12.5 μg of microspheres(Figure 6.11b) to magenta for the group of steel beads (Figure 6.11i). All calculated masses indicate an increase from the unloaded state, but as noted in Figure 6.12b, the masses do not increase in the expected monotonic manner.

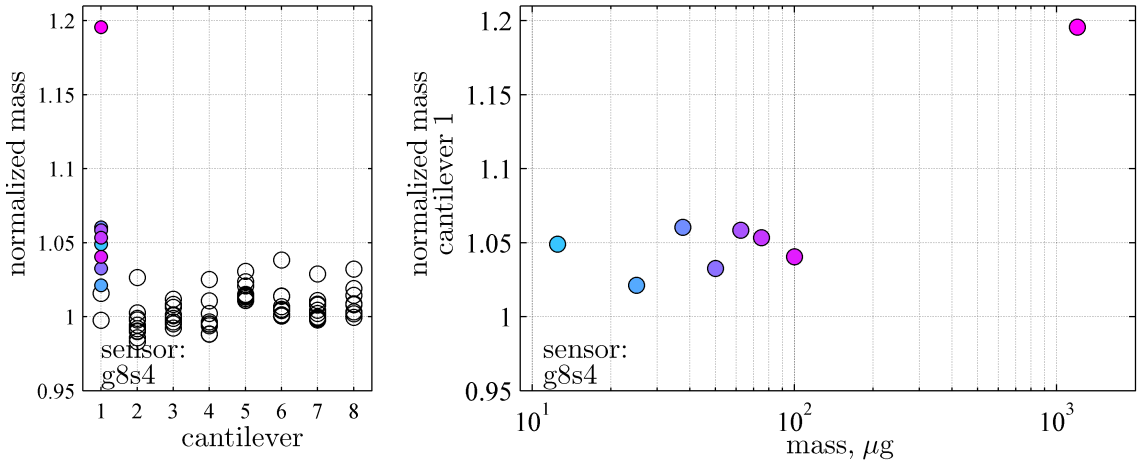

(a) Calculated normalized mass

(b) Calculated normalized mass as a function of actual added mass

Figure 6.12: Protocol 4: Incremental mass addition using microsphere solution on one cantilever of small format sensor g8s4

6.2.5 Protocol 5: Small array, one mass on each cantilever

This protocol is a preliminary experiment that uses a single 375μg ($d = 450\mu$m) steel sphere for the mass load. A pair of scans is completed for each cantilever for a total of 16. As before, one scan is completed in the unloaded state, the sphere is placed on the prescribed cantilever, and the second scan is completed. The resulting mass calculations are given in Figure 6.13. As with Figure 6.12 above, the open symbols represent an unloaded state. Each cantilever is measured a total of 16 times. There is one measurement with the sphere in place (termed a *loaded cantilever* measurement), and a total of 15 unloaded measurements: 8 from the 8 scans completed when

there is no load on any cantilever (termed *empty-cantilever–empty-array*) and 7 from the scans completed when the sphere is placed on one of the other cantilevers (termed *empty-cantilever–loaded-array*).

The sphere mass of 375μg corresponds to roughly 25% of the cantilever mass. From Section 5.3.4, the expected change in effective mass is 4 times the actual change in mass, for an expected normalized mass of around 2. As shown in Figure 6.13 the calculated normalized masses are well below 2 and have a mean of $\mu_{(1\text{ sphere})} = 1.5 \pm 0.1$. It should be noted that the formulation in Section 5.3.4 assumes that added mass is small compared to cantilever mass, so with 25% loading, the discrepancy is not terribly surprising.

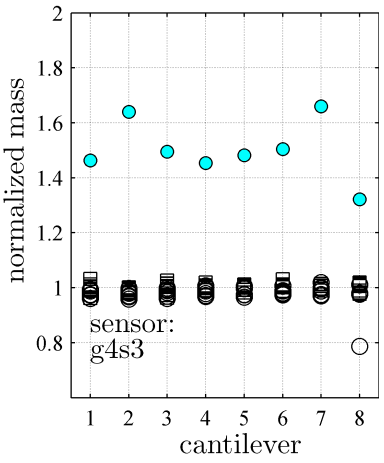

Figure 6.13: Protocol 5 Results. One 375μg ($d = 450\mu$m) steel sphere per cantilever.

6.2.6 Protocol 6: Large array, one mass on each cantilever

This is a preliminary study using the large format array with one-at-a-time cantilever loading. Table 6.2 summarizes the load locations for the even numbered scans. An unloaded scan is conducted as a control case before each loaded scan indicated in the table. (In other words, scans $1,3,5\ldots15$ are empty-cantilever–empty-array). As with all scans to be discussed in the remainder of this work, for any given loading condition, all cantilevers are measured. The set of 16 scans are completed for each of the two mass amounts. The 450 μm sphere has mass of 375μg, which

is approximately 4% of the cantilever mass. The 350 μm(177μg) sphere is approximately 2% of cantilever mass. This alters the mass in the single-degree-of-freedom-per-element model by 16% and 8% respectively.

		LDV Scan							
		2	4	6	8	10	12	14	16
Cantilever	n=1	load	0	0	0	0	0	0	0
	n=2	0	load	0	0	0	0	0	0
	n=3	0	0	load	0	0	0	0	0
	n=4	0	0	0	load	0	0	0	0
	n=5	0	0	0	0	load	0	0	0
	n=6	0	0	0	0	0	load	0	0
	n=7	0	0	0	0	0	0	load	0
	n=8	0	0	0	0	0	0	0	load

Table 6.2: Protocol 6 loading conditions: A set of 16 scans are completed for each loading level. An unloaded array is measured before each loading condition (load=0 on all cantilevers for scans $1,3,5\ldots15$)

Figure 6.14 shows the results of the Protocol 6 scans. The empty-cantilever–empty-array measurements for both mass levels are black circles. Filled color circles indicate the loaded condition. The empty color circles are the empty-cantilever–loaded-array measurements. The increased load level is marked by an increased reduction in the mean of the empty-cantilever–loaded-array measurements (which is an artifact of the frequency normalization method, discussed earlier in Section 6.1.3), as well as an increase in the standard deviation, as indicated in Table 6.3. The expected model masses of 1.08 and 1.16 compares well to experimental means of 1.07 and 1.16.

		Mean, $\mu \pm \sigma$	p	$N_{\textbf{points}}$
black open circle	empty cantilever-empty array, 177 μg	0.998 ± 0.02	0.77	64
	empty cantilever-empty array, 375μg	0.997 ± 0.03		
magenta open circle	empty cantilever-loaded array, 177μg	0.994 ± 0.01	0.0046	56
cyan open circle	empty cantilever-loaded array, 375μg	0.984 ± 0.02		
magenta filled circle	loaded cantilever, 177μg	1.07 ± 0.018	6×10^{-7}	8
cyan filled circle	loaded cantilever, 375μg	1.16 ± 0.022		

Table 6.3: Protocol 6 statistics

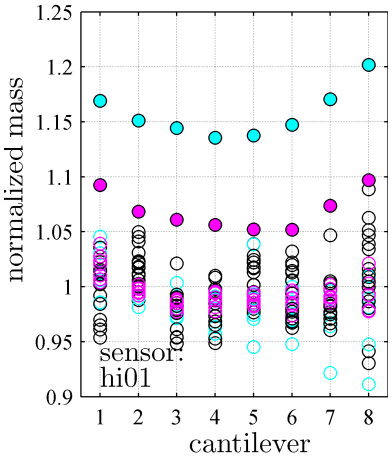

Figure 6.14: Protocol 6: Large sensor preliminary study. One mass at a time loading with two steel sphere sizes. 450 μm=375μg and 350 μm=177μg

6.2.7 Protocol AA: Large array, baselines, 12 sensors

Protocol AA is a simple set of scans in which each sensor is measured with no load (empty cantilever-empty array). A complete set of baseline plots for each sensor (FRF, response shape, frequency curve fit, coupling ratio R, and individual mass calculations) are included in Appendix A. The first aspect of performance of these large array sensors to be examined is the location of the resonant peak frequencies. Figure 6.15 shows the eight peak frequencies for each of the sensors measured in this unloaded protocol. The first observation is the relative consistency of the fundamental frequency. As shown in Figure 5.6b, the geometry and material properties indicate

the fundamental resonant frequency of an isolated cantilever for this design is about 9.4 kHz. The results in Figure 6.15 corroborate the calculation. In stark contrast to the small sensors measured in Protocol 2 (See Figure 5.12), these large format sensors are consistent in both fundamental frequency and bandwidth. The consistency of the fundamental frequency and bandwidth within a sensor design, and the increase of bandwidth noted among the three designs are a basic indicator that the sensor behavior is as intended.

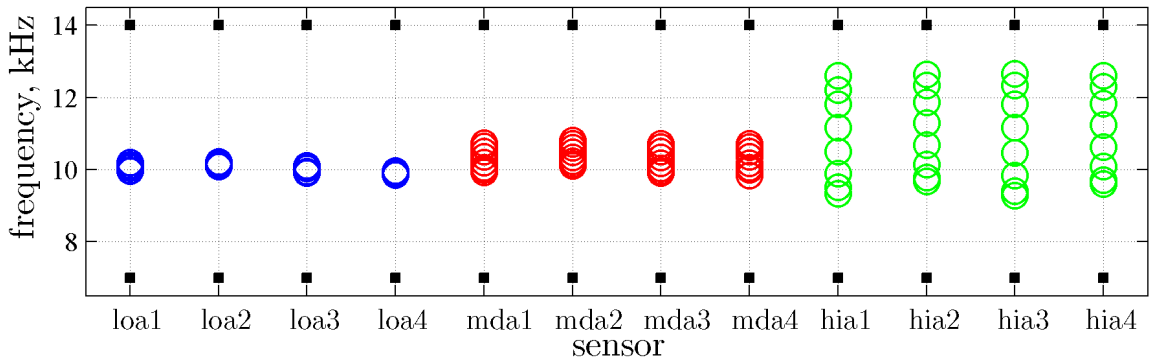

Figure 6.15: Protocol AA: Peak frequencies

The next snapshot of sensor performance will focus on the degree of localization. Response shape plots for one of each of the sensor designs are included in Figure 6.16. The response shapes are clearly spatially harmonic for the strong and moderate coupling sensors. Refer to Appendix A for response shapes for the remainder of the sensors measured in this baseline protocol. The low coupling sensor, loa2, demonstrates essentially full localization, with no discernably sinusoidal shapes. The noted behavior also correlates to the spectra included for the hia2 and loa2 cases in Figure 6.17. Sample hia2 (Figure 6.17a) has a broad bandwidth, spanning roughly 3000 Hz, with widely separated system resonances, each of which involve all of the cantilevers. By contrast, in Figure 6.17b resonant peaks are each dominated by motion of a single cantilever and are packed in a narrow band of roughly 200 Hz.

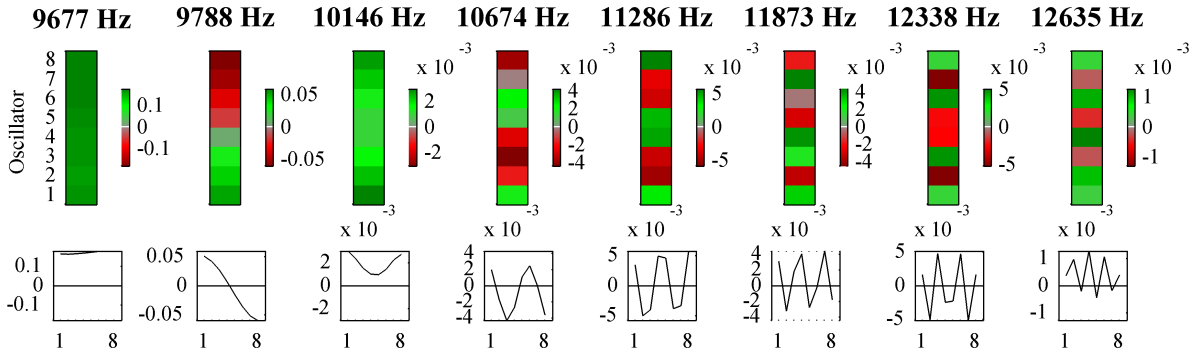

(a) Sensor hia2, strong coupling. Corresponds to spectra in Figure 6.17a

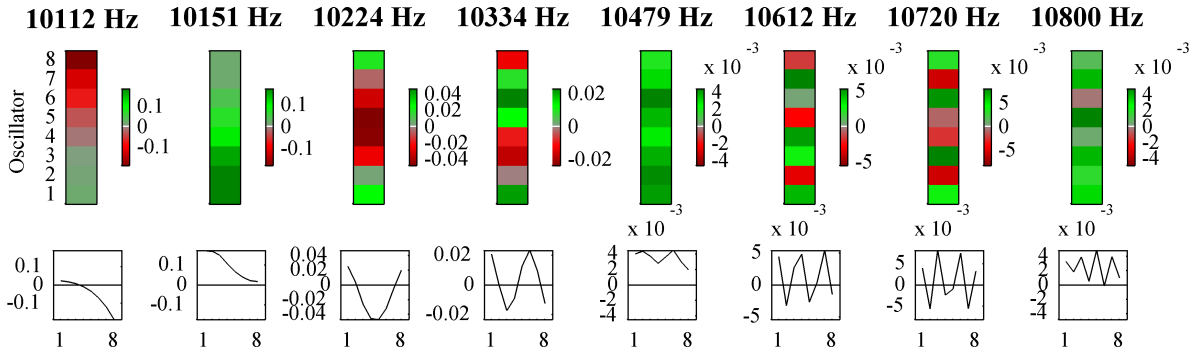

(b) Sensor mda2, moderate coupling.

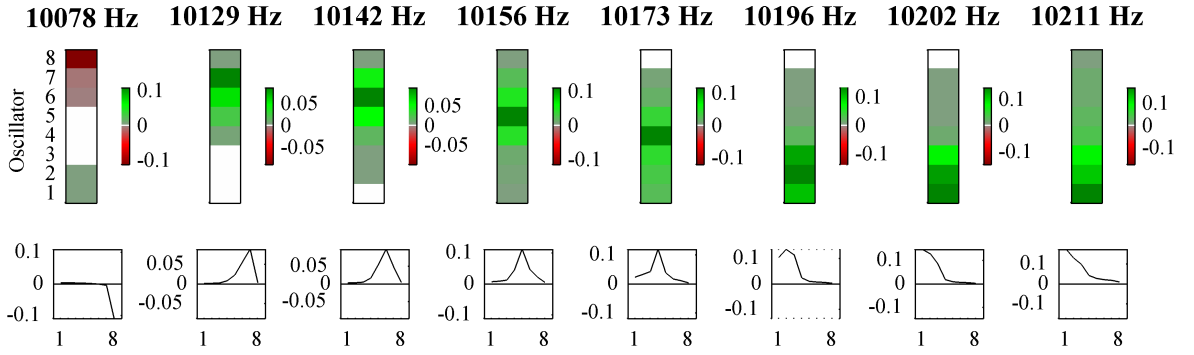

(c) Sensor loa2, low coupling. Corresponds to spectra in Figure 6.17b

Figure 6.16: Protocol AA: Baseline measurements. Response shapes for 3 sensors. Responses are extended for the high and medium coupling strength. Localization is significant in the case of low coupling strength.

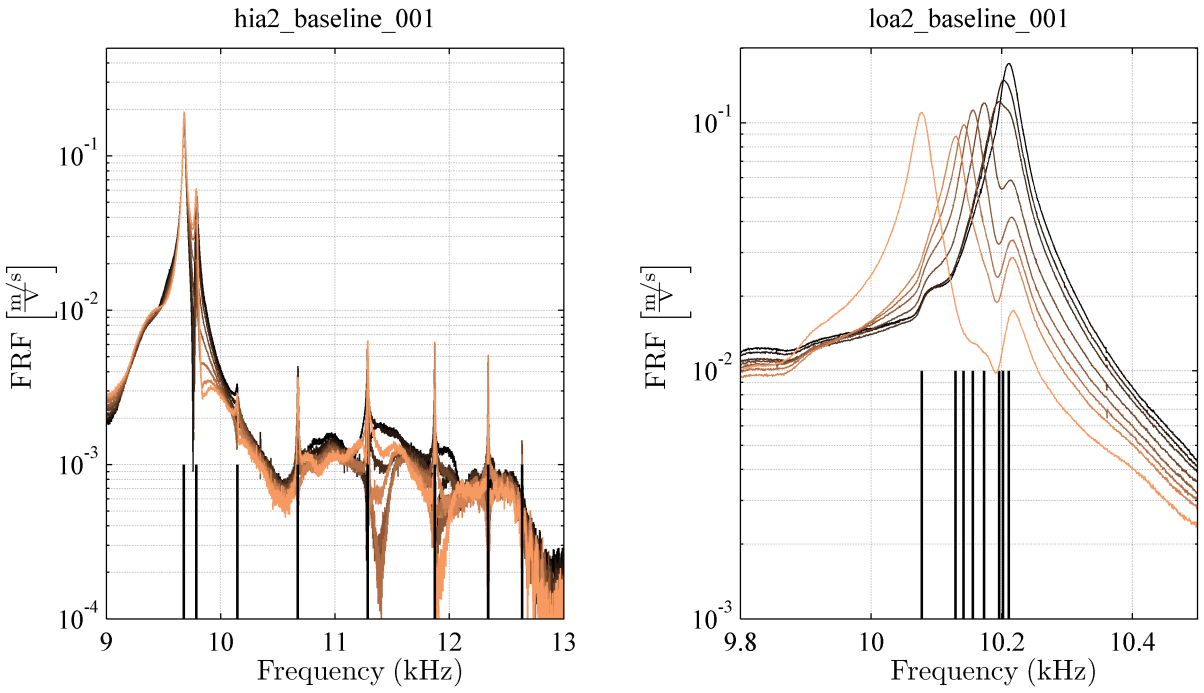

(a) Sensor hia2, strong coupling. Corresponds to response shapes in Figure 6.16a

(b) Sensor loa2, low coupling. Corresponds to response shapes in Figure 6.16c

Figure 6.17: Protocol AA: Baseline measurements, spectra of two sensors. Vertical black lines indicate the eight peak frequencies.

The final look at this baseline set of data is for the mass calculation. Figure 6.18 shows the normalized mass calculated for each cantilever with symbol color corresponding to the coupling strength. Individual sensor results are shown in different symbol shapes; the line represents the mean value for the four sensors of each type. Table 6.4 shows summary statistics along with probability values indicating the likelihood of the pair of groups being drawn from groups with the same mean. Standard deviation increases with coupling strength.

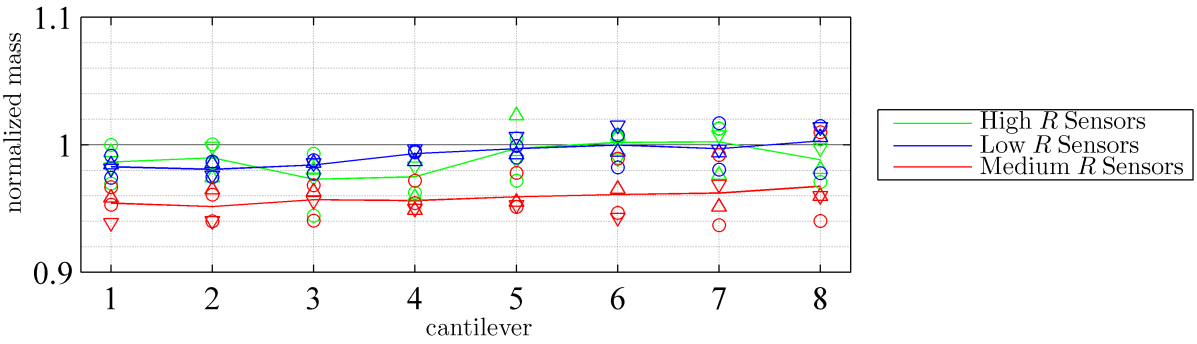

Figure 6.18: Protocol AA: Baseline (empty-cantilever–empty-array) scans on 12 large sensors.

	Mean, $\mu \pm \sigma$		p
Low R	0.992 ± 0.012	low-medium	9×10^{-13}
Medium R	0.96 ± 0.017	high-medium	2×10^{-9}
High R	0.989 ± 0.081	high-low	0.44

Table 6.4: Protocol AA statistics. Listed p-values result from two-tailed two-sample t-tests between the specified sets of data and indicate probability that the difference in the population means is zero.

6.2.8 Protocols A and B: Large array, 4 x steel spheres

The A and B protocols differ only in the set of sensors tested and the overall bandwidth of the chirp excitation. The A protocol includes six sensors. With those preliminary results to confirm the consistency of the fundamental frequency and bandwidth of these type 4 sensors, the chirp bandwidth was reduced to 9-14 kHz in subsequent protocols to bracket the range of sensor bandwidths more closely. The B protocol includes a total of 13 sensors. The results for the A protocol studies are not presented individually here, but are included in Section 6.3.1 which uses the A and B protocol results together to investigate sensor repeatability.

Similar to Protocol 6, Protocols A and B follow the one-location-at-a-time loading procedure. However, in this case, each sensor is measured for five different load levels (0 to 4 steel spheres, corresponding to 0, 177, 354, 531, and 708 μg). Therefore, each sensor is measured a total of 40

times. As such, each cantilever is also measured 40 times: five measurements for which the loading conditions are applied to it, and 35 measurements for which there is a load on a *different* cantilever (empty-cantilever–loaded-array). Since one of the five loading levels is actually zero load, one measurement on each cantilever is an empty-cantilever–empty-array measurement. The scans are completed in the following sequence. Beginning with the first cantilever, scans are completed with sequential loading before advancing to the second cantilever and so on, as shown in Table 6.5.

	LDV Scan															
	1	2	3	4	5	6	7	8	9	10	11	12	...	38	39	40
n=1	0	177	354	531	708	0	0	0	0	0	0	0	...	0	0	0
n=2	0	0	0	0	0	0	177	354	531	708	0	0	...	0	0	0
n=3	0	0	0	0	0	0	0	0	0	0	0	177	...	0	0	0
n=4	0	0	0	0	0	0	0	0	0	0	0	0	...	0	0	0
n=5	0	0	0	0	0	0	0	0	0	0	0	0	...	0	0	0
n=6	0	0	0	0	0	0	0	0	0	0	0	0	...	0	0	0
n=7	0	0	0	0	0	0	0	0	0	0	0	0	...	0	0	0
n=8	0	0	0	0	0	0	0	0	0	0	0	0	...	354	531	708

Table 6.5: Protocol A and B loading conditions: 40 LDV scans per sensor with five mass loading amounts (0, 177, 354, 531, and 708 μg)

Therefore, in the plots in Figure 6.19, for each cantilever there is one measurement per sensor at each loading level (filled color symbols), and 36 measurements at zero load (small open black circle in Figure 6.19). There are four sensors with high coupling strength, as shown in Figure 6.19a, therefore there are four filled color symbols at each mass loading level—one per sensor. Likewise, there are four medium and five low coupling sensors. Different loads are represented with different color and shape. The zero load condition is indicated by the black line and large empty circles. The low coupling results in Figure 6.19c shows substantially higher scatter in the no-load measurement points, but still indicate a clear trend of increasing calculated mass with increased load.

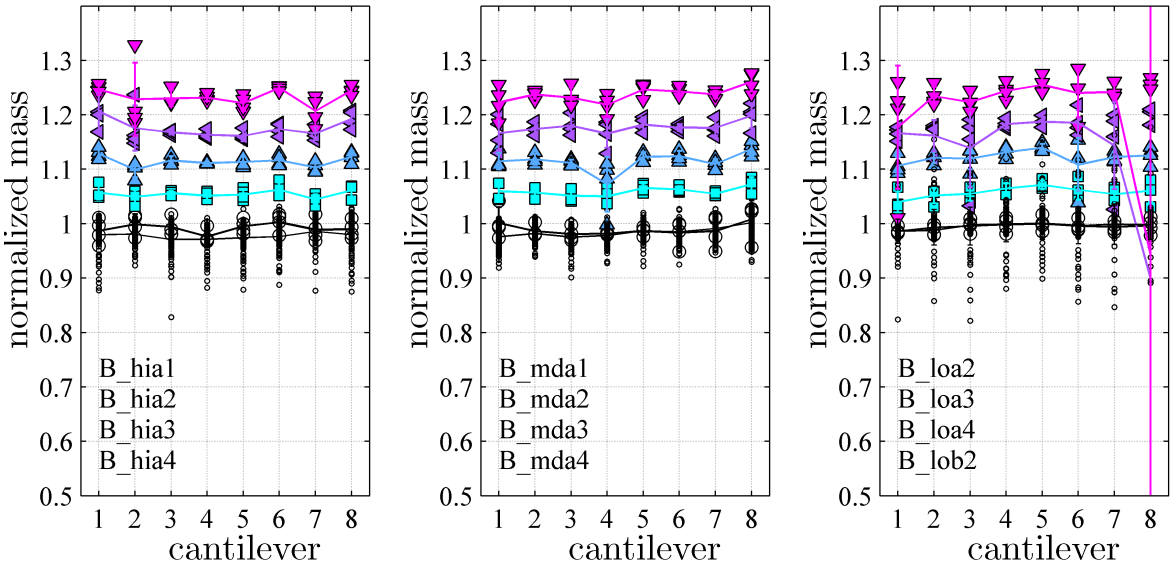

(a) High R, 4 samples (b) Medium R, 4 samples (c) Low R, 5 samples

Figure 6.19: Protocol B: Mean mass calculations using sensors with three different levels of coupling ratio, R, with 5 levels of added mass: 0, 177, 354, 531, and 708 μg. Mean value at each loading level is indicated by each colored line with error bars for the standard deviation.

6.2.9 Protocol B2: Large array, 7 x glass spheres, 3 sensors

This protocol uses sequential loading on each cantilever in the same manner as Protocols A and B. In this case, the load is glass beads, with a nominal mass of 27 μg. The lowest mass loading level from Protocol A/B is a single steel sphere with mass 177 μg. In order to ensure overlap in the range of mass loading between Protocol B and B2, the maximum loading condition will be seven glass beads, for a total mass of 189 μg. Including the no-load scans, there is a total of eight load increments for this study, for a total of 64 scans per sensor. A subset of three sensors, one at each mass level, are selected for this measurement protocol: loa1, mda1, and hia2. Figure 6.20 shows the mass calculation results for these sensors. Sensor mda1 shows moderate scatter, particularly in the empty-cantilever–loaded-array points (small black circles). Sensor loa1 shows pronounced scatter in both the empty-cantilever–loaded-array measurements, and the measurements of the cantilevers with mass. By simple observation of the color distribution, the general trend of a higher normalized

mass corresponding to a higher loading state still exists. However, the *difference* in the amount of scatter relative to the sensors with medium or high coupling strength when placed under the lighter loading conditions of this protocol, when compared to the *difference* in scatter among coupling strength with the heavier loading amounts of Protocol B is striking. Specifically, a comparison of Figure 6.20c with respect to Figure 6.20a contrasted with Figure 6.19c with respect to Figure 6.19a shows how the low coupling suffers under light loading conditions.

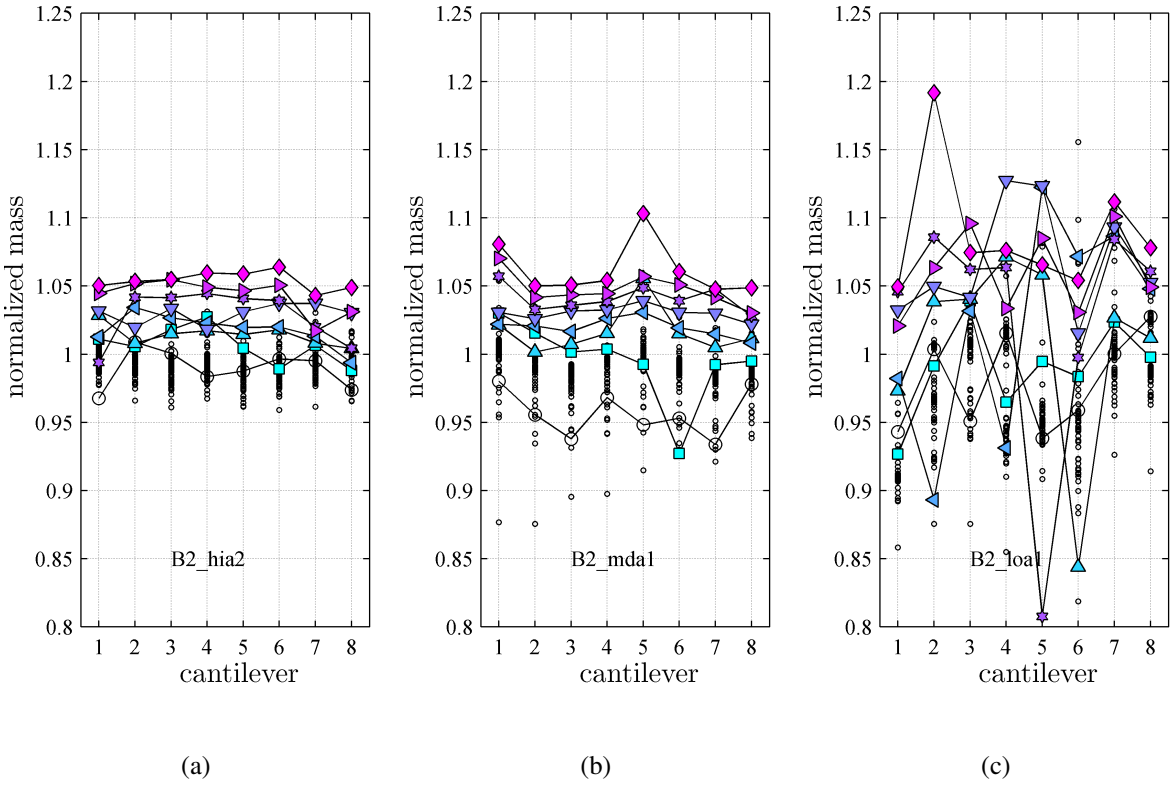

Figure 6.20: Protocol B2: Glass sphere loading, single sensor plots. Eight load amounts: 0, 27, 54, 81, 108, 135, 162, and 189 μg

6.2.10 Protocol B3: Large array, 7 x polystyrene spheres, 3 sensors

Protocol B3 is identical to Protocol B2 in every respect except the added mass material. In this case, polystyrene beads with a nominal mass of 9 μg are used in place of glass (27 μg).

Load amounts are 0, 9, 18, 27, 36, 45, 54, and 63 μg. As shown in Figure 6.21c, the loa1 sensor demonstrates significant scatter at all loading levels for this protocol.

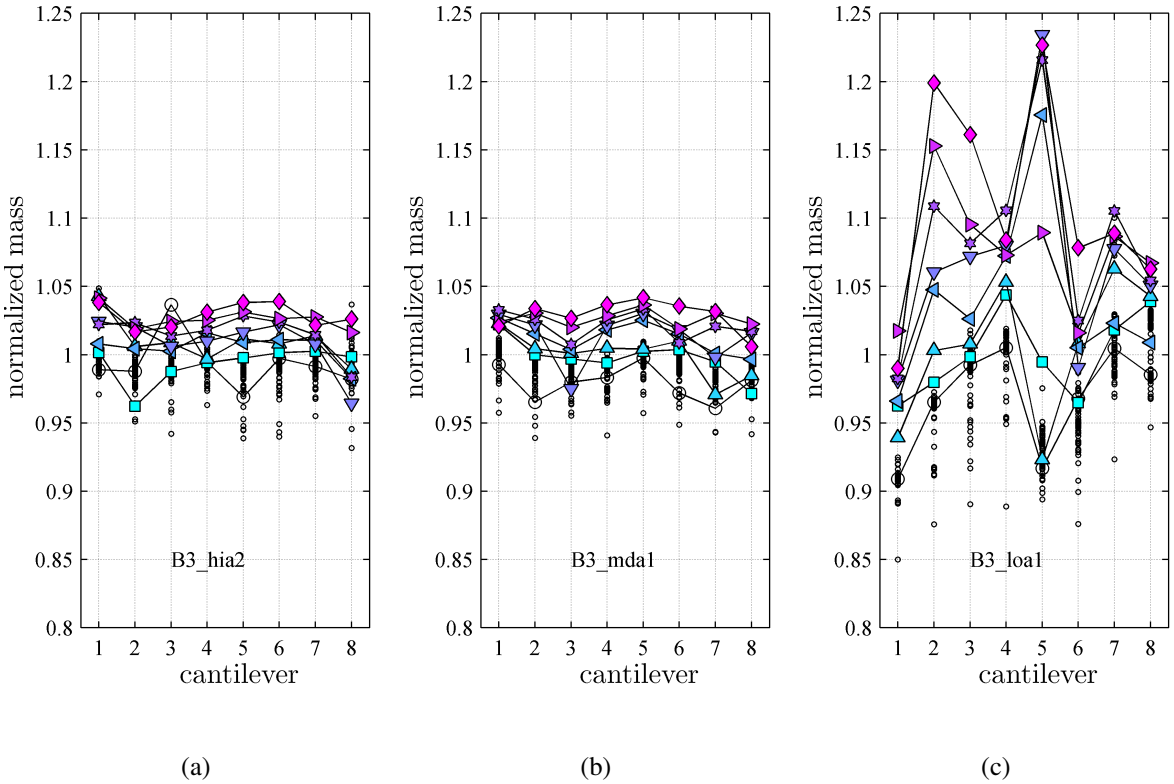

Figure 6.21: Protocol B3: Polystyrene sphere loading, single sensor plots.

Figure 6.22 shows a probability map for the detection threshold based on the polystyrene loading results given the null hypothesis that a particular loading level and the unloaded state have the same mean. Each gray region represents a level of significance, α. For each loading level, the probability is given for loa1 (blue), mda1 (red), and hia2 (green) for each of the loading amounts. Above the boundary line for that particular α level, the null hypothesis cannot be rejected. In other words, the resulting mass calculation is stastistically indeterminate from the zero load state with a significance level of α for the points above the α region.

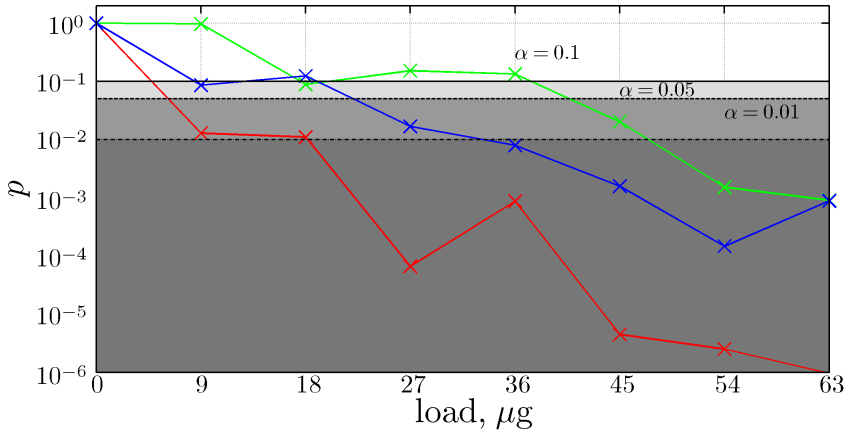

Figure 6.22: Statistical indicator of detection threshold for one sensor of each coupling strength: Low coupling (blue): Sensor loa1. Medium coupling (red): Sensor mda1. High coupling (green): Sensor hia2.

6.2.11 Protocol E: Large array, multiple loading locations, 12 sensors

The purpose of this protocol is to subject the sensors to multiple simultaneous loads for each scan. A total of twelve sensors—four at each of the three coupling strengths—are measured with a total of 17 different loading states listed in Table 6.6. Mean values are calculated for all of the loaded cantilevers for a given total load amount (i.e. for the three location loading case, there are 15 total loaded cantilever locations and 4 sensors, so the mean is calculated with 60 values). These mean values are listed to the right of the rows of plots in Figures 6.23, 6.24, and 6.25.

Steel spheres which are slightly larger than those used in earlier protocols are selected to ensure clarity of signal. The spheres used in this study have approximate diameter of 460 μm and mass 400 μg, which should correspond to a normalized mass amount of 1.17. Figures 6.23, 6.24, and 6.25 show compiled results for all loading locations, and all sensors. As with other figures, an open black symbols indicates an unloaded cantilever. The filled colored symbols indicate a loaded cantilever. Different symbols, each of which has a corresponding color intensity, represent different sensors.

Load Amount	Cantilever Combinations				
No Load	none				
2 Locations	1-2	1-4	1-7	3-4	3-5
3 Locations	1-2-3	1-3-5	1-4-7	1-7-8	3-4-5
4 Locations	1-2-3-4	1-3-6-8	2-4-6-8	2-3-4-8	3-4-5-6
All Cantilevers Loaded	1-2-3-4-5-6-7-8				

Table 6.6: Protocol E mass loading locations, 400μg steel spheres

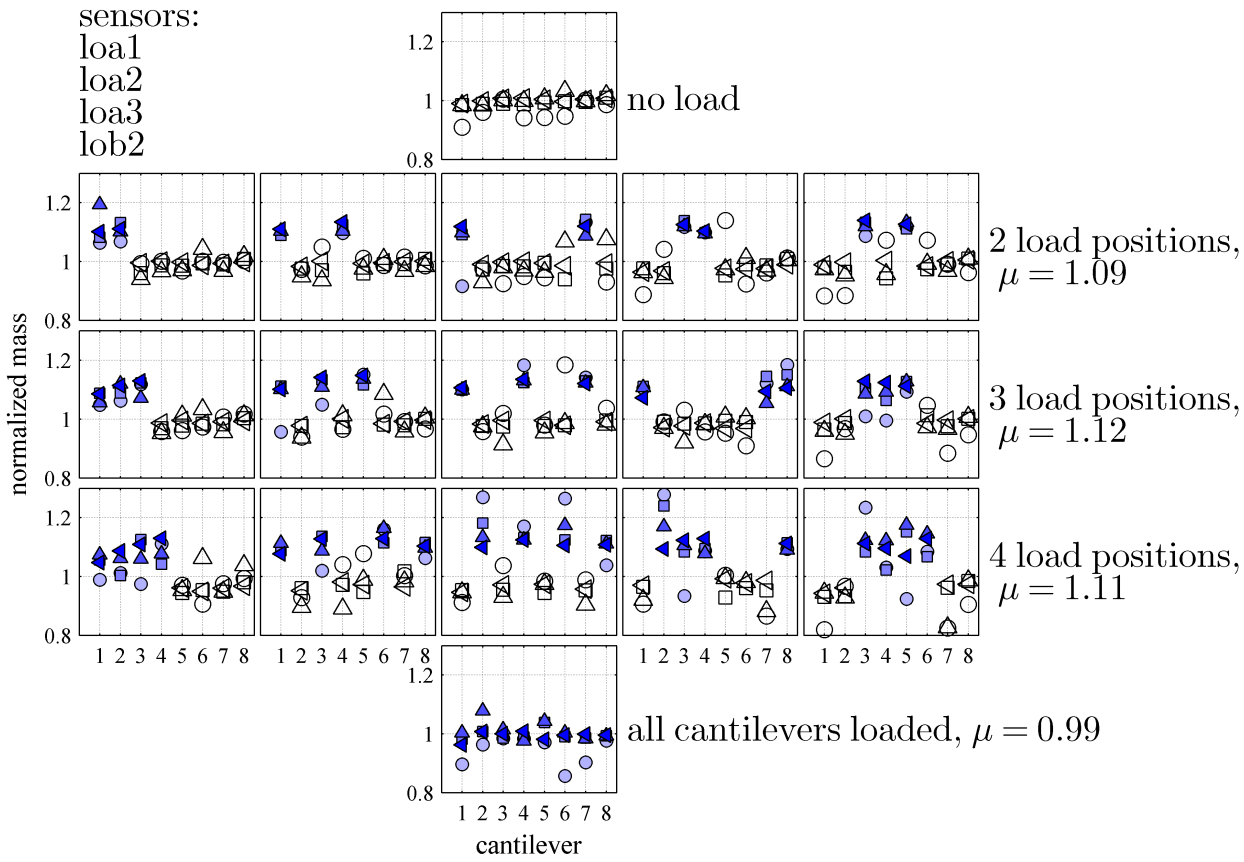

Figure 6.23: Protocol E: Multiple loading locations, low *R*

The results for the no load and equally loaded cases (row 1 and row 5 in each of the three figures) both indicate a uniform calculated mass of 1. This behavior is an artifact of the calculations being based on individual, isolated observations without the use of a reference state. The results

of the 2-, 3-, and 4 loading position cases demonstrate the artifact via reduction in calculated mass for the unloaded cantilevers in a given array.

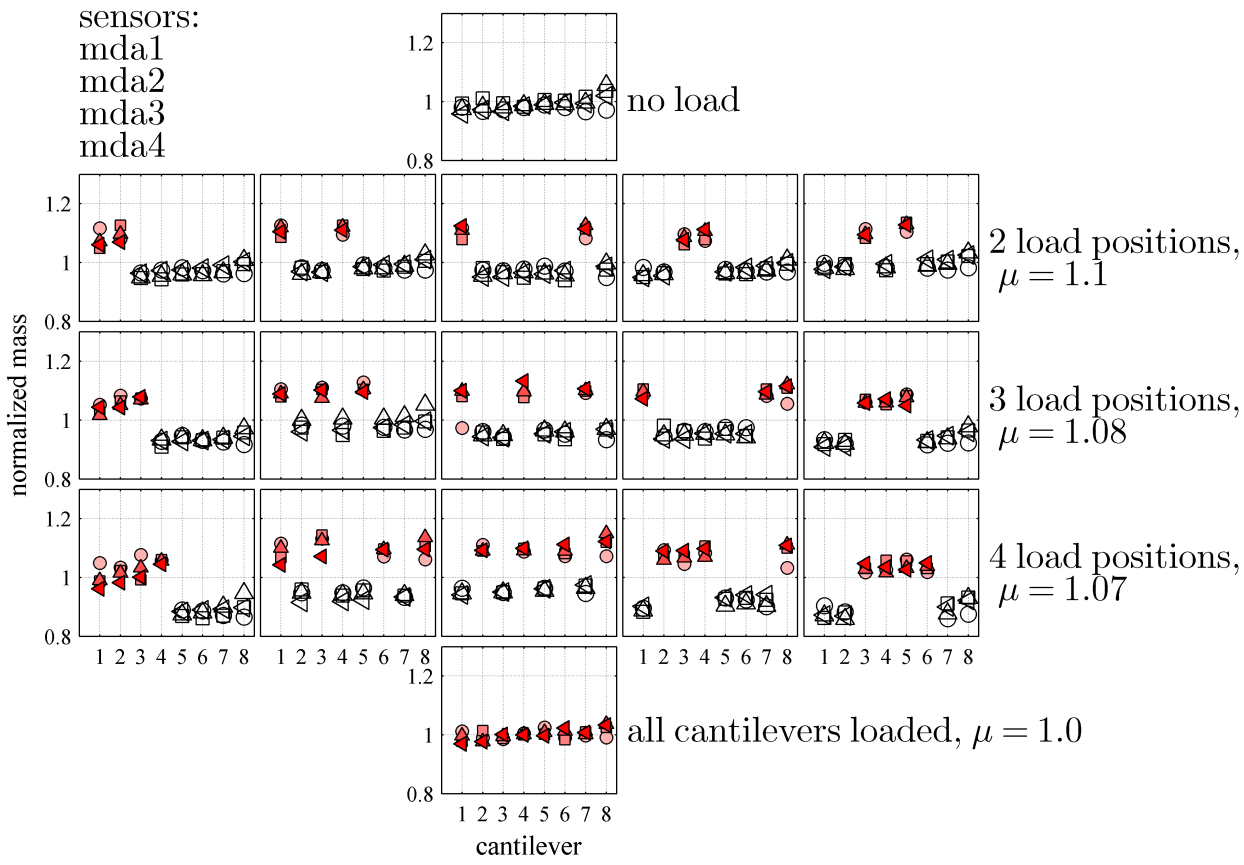

Figure 6.24: Protocol E: Multiple loading locations, medium *R*

The mean normalized mass values indicated at the right end of each row range from 1.07 to 1.12, which is substantially lower than the 1.17 indicated by the model from Section 5.3.4. However, when considering the *net* difference in normalized mass between the mean for the cantilevers with no load and the mean for the loaded cantilevers for each given loading case, the value is in line with the model prediction.

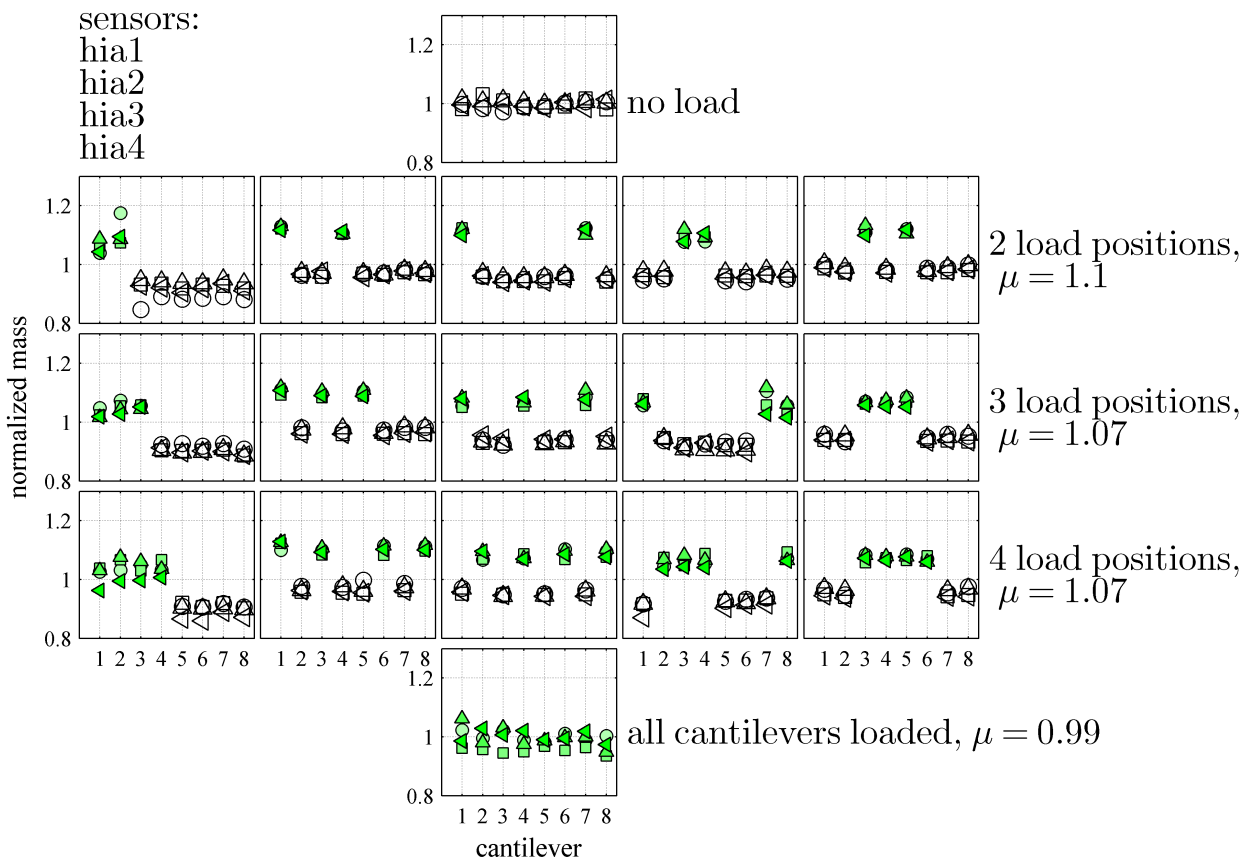

Figure 6.25: Protocol E: Multiple loading locations, high *R*

6.3 Analysis: Multiple Protocols

This section takes experimental results from multiple protocols to examine several aspects of sensor behavior. First is the issue of sensor repeatability, in Section 6.3.1. Section 6.3.2 examines sensor linearity by presenting individual sensor data with both steel and glass loading conditions. Section 6.3.3 also addresses sensor linearity with regression analysis for the different coupling strength values. This chapter closes with a compilation of the observed coupling ratio values for across all sensors and protocols in Section 6.3.4.

6.3.1 Same sensor repeatability

This section uses six paired studies to examine the repeatability of the sensor results. The A and B protocols are identical in mass loading and data collection procedure. Table 6.7 shows the sequential loading locations for a single loading amount. The large array sensors used in both protocols include two high-R, two medium-R, and two low-R for a total of six individual sensors. Figure 6.26 shows representative mass loading plots for three of the sensors. Similar to earlier figures, the empty cantilever, loaded array cases are open black circles. Loading amount is indicated by color, with cyan for no load ranging through magenta for 4 spheres (708 μg). Data from protocol A are filled symbols, and Protocol B is represented by open symbols. The spread in the empty cantilever, loaded array mass estimates varies drastically from the high-R sensor in Figure 6.26a to the low-R in Figure 6.26c. In Figure 6.26a, none of the unloaded cantilever values (cyan square or black circles) exceed the corresponding value for the 177 μg (1 sphere) load. In the case of moderate R, there is a small degree of overlap between these value ranges, while the empty array estimates for the low-R case in Figure 6.26c range from 0.7 to greater than 1.3.

Figure 6.27 characterizes the phenomenon in Figure 6.26 in terms of standard deviation of the difference between the two sets of calculations. For a given loading amount, each sensor has a total of 64 measurements: eight of loaded cantilevers, and 56 of unloaded cantilevers. A simple error metric is the difference, δ, in the measurements from the two protocols. The standard deviation of these δ values is an indicator of measurement repeatability. The loading pattern description in Table 6.7 also helps to illustrate the calculations. The standard deviation of the eight δ values along the diagonal represents variability at that load level. The standard deviation of the 56 remaining off diagonal δ values indicates variability in the empty cantilever-loaded array state for that particular load level.

The filled circles in Figure 6.27 represent the standard deviation of the δ values from the loaded states, and the open circles are the standard deviation of the remaining 56 δ values for the measurements of unloaded cantilevers. As an example, the filled red circle at the 0% location in

		LDV Scan Number							
		1	2	3	4	5	6	7	8
Cantilever	n=1	load	0	0	0	0	0	0	0
	n=2	0	load	0	0	0	0	0	0
	n=3	0	0	load	0	0	0	0	0
	n=4	0	0	0	load	0	0	0	0
	n=5	0	0	0	0	load	0	0	0
	n=6	0	0	0	0	0	load	0	0
	n=7	0	0	0	0	0	0	load	0
	n=8	0	0	0	0	0	0	0	load

Table 6.7: Measurement procedure for a single loading amount (e.g. 177 μg, 1 sphere)

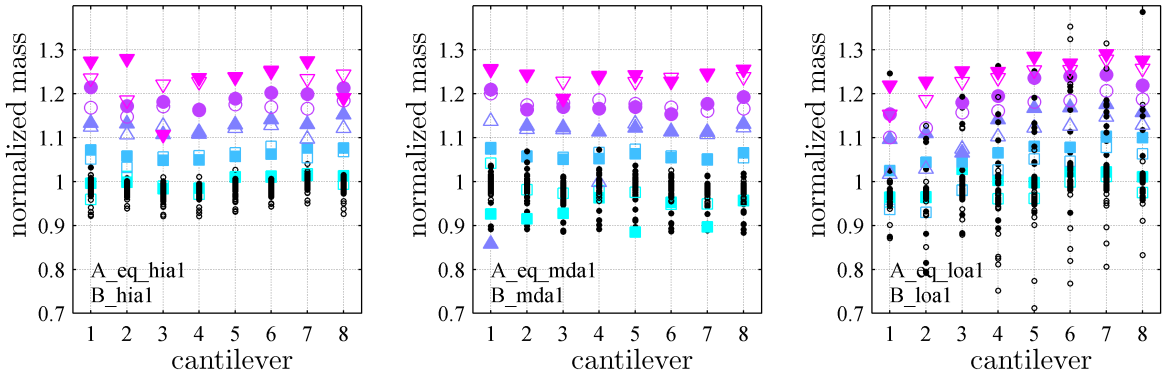

(a) High R (b) Medium R (c) Low R

Figure 6.26: Comparison of duplicate measurement sets on the same three sensors. First measurement, filled symbols, second measurement, open symbols. Mass loading levels: 0, 177, 354, 531, and 708 μg.

Figure 6.27 is the standard deviation of the difference between the eight filled cyan squares and the eight empty cyan squares in Figure 6.26a. The filled red circle at the 8% location in Figure 6.27 is the standard deviation of the difference between the magenta triangles, and so on. Although the analysis is on a limited number of sensors, Figure 6.27 quantifies the increase in spread noted with decreasing coupling strength in Figure 6.26.

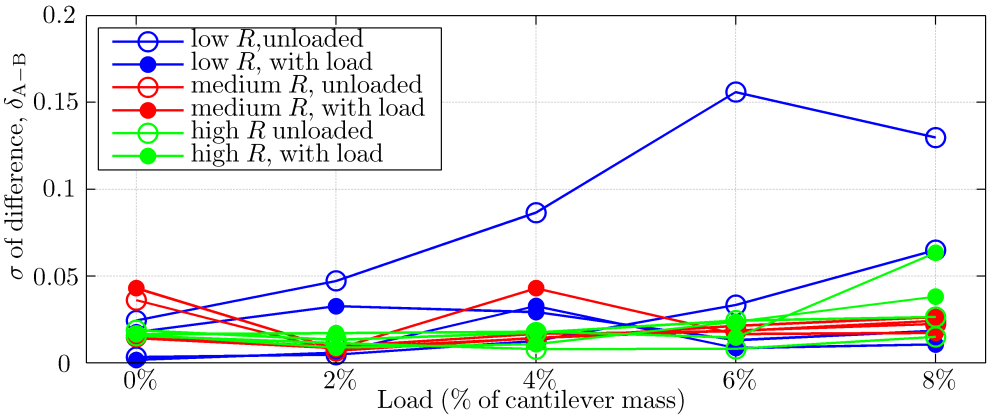

Figure 6.27: Sensor repeatability: standard deviation of differences in repeat scans

6.3.2 Compilation of Protocol B and B2: Steel and glass bead loading

In contrast to Section 6.3.1, which compared duplicate measurements on the same sensors, this section presents the results of two different load ranges applied to the same three sensors. The two loading ranges are [0 177 354 531 708] μg (protocol B, steel beads), and [0 27 54 81 108 135 162 189] μg (protocol B2, glass beads). Note that the smallest steel load (177 μg) is slightly smaller than the largest glass load (189 μg), creating a small amount of overlap in the loading conditions. Similar to the presentation of the loading data in previous sections, the incremental loading conditions are represented by smooth color transitions. The glass loading is represented by squares in the familiar magenta to cyan range, while the steel is shown as triangles in steps moving from yellow to red. The empty cantilever-empty array condition is the empty corresponding shape. In this set of plots, the empty cantilever-loaded array measurements are included as lines with error bars representing $\mu \pm \sigma$(mean $\pm$ one standard deviation). One key observation is that the cyan square, representing the heaviest glass load (189 μg glass), should be consistently higher than the light yellow triangle (representing the lightest steel load (177 μg steel)) but is only occasionally so. The other notable feature of the three plots is the generally increasing scatter in the no load and lighter load cases. This observation will be quantified in Section 6.3.3.

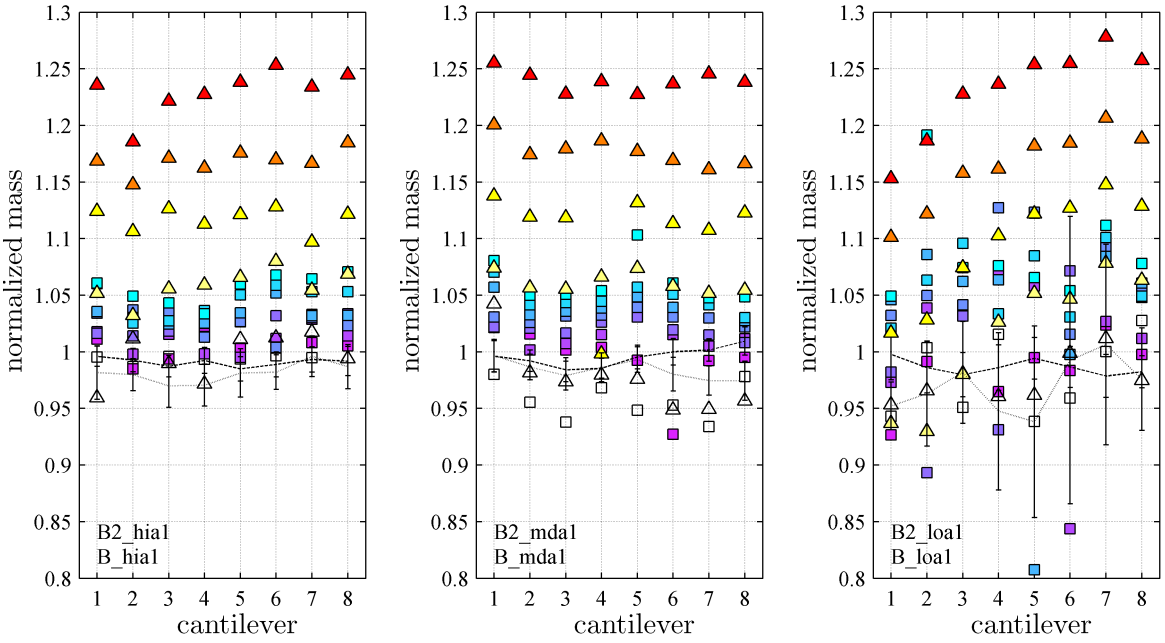

(a) Sensor hia1 (b) Sensor mda1 (c) Sensor loa1

Figure 6.28: Glass and steel sphere loading on same sensor. Solid black line: $\mu \pm \sigma$ of empty cantilever-loaded array measurements during B protocol (steel masses) $\triangle$: empty cantilever-empty array during B protocol (steel masses) Dotted black line: $\mu \pm \sigma$ of empty cantilever-loaded array measurements during B2 protocol (glass masses) $\square$:empty cantilever-empty array during B2 protocol (glass masses)

6.3.3 Normalized mass and load relationship: B, B2, B3

This section presents the relationship between the amount of mass added to a cantilever and the calculated normalized mass. As discussed during the derivation of the coupling ratio expression in Section 5.2.2, as well as in the mass addition protocol description in Section 5.3.4, the expected slope of this loading curve is $4.29 \times 10^{-4} \frac{1}{\mu g}$. The three plots in Figure 6.29 show the combined steel, glass, and polystyrene loading conditions for each coupling ratio.

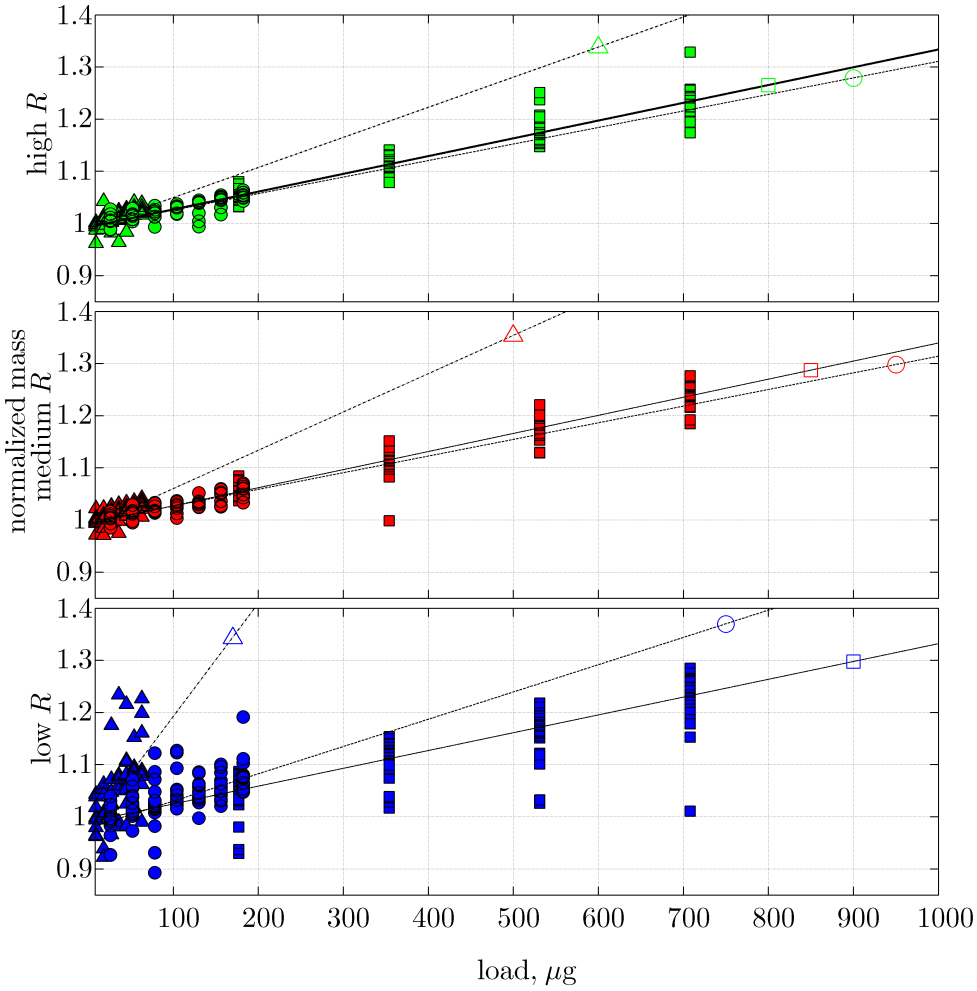

Figure 6.29: Load versus calculated mass

For this analysis, data from three protocols are pooled: 12 sensors from protocol B (1-4 steel beads, 177 μg each), 3 sensors from protocol B2 (1-7 glass beads, 27 μg each), and 3 sensors from protocol B3 (1-7 polystyrene beads, 9 μg each). Symbol shape corresponds to load type with squares for steel, circles for glass, and triangles for polystyrene. A linear regression is performed for each load type at each coupling ratio. The regression lines are identified with a corresponding open shape. These results again demonstrate not only the deterioration of sensor performance in the low coupling case, but also a dependence on load level.

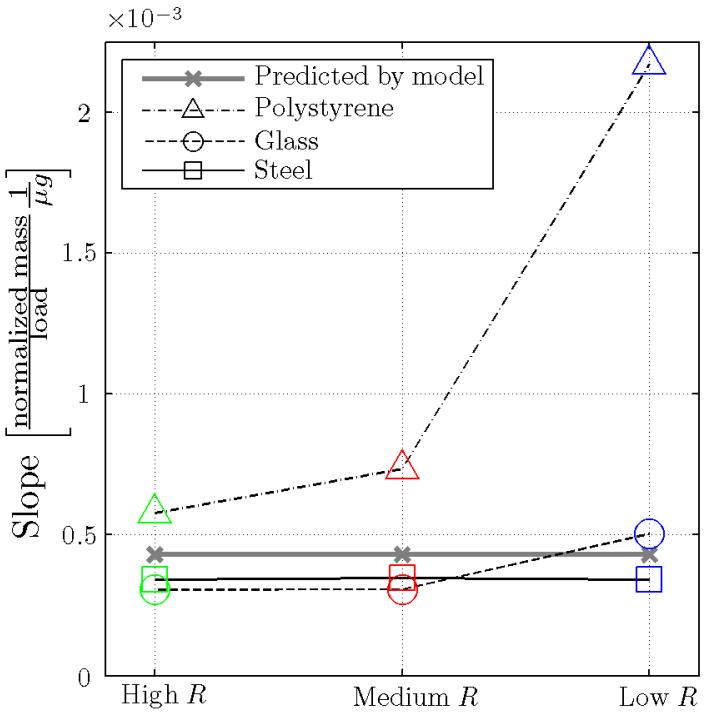

Figure 6.30: Slopes of loading curves for ranges of load and three coupling ratios

Figure 6.30 shows the slopes from the regressions in Figure 6.29 with corresponding color and shape. The gray line indicates the expected slope value from the model ($4.29 \times 10^{-4} \frac{1}{\mu g}$). The high coupling sensor demonstrates the most consistent slopes while the low coupling sensor slope values demonstrate a nearly fivefold difference for the different load ranges. Additionally, the slopes indicated from the polystyrene loading are consistently higher than expected.

6.3.4 Coupling Ratio

Figure 6.31 shows the compiled values calculated for the coupling ratio, R, using all available data for each sensor. Each R value is the mean of three different bandwidth estimates. The detailed procedure used to calculate R is described earlier in Section 6.1.3. The sensor design process, described in Section 5.2.3, targeted R values for these large array sensors of R =0.03 for the 1000 μm gap design, R =0.003 for the 250 μm gap design, and "as low as practicable for our testing assem-

bly" in the third design with no coupling beam. The observed average values are R =0.22, 0.045, and 0.013 respectively. While the sensors demonstrate far higher coupling than the model used for designing the geometry indicated, the variation in the coupling within each design is low with standard deviations roughly an order of magnitude smaller than the coupling ratios themselves.

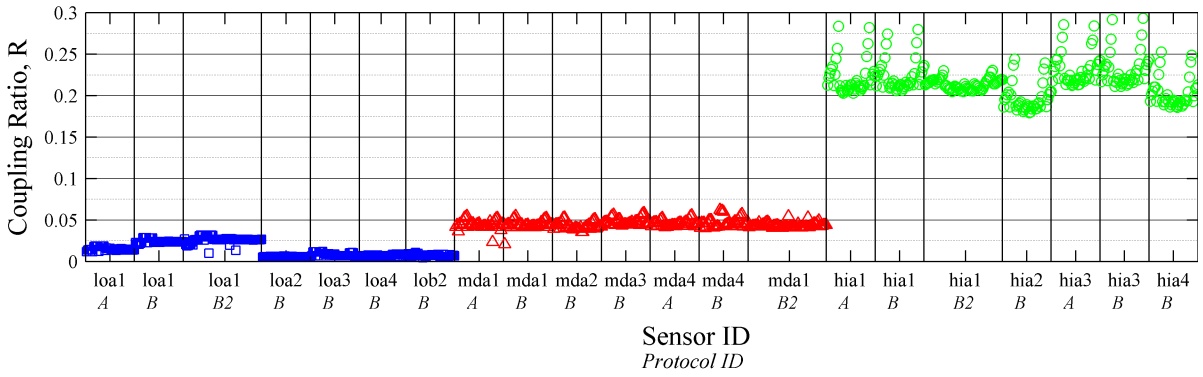

Figure 6.31: Coupling ratios, R, determined from the measured bandwidth of each sensor. Values for R are given as $\mu \pm \sigma$. Low coupling (blue): $R = 0.013 \pm 0.008$. Medium coupling (red): $R = 0.045 \pm 0.005$. High coupling (green): $R = 0.22 \pm 0.02$

6.4 Comparison to Numerical Simulation

This section first discusses the calculations to determine equivalent metrics for the experimental data that will allow for comparison to the numerical simulation work presented in Chapter 4. In Figures 4.5 and 4.6, the results are presented as sensitivities as a function of normalized mass disorder σ_m/R with

$$\text{Sensitivity, } S = \frac{\sigma_{\text{error}}}{\sigma_{\text{noise}}} \tag{6.5}$$

In this discussion, the standard deviation of the mass values calculated from multiple measurements of the same loading condition will be termed σ_e. All measurements considered here are made by the same system under the same operating conditions such that σ_{noise} is constant. With

this assumption of constant noise, the σ_e calculated in this section is proportional to $\frac{\sigma_{error}}{\sigma_{noise}}$ from Chapter 4 and thus will be used in place of the sensitivity, S.

For any of the single loading location protocols (A, B, B2, B3), an LDV scan is done with the specified mass amount, z, placed on each of the eight cantilevers in successive measurements, as illustrated earlier in Table 6.7. That set of eight scans corresponds to a single loading condition, which also corresponds to an 8×8 matrix of calculated masses. As illustrated in Equation 6.6, that two-dimensional matrix can be considered to be a “page" of data. Extending that analogy, each loading condition has a corresponding two dimensional page of data that can stack into a three dimensional data “box" with as many pages as loading conditions. The data from each page is then rearranged as shown in Equation 6.7 to determine the standard deviations.

Equations 6.6 and 6.7 illustrate the process to calculate a value for both σ_e—the indicator of the quality of the measurement—and σ_m—the indicator of the disorder in the array. The mean of the standard deviations of mass calculations at the same loading level is σ_e, while the mean of the standard deviations of mass calculations for the same cantilever is σ_m. The range of loading conditions in each protocol ensure a range of values for σ_m, in addition to the range of values for R from the three array designs. These two ranges of values give a span of σ_m/R values for the plot to compare experiment to simulation.

$$\text{“Page” of measurement “box”} \rightarrow \begin{bmatrix} z & b & c & d & e & f & g & h \\ a & z & c & d & e & f & g & h \\ a & b & z & d & e & f & g & h \\ a & b & c & z & e & f & g & h \\ a & b & c & d & z & f & g & h \\ a & b & c & d & e & z & g & h \\ a & b & c & d & e & f & z & h \\ a & b & c & d & e & f & g & z \end{bmatrix} \rightarrow \text{rearrange} \rightarrow \quad (6.6)$$

$$\begin{bmatrix} z & [] & b & c & d & e & f & g & h \\ z & a & [] & c & d & e & f & g & h \\ z & a & b & [] & d & e & f & g & h \\ z & a & b & c & [] & e & f & g & h \\ z & a & b & c & d & [] & f & g & h \\ z & a & b & c & d & e & [] & g & h \\ z & a & b & c & d & e & f & [] & h \\ z & a & b & c & d & e & f & g & [] \end{bmatrix} \downarrow \xrightarrow{\text{standard deviation}} \begin{bmatrix} \sigma_{m_1} \\ \sigma_{m_2} \\ \sigma_{m_3} \\ \sigma_{m_4} \\ \sigma_{m_5} \\ \sigma_{m_6} \\ \sigma_{m_7} \\ \sigma_{m_8} \end{bmatrix} \downarrow \text{mean} \Rightarrow \sigma_m$$
$$\left[\sigma_{e_z}\ \sigma_{e_a}\sigma_{e_b}\sigma_{e_c}\sigma_{e_d}\sigma_{e_e}\sigma_{e_f}\sigma_{e_g}\sigma_{e_h}\right] \xrightarrow{\qquad\qquad\qquad\qquad\qquad\qquad} \text{mean} \Rightarrow \sigma_e \tag{6.7}$$

Figure 6.32 is analogous to Figure 4.5 from the numerical simulations. It should be noted that while Figure 4.5 presents data for a range of array sizes ($N = 5$ to $N = 1000$) and two very different coupling ratios ($R = 0.1$ and $R = 0.001$), these experimental results are for only one array size, $N = 8$, and a set of coupling ratios that span roughly one order of magnitude ($R \approx$0.2, 0.05, and 0.02).

As with other figures throughout the work, blue corresponds to the low R sensors, red to medium, and green to high R sensors. Data points for any given sensor are connected. Results from the A or B protocols are the darker red, blue or green. Results from the B2 and B3 protocols are the corresponding lighter red, blue, or green. The vertical line is at the value of $(\sigma_m/R) = 1/\sqrt{N}$. Generally, the experimental results are consistent with the findings from the simulations. To the right of the transition, sensors demonstrate increasingly localized responses. Mass calculation quality, as indicated here by σ_e degrades. To the left, the sensors are insensitive to the amount of mass disorder. Figures 6.20 and 6.21 clearly illustrate that the experimental results bracket this transition in behavior, and that the value of the transition is consistent with the simulation results. In some cases, the medium R sensors demonstrate largely extended responses, and at other times, localization is evident.

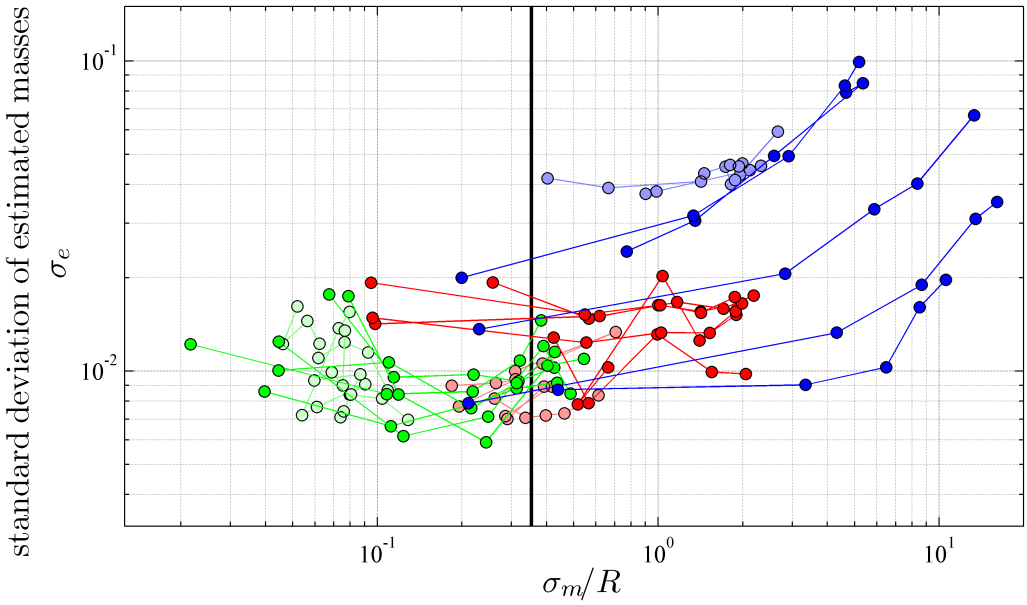

Figure 6.32: Standard deviation of calculated masses for different coupling strengths

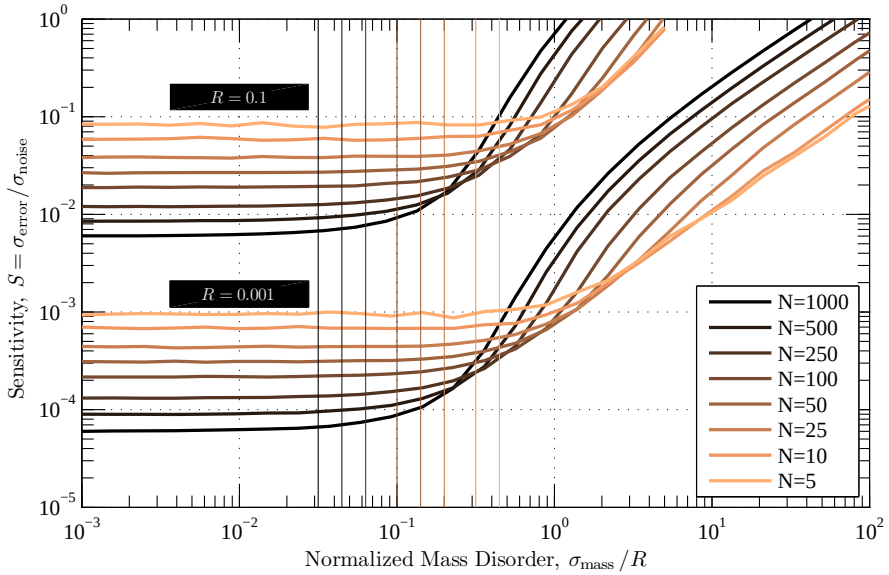

Figure 6.33: Reprint of Figure 4.5. Sensitivity of the mass identification technique to measurement noise, as a function of mass disorder. The values at which $(\sigma_{\text{mass}}/R) = 1/\sqrt{N}$ are indicated by vertical lines for each value of N.

CHAPTER 7

CONCLUSIONS

7.1 Conclusions

Generally, the dissertation is the primary deliverable resulting from one's time as a graduate student. It is the tangible evidence of the discovery and learning that has taken place. I take this opportunity to mention a few items beyond the words and figures in this manuscript. In addition to a few conference proceedings[224–228] and a journal article,[229] another tangible result of my time at the Catholic University of America is the experimental test facility I have assembled in the Center for Acoustics Vibrations and Structures. The basic control software architecture for the scanning LDV system was heavily borrowed from a similar system built by colleagues in this lab,[230] but the new system required assembly and validation. My contributions include substantial control software modifications to interface with different linear stages, controllers, and data acquisition hardware as well as enhancements to incorporate the environmental monitoring and sample location function via vibrometer signal mapping. Together with the custom data processing software, the system is a comprehensive, flexible tool for measurement and analysis of vibration in structures from ranging in size from small to microscale. It has been used for demonstrations and experiments in both graduate and undergraduate courses here at CUA.

As for the content of this manuscript, the broad purpose is the investigation of localization phenomenon. Presentation of the technical basis for and results of this investigation, as well as its significance and broader impact is the purpose of this document. The vehicle for the investigation

is a system of coupled resonators used as a mass sensor. The sensor algorithm determines system masses from measured system eigenmodes. Numerical simulation investigates the sensitivity of the mass determination method to noise. Simulation results show that array sensitivity to noise is divided into two regimes. In cases of extended modes, when the localization length of the array is comparable to or smaller than the array itself, mass identification is insensitive to changes in array disorder. Array responses demonstrate significant localization and a corresponding increase in sensitivity to noise when normalized mass disorder exceeds a transition value that is related to array size. In the extended mode regime, for a given amount of coupling strength, arrays with a large number of oscillators have lower sensitivity. Similarly, arrays with lower coupling strength have lower sensitivity to noise. For a given combination of coupling strength and amount of mass disorder, there is an optimum array size in which the localization length is comparable to the array size. That combination of array parameters yields the minimum sensitivity to noise.

The numerical simulation work is paired with experimental testing of a set of prototypes. The experimental results demonstrate a functional method for mass detection using a coupled array of eight resonant cantilevers. In studies with a single mass added to a single cantilever, the sensor is linear and highly repeatable for loading levels ranging from 0.1% to 9% of the mass of a cantilever. Mass loading levels of 0.2% or less were statistically indeterminate from a zero load condition ($\alpha = 0.01$), indicating the functional threshold of detection. Further, the results support the design implications from the numerical simulations. Mass identification using arrays with localized responses demonstrates markedly higher variability. The simulation work indicates that the transition from the regime with low disorder and extended modes to the regime in which localization is significant occurs for a normalized mass disorder level that is related to array size, $(\sigma_{\text{mass}}/R) = 1/\sqrt{N}$. Experimental results are consistent with that finding.

7.2 Future Directions

Another important result that should be generated by any research is questions. This body of work not only contributes to the increase in knowledge about the topic, but also provides the opportunity to ask better questions: questions that are more knowledgeable, more focused, and more likely to foster quality future contributions to the understanding of periodic systems and localization in nearly periodic systems. Some of the next steps are quite clear. For example, design and testing of additional prototypes with a wider range of coupling strengths, number of oscillators, and initial mass disorder for further experimental vetting of the results from the numerical simulation. Implementation on a true microscale is also a logical extension.

This work set out to investigate the sensor in a "single snapshot" implementation. Although results for loaded and unloaded states are compared extensively in this work, the sensor is fundamentally not being used in a differential measurement sense. The use of a baseline sensor measurement as a reference state provides a host of opportunities for additional investigation. Use of such a baseline for frequency normalization eliminates the downward shift in the unloaded cantilevers noted in these results and allows for tracking of mass changes in time. Additional simulation work can investigate discrimination of mass addition patterns involving multiple cantilevers and/or variable mass distributions along the cantilever length. Any of these threads provide ample fodder for a trail of subsequent graduate students and researchers to follow. There is, after all, *still* plenty of room at the bottom.

APPENDIX

SENSOR BASELINE MEASUREMENT DATA

This Appendix is a collection of all of the results from the baseline measurements (Protocol AA) for the Type 4 sensors. Frequency response functions, response shapes, frequency distribution and calculated mass values are shown for each of the 12 sensors listed in Table A.1. Of note when scanning through the results is the sharp transition from extended, sinusoidal response shapes in the high and medium *R* sensors to strikingly localized modes in the low *R* sensors.

Sensor type 4
Large array, sanded steel ingot

Protocol:	**AA**	**A**	**B**	**B2**	**B3**	**E**
Sensor	no mass	steel × 4	steel × 4	glass	polystyrene	multiple steel
loa01	✓	✓	✓	✓	✓	✓
loa02	✓		✓			✓
loa03	✓		✓			✓
loa04	✓		✓			
lob01		✓	✓			
lob02			✓			✓
mda01	✓	✓	✓	✓	✓	✓
mda02	✓		✓			✓
mda03	✓		✓			✓
mda04	✓	✓	✓			✓
hia01	✓	✓	✓	✓		✓
hia02	✓	✓	✓	✓	✓	✓
hia03	✓	✓	✓			✓
hia04	✓		✓			✓

Table A.1: Protocols completed with type 4 sensors.

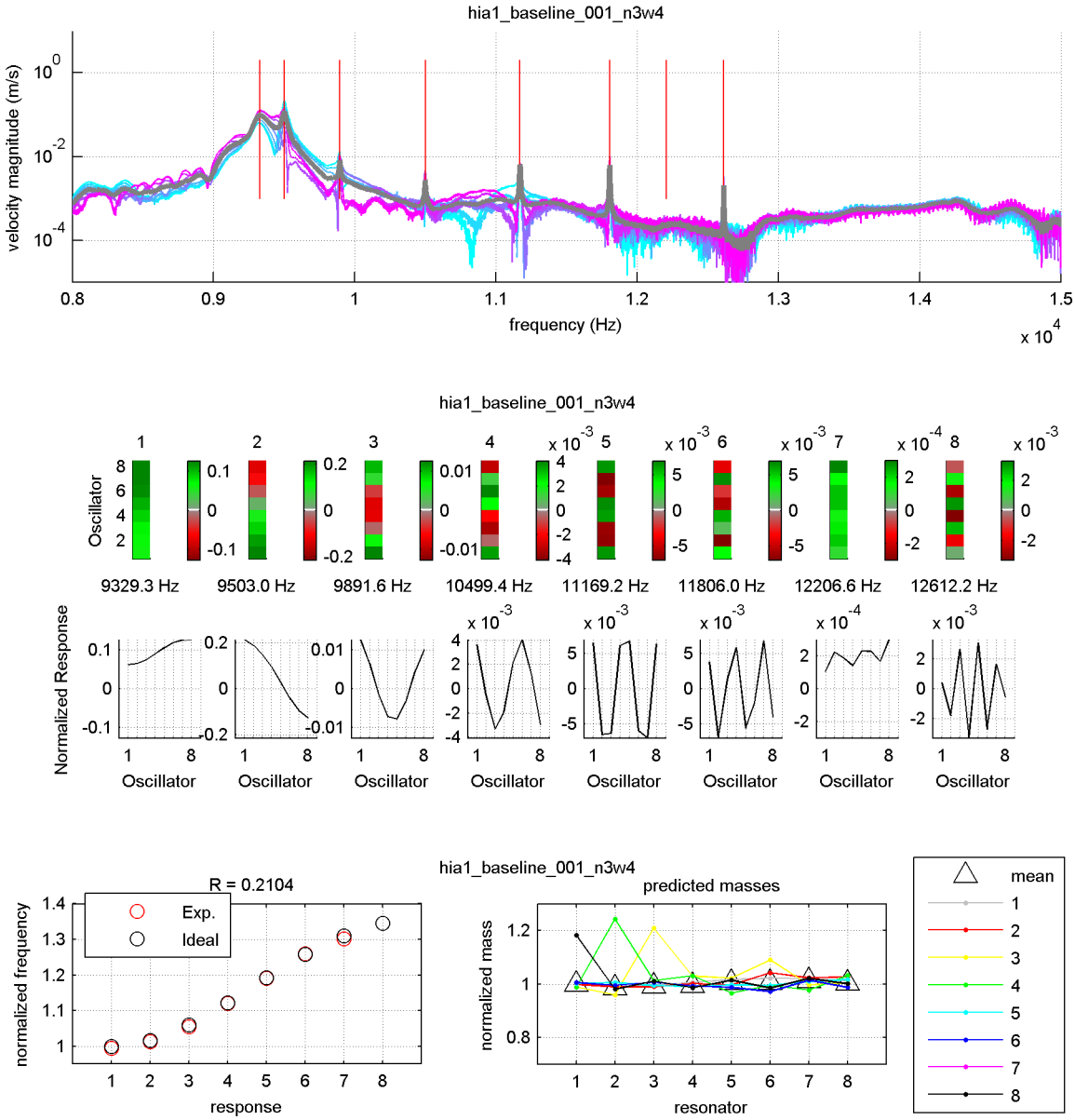

Figure A.1: Frequency response functions, response shapes, frequency distribution and calculated mass values for Protocol AA (baseline, zero loading) for Type 4 sensor hia1

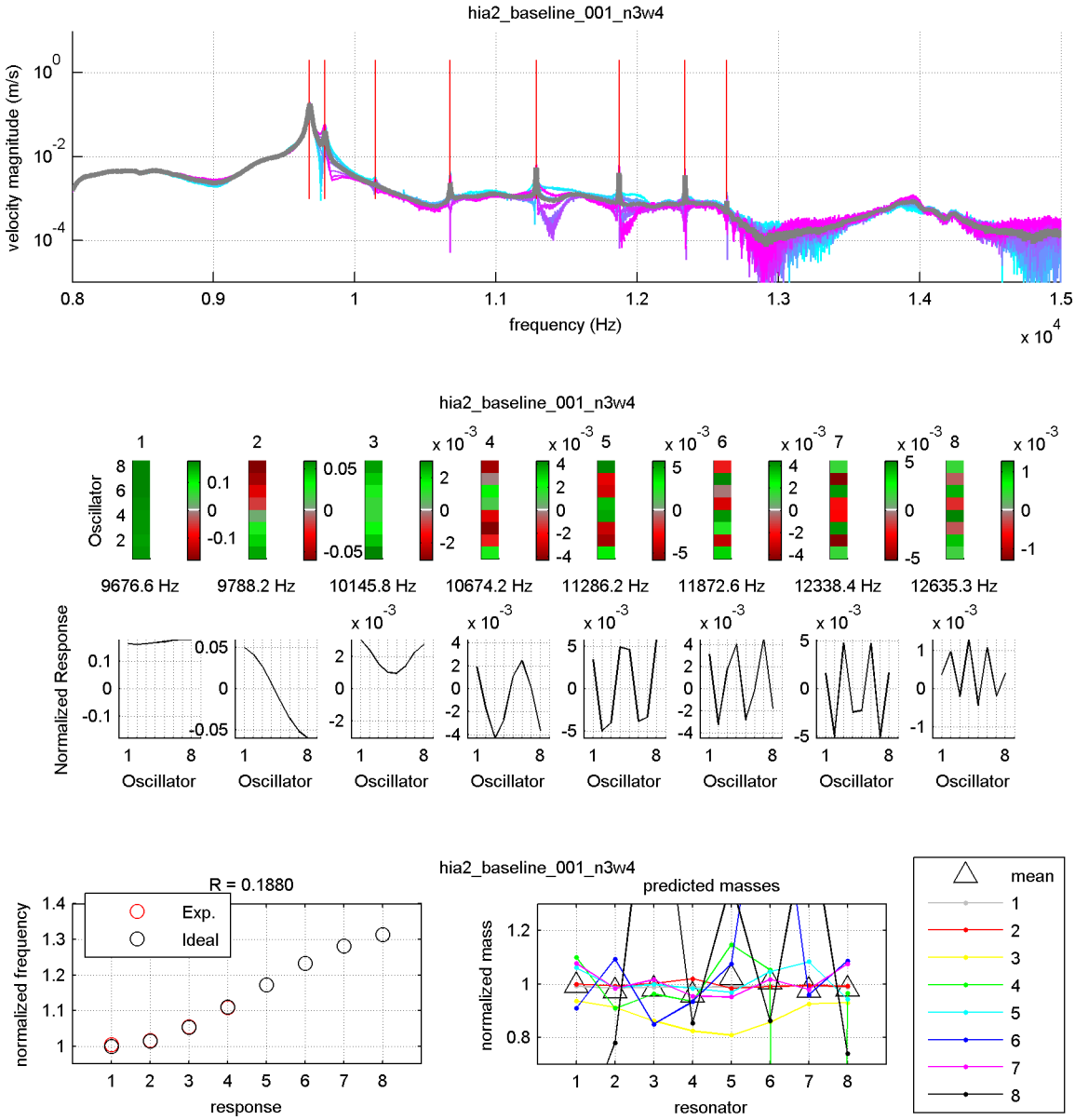

Figure A.2: Frequency response functions, response shapes, frequency distribution and calculated mass values for Protocol AA (baseline, zero loading) for Type 4 sensor hia2

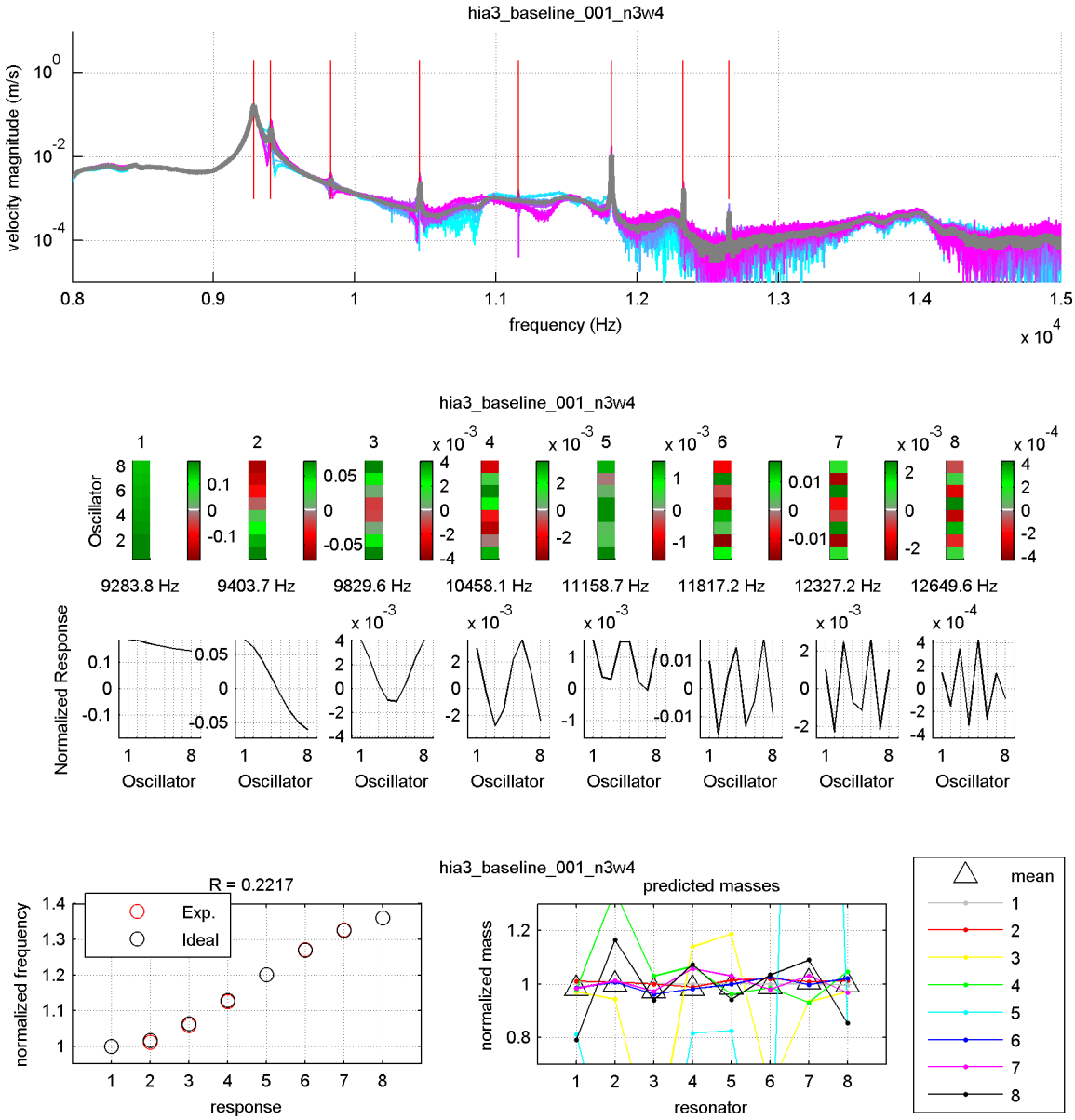

Figure A.3: Frequency response functions, response shapes, frequency distribution and calculated mass values for Protocol AA (baseline, zero loading) for Type 4 sensor hia3

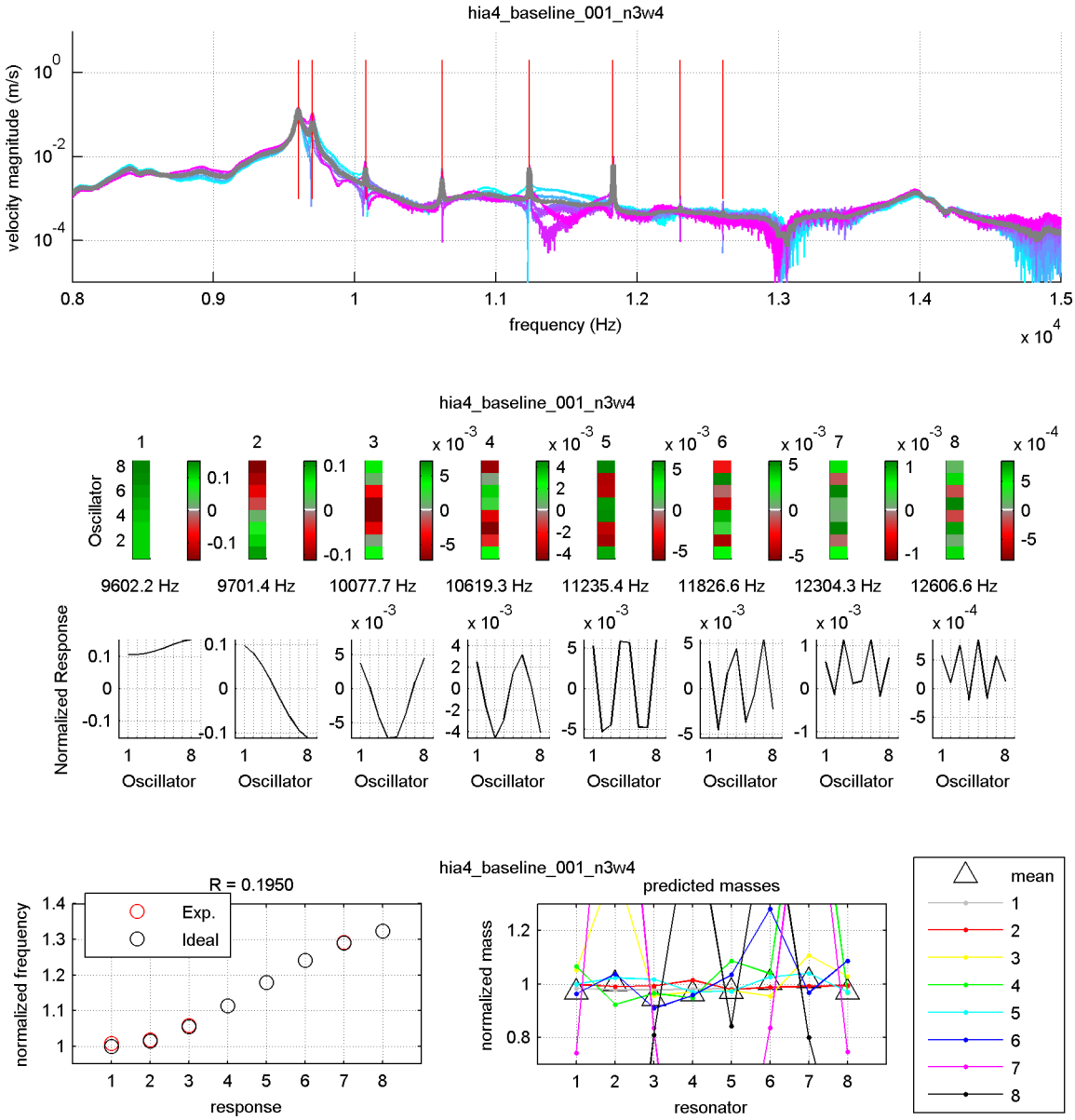

Figure A.4: Frequency response functions, response shapes, frequency distribution and calculated mass values for Protocol AA (baseline, zero loading) for Type 4 sensor hia4

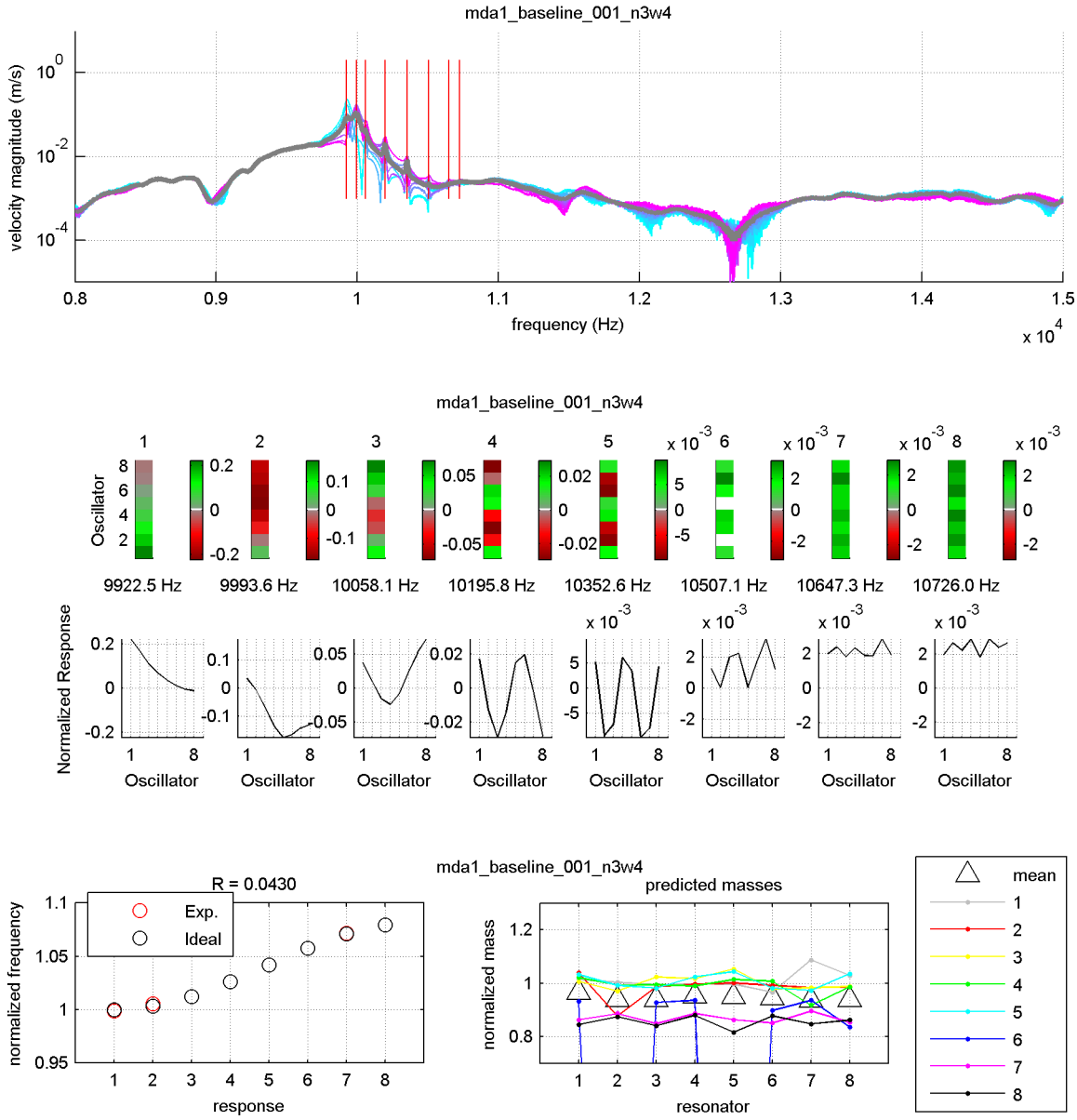

Figure A.5: Frequency response functions, response shapes, frequency distribution and calculated mass values for Protocol AA (baseline, zero loading) for Type 4 sensor mda1

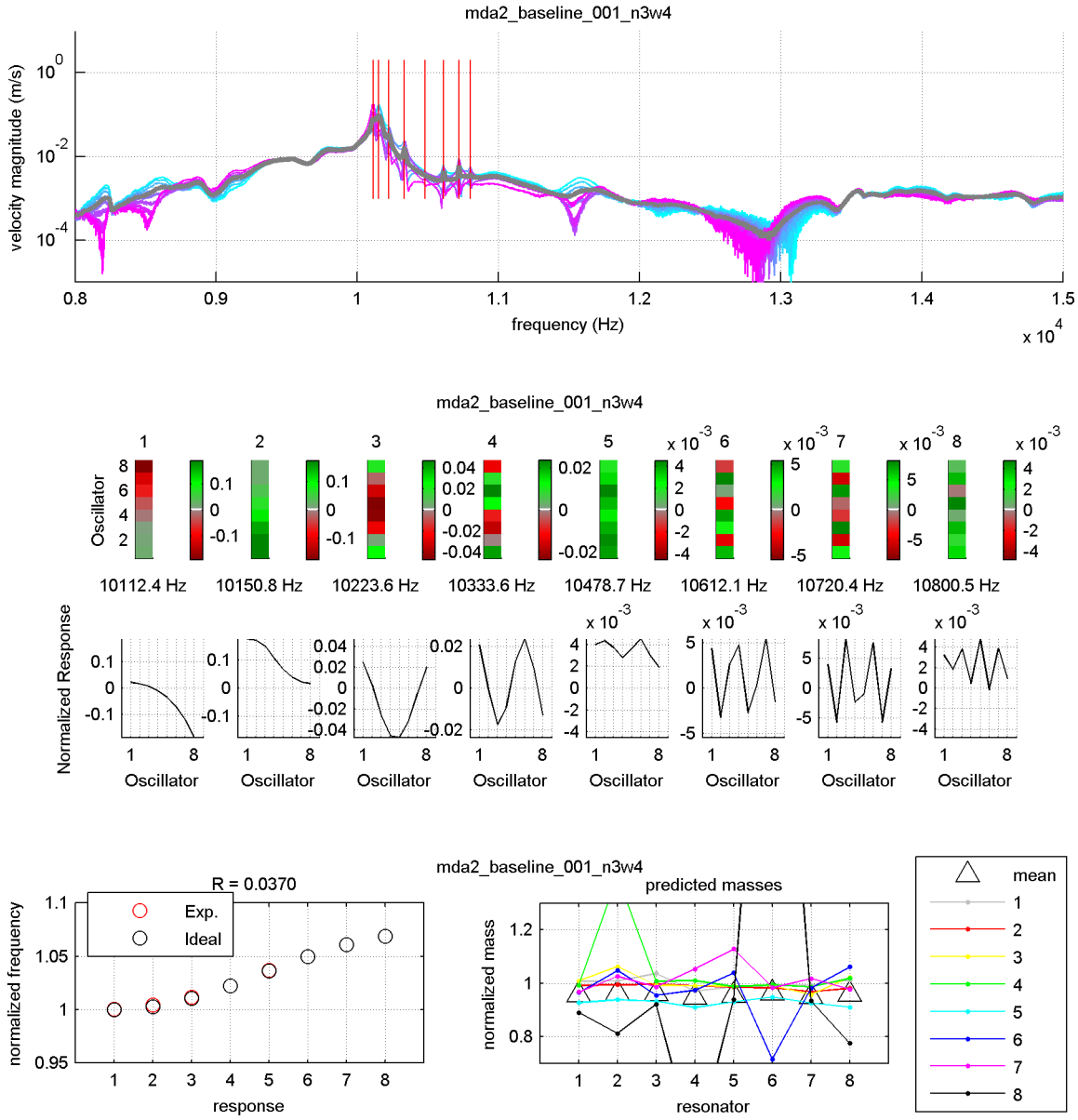

Figure A.6: Frequency response functions, response shapes, frequency distribution and calculated mass values for Protocol AA (baseline, zero loading) for Type 4 sensor mda2

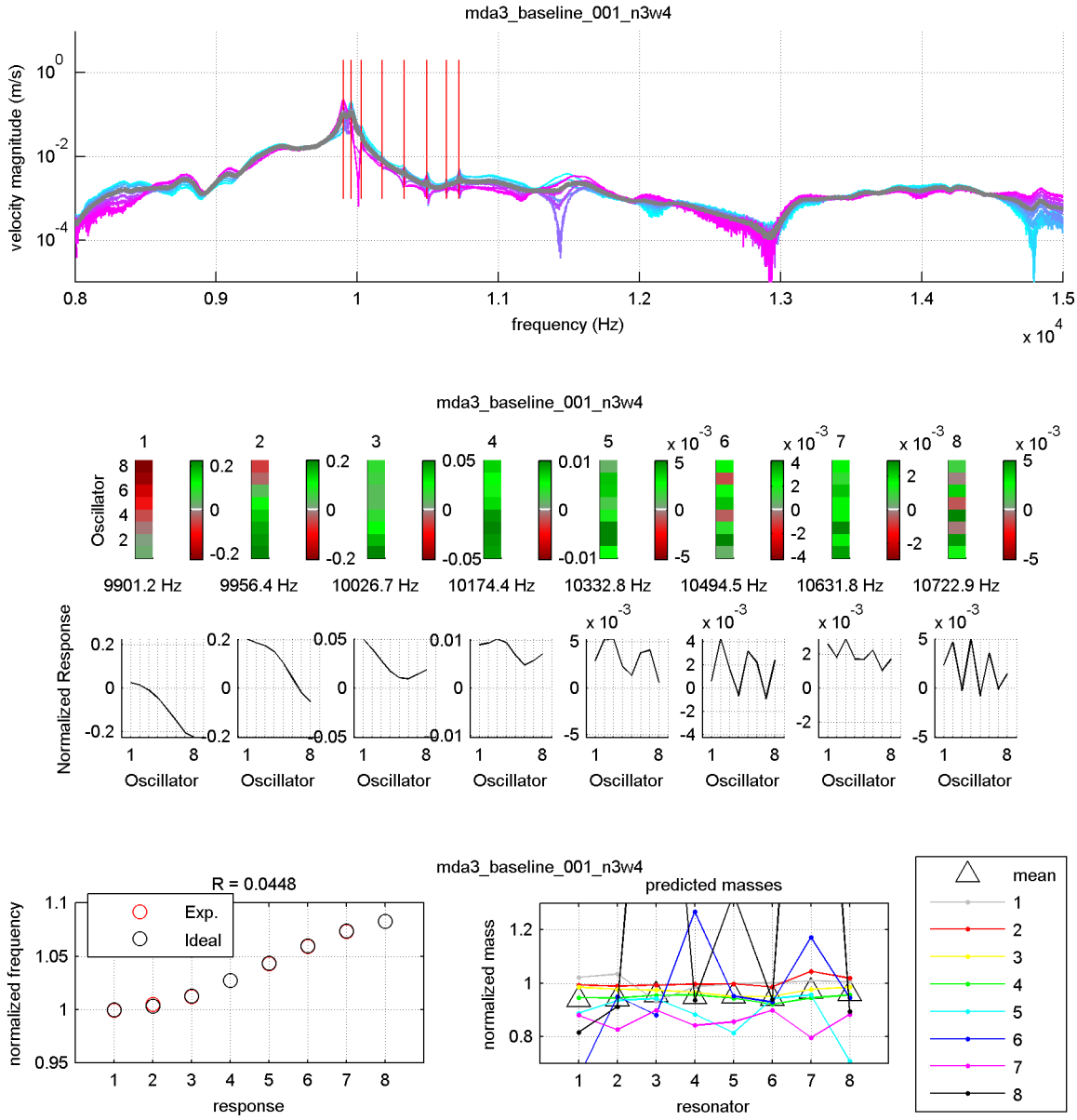

Figure A.7: Frequency response functions, response shapes, frequency distribution and calculated mass values for Protocol AA (baseline, zero loading) for Type 4 sensor mda3

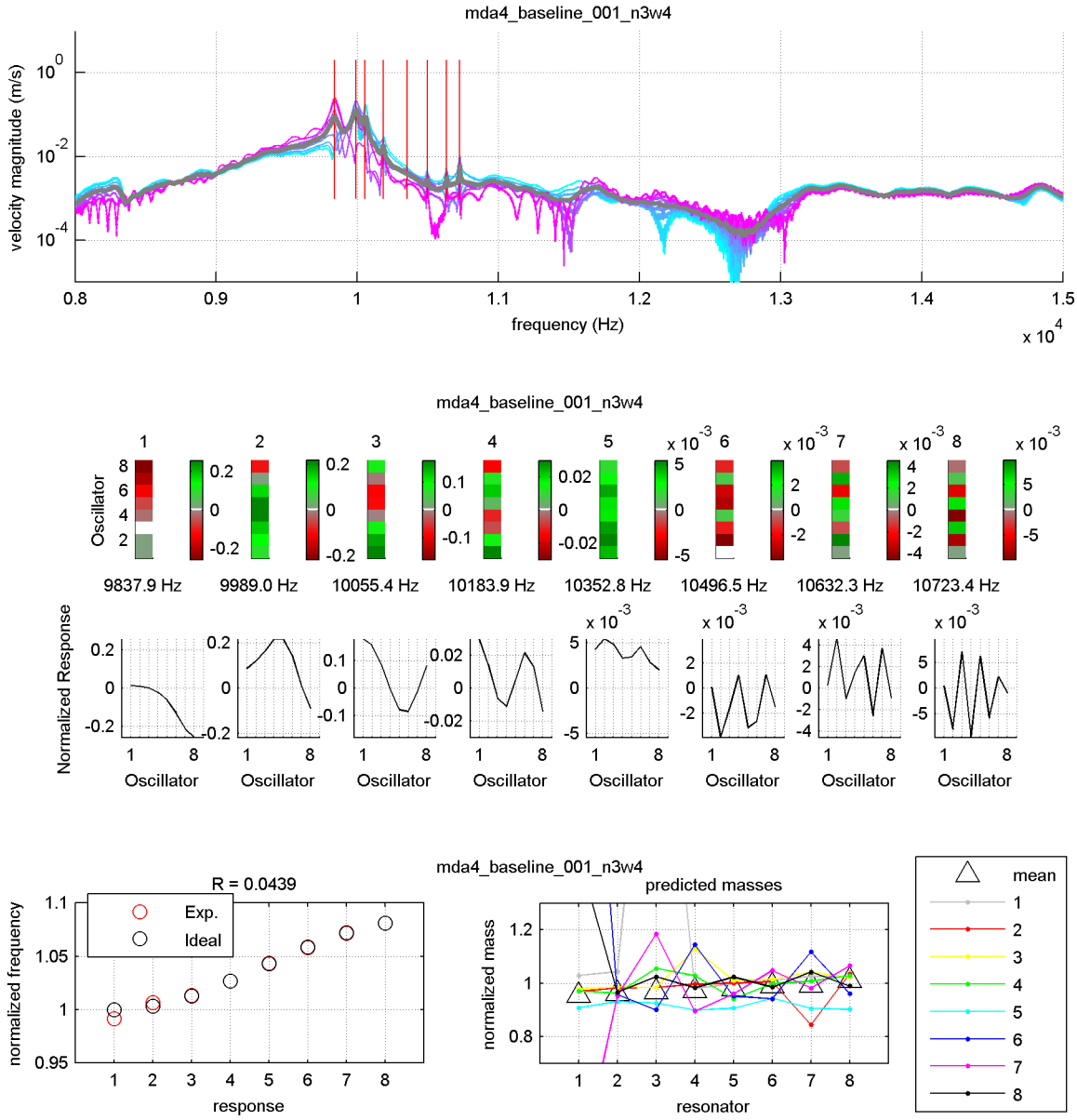

Figure A.8: Frequency response functions, response shapes, frequency distribution and calculated mass values for Protocol AA (baseline, zero loading) for Type 4 sensor mda4

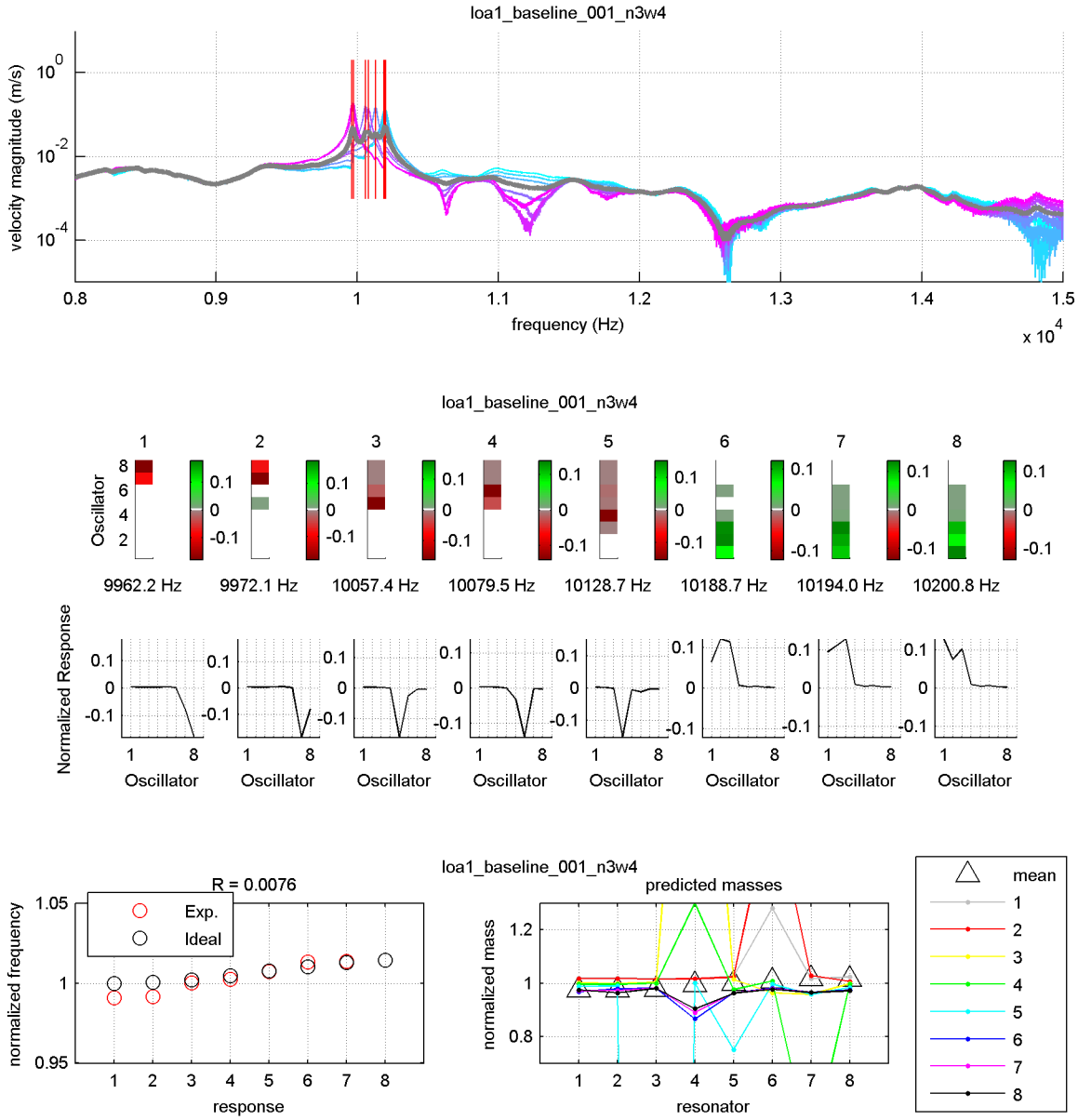

Figure A.9: Frequency response functions, response shapes, frequency distribution and calculated mass values for Protocol AA (baseline, zero loading) for Type 4 sensor loa1

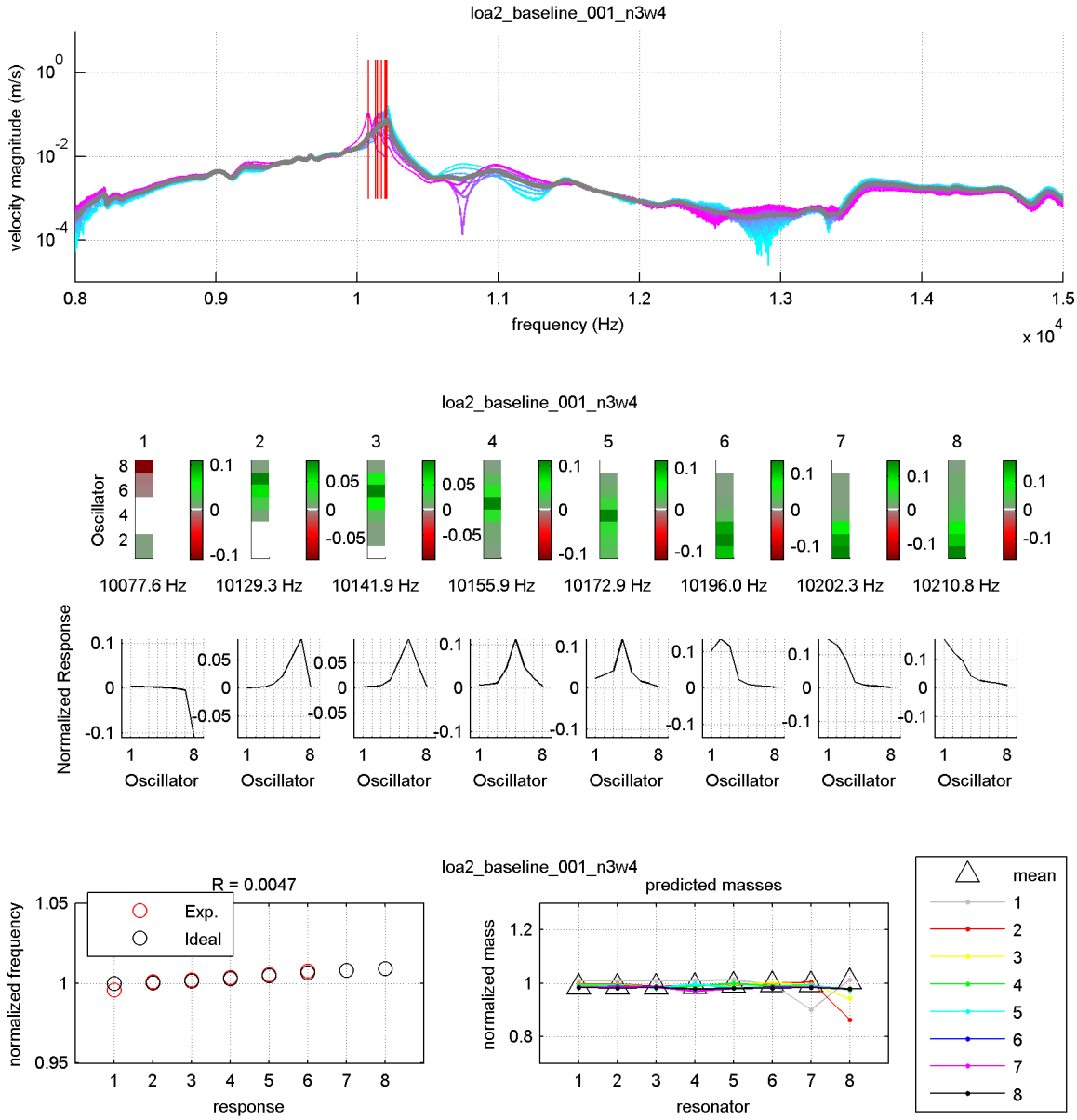

Figure A.10: Frequency response functions, response shapes, frequency distribution and calculated mass values for Protocol AA (baseline, zero loading) for Type 4 sensor loa2

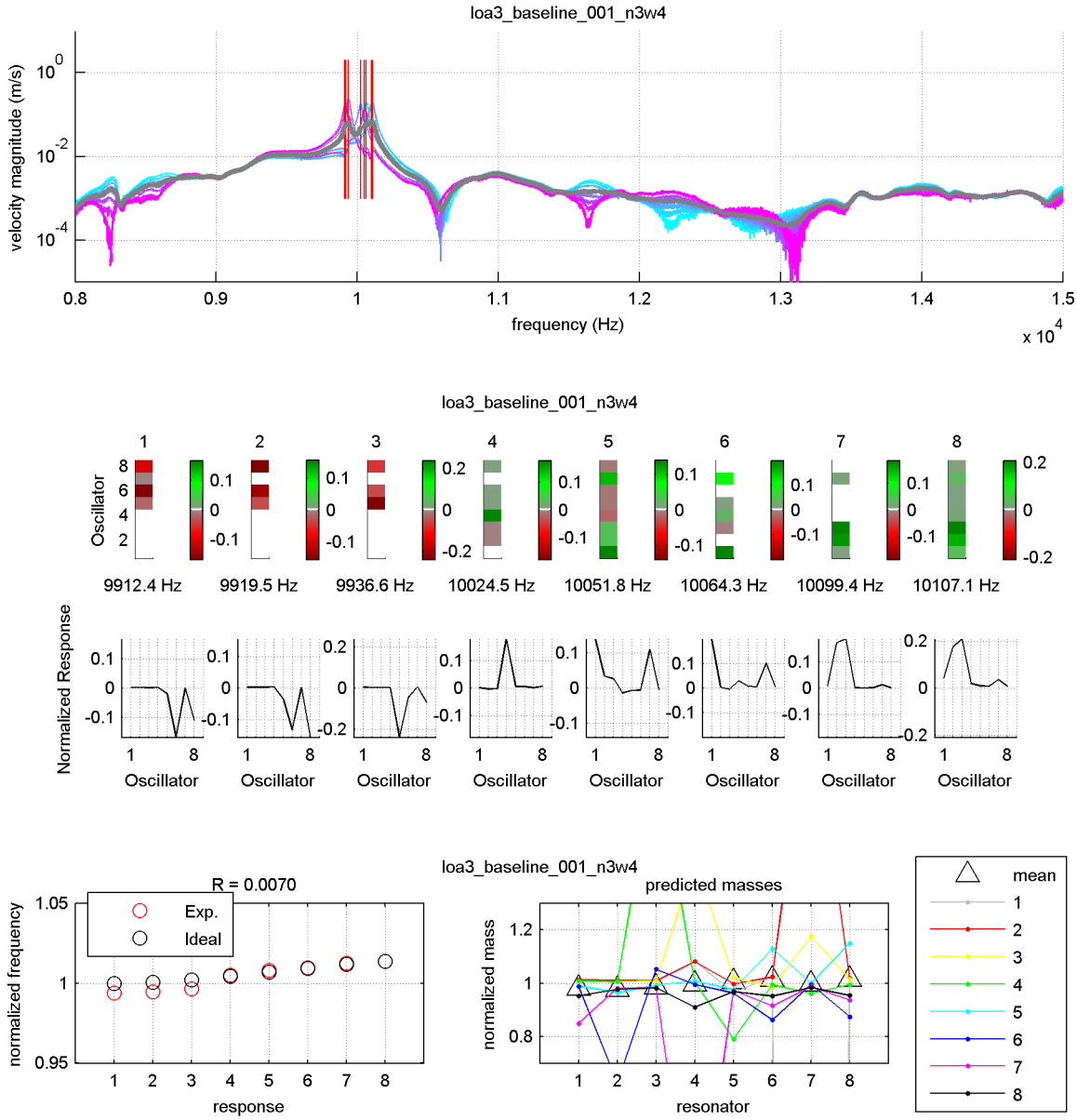

Figure A.11: Frequency response functions, response shapes, frequency distribution and calculated mass values for Protocol AA (baseline, zero loading) for Type 4 sensor loa3

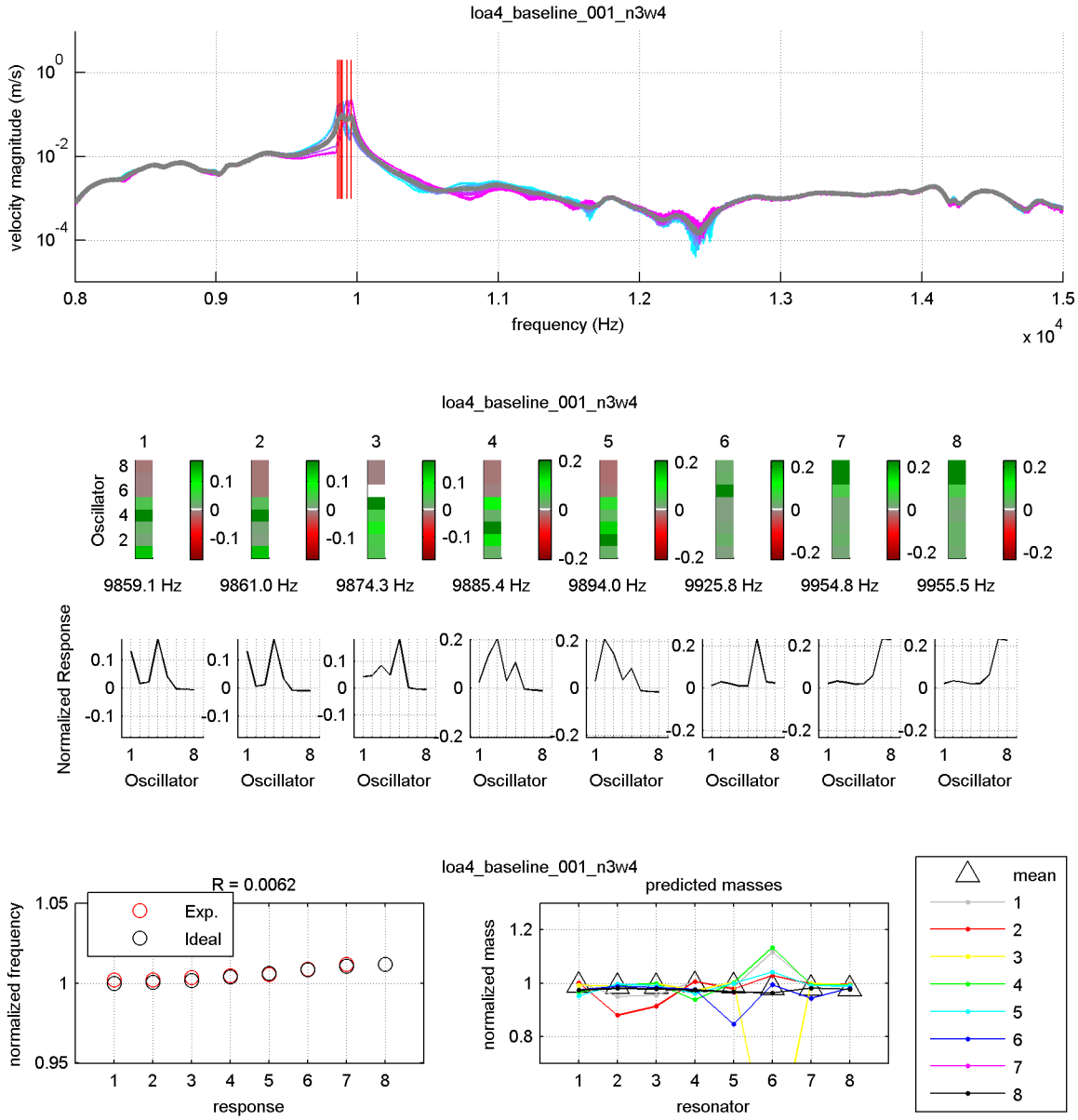

Figure A.12: Frequency response functions, response shapes, frequency distribution and calculated mass values for Protocol AA (baseline, zero loading) for Type 4 sensor loa4

BIBLIOGRAPHY

[1] L. Lin, C. T.-C. Nguyen, R. T. Howe, and A. P. Pisano. Microelectromechanical signal processors, US patent 5455547A, 1995.

[2] M. S. Hanay, S. Kelber, A. K. Naik, D. Chi, S. Hentz, E. C. Bullard, E. Colinet, L. Duraffourg, and M. L. Roukes. Single-protein nanomechanical mass spectrometry in real time. *Nature Nanotechnology*, 7(9):602–608, 2012.

[3] F. M. Battiston, J. P. Ramseyer, H. P. Lang, M. K. Baller, Ch. Gerber, J. K. Gimzewski, E. Meyer, and H-J. Guntherodt. A chemical sensor based on a microfabricated cantilever array with simultaneous resonance-frequency and bending readout. *Sensors and Actuators B-Chemical*, 77:122–131, 2001.

[4] M. K. Baller, H. P. Lang, J. Fritz, Ch. Gerber, J. K. Gimzewski, U. Drechsler, H. Rothuizen, M. Despont, P. Vettiger, F. M. Battiston, J. P. Ramseyer, P. Fornaro, E. Meyer, and H. J. Guntherodt. A cantilever array-based artificial nose. *Ultramicroscopy*, 82:1–9, 2000.

[5] R.P. Feynman. There's plenty of room at the bottom. *Engineering and Science*, 23(5), February 1960.

[6] M. Roukes. Plenty of room, indeed. *Scientific American*, 285(3):48–51, 54–57, September 2001.

[7] J. Chaste, A. Eichler, J. Moser, G. Ceballos, R. Rurali, and A. Bachtold. A nanomechanical mass sensor with yoctogram resolution. *Nature Nanotechnology*, 7(5):301–304, 2012.

[8] D. M. Eigler and E. K. Schweizer. Positioning single atoms with a scanning tunnelling microscope. *Nature*, 344(6266):524–526, April 1990.

[9] S. Beeby, G. Ensell, M. Kraft, and N. White. *MEMS Mechanical Sensors*. Artech House, Inc., Boston, 2004.

[10] M. Elwenspoek and R. Wiegerink. *Mechanical Microsensors*. Springer, January 2001.

[11] H. J. de los Santos. *Introduction To Microelectromechanical Microwave Systems*. Artech House, 2004.

[12] S. D. Senturia. *Microsystem Design*. Springer, November 2000.

[13] C. Liu. *Foundations of MEMS*. Pearson Prentice Hall, 2006.

[14] M. J. Madou. *Fundamentals of Microfabrication: The Science of Miniaturization, Second Edition*. CRC Press, 2 edition, March 2002.

[15] N. V. Lavrik, M. J. Sepaniak, and P. G. Datskos. Cantilever transducers as a platform for chemical and biological sensors. *Review of Scientific Instruments*, 75:2229, 2004.

[16] R. Adler. Compact electromechanical filters. *Electronics*, 20:100–105, 1947.

[17] H. C. Nathanson and R. A. Wickstrom. A resonant-gate silicon surface transistor with high-q band-pass properties. *Applied Physics Letters*, 7(4):84, 1965.

[18] H. C. Nathanson, W. E. Newell, R. A. Wickstrom, and Jr. Davis, J. R. The resonant gate transistor. *IEEE Transactions on Electron Devices*, 14(3):117 – 133, March 1967.

[19] W. E. Newell. Miniaturization of tuning forks. *Science*, 161:1320, 1968.

[20] R. A. Johnson. *Mechanical Filters in Electronics*. Wiley, New York, 1983.

[21] K.E. Petersen. Silicon as a mechanical material. *Proceedings of the IEEE*, 70(5):420 – 457, May 1982.

[22] J. C. Greenwood. Silicon in mechanical sensors. *Journal of Physics E: Scientific Instruments*, 21:1114–1128, 1988.

[23] C.T.-C. Nguyen and R.T. Howe. CMOS micromechanical resonator oscillator. In *Electron Devices Meeting, 1993. IEDM '93. Technical Digest., International*, pages 199 –202, December 1993.

[24] C.T.-C. Nguyen. High-q micromechanical oscillators and filters for communications. In *Proceedings of 1997 IEEE International Symposium on Circuits and Systems, 1997. ISCAS '97*, volume 4, pages 2825 –2828 vol.4, June 1997.

[25] K. Wang and C.T.-C. Nguyen. High-order micromechanical electronic filters. In *Tenth Annual International Workshop on Micro Electro Mechanical Systems, 1997. MEMS '97, Proceedings, IEEE*, pages 25 –30, January 1997.

[26] K. Wang and C.T.-C. Nguyen. High-order medium frequency micromechanical electronic filters. *Journal of Microelectromechanical Systems*, 8(4):534 –556, December 1999.

[27] C.T.-C. Nguyen. Micromechanical filters for miniaturized low-power communications. In *SPIE Proceedings Vol. 3673, Smart Structures and Materials 1999: Smart Electronics and MEMS*, volume 3673, pages 55–66. SPIE, 1999.

[28] F. D. Bannon, J. R. Clark, and C. T.-C. Nguyen. High frequency microelectromechanical IF filters. In *IEEE International Electron Devices Meeting*, pages 773–776, San Francisco, CA, 1996.

[29] F. D. Bannon, J. R. Clark, and C. T.-C. Nguyen. High-q HF microelectromechanical filters. *IEEE Journal of Solid-State Circuits*, 35:512–526, 2000.

[30] J. R. Clark, A.-C. Wong, and C. T.-C. Nguyen. Parallel-resonator HF micromechanical bandpass filters. In *Digest of Technical Papers, 1997 International Conference on Solid-State Sensors and Actuators*, pages 1161–1164, Chicage, 1997.

[31] S. Pourkamali and F. Ayazi. Electrically coupled MEMS bandpass filters part II. without coupling element. *Sensors and Actuators A*, 122:317–325, 2005.

[32] S. Pourkamali and F. Ayazi. Electrically coupled MEMS bandpass filters part i: With coupling element. *Sensors and Actuators A*, 122:307–316, 2005.

[33] W. C. Tang, C. T.-C. Nguyen, and R. T. Howe. Laterally driven polysilicon resonant microstructures. *Sensors and Actuators*, 20(1-2):25–32, November 1989.

[34] W. Tang, C. T.-C. Nguyen, M. Judy, and R. Howe. Electrostatic-comb drive of lateral polysilicon resonators. *Sensors and Actuators A: Physical*, 21(1-3):328–331, February 1990.

[35] D. S. Greywall and P. A. Busch. Coupled micromechanical drumhead resonators with practical application as electromechanical bandpass filters. *Journal of Micromechanics and Microengineering*, 12(6):925–938, November 2002.

[36] L. Lin, R. T. Howe, and A. P. Pisano. Microelectromechanical filters for signal processing. *Journal of Microelecromechanical Systems*, 7:286–294, 1998.

[37] E. Mile, G. Jourdan, I. Bargatin, S. Labarthe, C. Marcoux, P. Andreucci, S. Hentz, C. Kharrat, E. Colinet, and L. Duraffourg. In-plane nanoelectromechanical resonators based on silicon nanowire piezoresistive detection. *Nanotechnology*, 21:7, 2010.

[38] A.-C. Wong and C. T.-C. Nguyen. Micromechanical mixer-filters ("Mixlers"). *Journal of Microelecromechanical Systems*, 13:100–112, 2004.

[39] M.-H. Li, W.-C. Chen, and S.-S. Li. Mechanically coupled CMOS-MEMS free-free beam resonator arrays with enhanced power handling capability. *IEEE Transactions on Ultrasonics, Ferroelectrics and Frequency Control*, 59(3):346 –357, March 2012.

[40] Y. Yuan, J. Xu, Y. Xu, and X. Zhang. A novel microstrip MEMS bandpass filter on silicon substrate. In *2011 International Conference on Electronics, Communications and Control (ICECC)*, pages 1850 –1852, September 2011.

[41] Y.-H. Jang, I. Llamas-Garro, Y.-K. Kim, and J.-M. Kim. RF MEMS suspended band-stop resonator and filter for frequency and bandwidth continuous fine tuning. *Journal of Micromechanics and Microengineering*, 22(1):015005, January 2012.

[42] Y.-W. Yu, J. Zhu, Y. Shi, and L.-L. Jiang. A 12-16 GHz microelectromechanical system-switchable bandpass filter. *Journal of Micromechanics and Microengineering*, 22(7):075010, July 2012.

[43] J. Giner, A. Uranga, J. L. Munoz-Gamarra, E. Marigo, and N. Barniol. A fully integrated programmable dual-band RF filter based on electrically and mechanically coupled CMOS-MEMS resonators. *Journal of Micromechanics and Microengineering*, 22(5):055020, May 2012.

[44] M. Geear, R.R.A. Syms, S. Wright, and A.S. Holmes. Monolithic MEMS quadrupole mass spectrometers by deep silicon etching. *Journal of Microelectromechanical Systems*, 14(5):1156 – 1166, October 2005.

[45] C.A. Musca, J. Antoszewski, K.J. Winchester, A.J. Keating, T. Nguyen, K. Silva, J.M. Dell, L. Faraone, P. Mitra, J.D. Beck, M.R. Skokan, and J.E. Robinson. Monolithic integration of an infrared photon detector with a MEMS-based tunable filter. *IEEE Electron Device Letters*, 26(12):888 – 890, December 2005.

[46] B. Piekarski, D. DeVoe, M. Dubey, R. Kaul, and J. Conrad. Surface micromachined piezoelectric resonant beam filters. *Sensors and Actuators A: Physical*, 91(3):313–320, July 2001.

[47] G. Binnig, C. F. Quate, and Ch. Gerber. Atomic force microscope. *Physical Review Letters*, 56(9):930–933, March 1986.

[48] R. Bogue. MEMS sensors: past, present and future. *Sensor Review*, 27(1):7–13, 2007.

[49] K. Moelhave. Licensed under the creative commons attribution 2.5 generic license. http://commons.wikimedia.org/wiki/File:Epitaxial_Nanowire_Heterostructures_SEM_image.jpg.

[50] J. C. Greenwood. Etched silicon vibrating sensor. *Journal of Physics E: Scientific Instruments*, 17(8):650–652, August 1984.

[51] A. Zribi, A. Knobloch, W.-C. Tian, and S. Goodwin. Micromachined resonant multiple gas sensor. *Sensors and Actuators A: Physical*, 122(1):31–38, July 2005.

[52] E. Stemme and G. Stemme. A balanced resonant pressure sensor. *Sensors and Actuators A: Physical*, 21(1-3):336–341, February 1990.

[53] D.W. Satchell and J.C. Greenwood. A thermally-excited silicon accelerometer. *Sensors and Actuators*, 17(1-2):241–245, May 1989.

[54] R.T. Howe and R.S. Muller. Resonant-microbridge vapor sensor. *IEEE Transactions on Electron Devices*, 33(4):499 – 506, April 1986.

[55] E. Buks and M.L. Roukes. Electrically tunable collective response in a coupled micromechanical array. *Journal of Microelectromechanical Systems*, 11(6):802 – 807, December 2002.

[56] D. L. DeVoe. Piezoelectric thin film micromechanical beam resonators. *Sensors and Actuators A: Physical*, 88(3):263–272, January 2001.

[57] T. Thundat, E. A. Wachter, S. L. Sharp, and R. J. Warmack. Detection of mercury vapor using resonating microcantilevers. *Applied Physics Letters*, 66, 1995.

[58] T. Thundat, R. J. Warmack, G. Y. Chen, and D. P. Allison. Thermal and ambient-induced deflections of scanning force microscope cantilevers. *Applied Physics Letters*, 64:2894–2896, 1994.

[59] T. Thundat, G. Y. Chen, R. J. Warmack, D. P. Allison, and E. A. Wachter. Vapor detection using resonating microcantilevers. *Analytical Chemistry*, 67:519–521, 1995.

[60] P. Melvas, E. Kalvesten, and G. Stemme. A surface-micromachined resonant-beam pressure-sensing structure. *Journal of Microelectromechanical Systems*, 10(4):498 –502, December 2001.

[61] G. Stemme. Resonant silicon sensors. *Journal of Micromechanics and Microengineering*, 1:113–125, 1991.

[62] D. R. Southworth, H. G. Craighead, and J. M. Parpia. Pressure dependent resonant frequency of micromechanical drumhead resonators. *Applied Physics Letters*, 94(21):213506–213506–3, May 2009.

[63] H. J. Mamin and D. Rugar. Sub-attonewton force detection at millikelvin temperatures. *Applied Physics Letters*, 79(20):3358–3360, November 2001.

[64] H. Jung, C. J. Kim, and S. H. Kong. An optimized MEMS-based electrolytic tilt sensor. *Sensors and Actuators A: Physical*, 139(1-2):23–30, September 2007.

[65] X. Zou, P. Thiruvenkatanathan, and A.A. Seshia. Micro-electro-mechanical resonant tilt sensor. In *Frequency Control Symposium (FCS), 2012 IEEE International*, pages 1–4, May 2012.

[66] T. Thundat, S. L. Sharp, W. G. Fisher, R. J. Warmack, and E. A. Wachter. Micromechanical radiation dosimeter. *Applied Physics Letters*, 66(12):1563–1565, March 1995.

[67] P. G. Datskos, P. I. Oden, T. Thundat, E. A. Wachter, R. J. Warmack, and S. R. Hunter. Remote infrared radiation detection using piezoresistive microcantilevers. *Applied Physics Letters*, 69(20):2986–2988, November 1996.

[68] T. Ono and M. Esashi. Magnetic force and optical force sensing with ultrathin silicon resonator. *Review of Scientific Instruments*, 74(12):5141–5146, December 2003.

[69] A. C. Stephan, T. Gaulden, A. D. Brown, M. Smith, L. F. Miller, and T. Thundat. Microcantilever charged-particle flux detector. *Review of Scientific Instruments*, 73(1):36–41, January 2002.

[70] S. P. Beeby, J. N. Ross, and N. M. White. Design and fabrication of a micromachined silicon accelerometer with thick-film printed PZT sensors. *Journal of Micromechanics and Microengineering*, 10(3):322–328, September 2000.

[71] A. N. Cleland and M L Roukes. A nanometre-scale mechanical electrometer. *Nature*, 392(6672):160–162, 1998.

[72] O. Sahin, G. Yaralioglu, R. Grow, S.F. Zappe, A. Atalar, C. Quate, and O. Solgaard. High-resolution imaging of elastic properties using harmonic cantilevers. *Sensors and Actuators A: Physical*, 114(2-3):183–190, September 2004.

[73] A. W. McFarland, M. A. Poggi, M. J. Doyle, L. A. Bottomley, and J. S. Colton. Influence of surface stress on the resonance behavior of microcantilevers. *Applied Physics Letters*, 87(5):053505–053505–3, July 2005.

[74] K. L. Ekinci, X. M. H. Huang, and M. L. Roukes. Ultrasensitive nanoelectromechanical mass detection. *Applied Physics Letters*, 84, 2004.

[75] A. Gupta, D. Akin, and R. Bashir. Single virus particle mass detection using microresonators with nanoscale thickness. *Applied Physics Letters*, 84, 2004.

[76] B. Ilic, D. Czaplewski, M. Zalalutdinov, H. G. Craighead, P. Neuzil, C. Campagnolo, and C. Batt. Single cell detection with micromechanical oscillators. *Journal of Vacuum Science & Technology B*, 19:2825–2828, 2001.

[77] R. J. Linderman, P. E. Kladitis, and V. M. Bright. Development of the micro rotary fan. *Sensors and Actuators A: Physical*, 95(2-3):135–142, January 2002.

[78] R. A. Conant, J. T. Nee, K. Y. Lau, and R. S. Muller. A flat high-frequency scanning micromirror. In *Proc. Solid-State Sensor and Actuator Workshop*, page 6âĂŞ9, 2000.

[79] P. C. Fletcher. Licensed under the creative commons attribution-share alike 3.0 unported license. http:// commons.wikimedia.org/wiki/File:MEMS_Microcantilever_in_Resonance.png.

[80] N. Licensed under the creative commons attribution-share alike 3.0 unported license. http://commons.wikimedia.org/wiki/File:IZM_Silicon_Micropump.jpg.

[81] S. Prescesky, M. Paraeswaran, A. Rawicz, R. F. B. Turner, and U. Reichl. Silicon micromachining technology for sub-nanogram discrete mass biosensors. *Canadian Journal of Physics*, 70:1178–1183, 1992.

[82] T. Ono, X. Li, H. Miyashita, and M. Esashi. Mass sensing of adsorbed molecules in sub-picogram sample with ultrathin silicon resonator. *Review of Scientific Instruments*, 74, 2003.

[83] N. V. Lavrik and P. G. Datskos. Femtogram mass detection using photothermally actuated nanomechanical resonators. *Applied Physics Letters*, 82(16):2697–2699, April 2003.

[84] B. Ilic, H. G. Craighead, S. Krylov, W. Senaratne, C. Ober, and P. Neuzil. Attogram detection using nanoelectromechanical oscillators. *Journal of Applied Physics*, 95:3694, 2004.

[85] M. Li, H. X. Tang, and M. L. Roukes. Ultra-sensitive NEMS-based cantilevers for sensing, scanned probe and very high-frequency applications. *Nature Nanotechnology*, 2(2):114–120, January 2007.

[86] Y. T. Yang, C. Callegari, X. L. Feng, K. L. Ekinci, and M. L. Rouke. Zeptogram-scale nanomechanical mass sensing. *Nano Letters*, 6:583–586, 2006.

[87] H.-Y. Chiu, P. Hung, H. W. Ch. Postma, and M. Bockrath. Atomic-scale mass sensing using carbon nanotube resonators. *Nano Letters*, 8(12):4342–4346, December 2008.

[88] T. J. Quinn. News from the BIPM. *Metrologia*, 29, 1992.

[89] L. A. Pinnaduwage, A. Wig, D. L. Hedden, A. Gehl, D. Yi, T. Thundat, and R. T. Lareau. Detection of trinitrotoluene via deflagration on a microcantilever. *Journal of Applied Physics*, 95(10):5871 –5875, May 2004.

[90] G. Y. Chen, T. Thundat, E. A. Wachter, and R. J. Warmack. Adsorption-induced surface stress and its effects on resonance frequency of microcantilevers. *Journal of Applied Physics*, 77:3618–3622, 1995.

[91] G. Y. Huang, W. Gao, and S. W. Yu. Model for the adsorption-induced change in resonance frequency of a cantilever. *Applied Physics Letters*, 89(4):043506–043506–3, July 2006.

[92] B. Kim, M.A. Hopcroft, R.N. Candler, C.M. Jha, M. Agarwal, R. Melamud, S.A. Chandorkar, G. Yama, and T.W. Kenny. Temperature dependence of quality factor in MEMS resonators. *Journal of Microelectromechanical Systems*, 17(3):755 –766, June 2008.

[93] K. Y. Yasamura, T. D. Stowe, E. M. Chow, T. Pfafman, T. W. Kenny, B. C. Stipe, and D. Rugar. Quality factors in micron- and submicron-thick cantilevers. *Journal of Microelecromechanical Systems*, 9:117–125, 2000.

[94] A. N. Cleland and M. L. Roukes. Noise processes in nanomechanical resonators. *Journal of Applied Physics*, 92(5):2758 –2769, September 2002.

[95] A. N. Cleland. Thermomechanical noise limits on parametric sensing with nanomechanical resonators. *New Journal of Physics*, 7:235–235, November 2005.

[96] K. L. Ekinci, Y. T. Yang, and M. L. Roukes. Ultimate limits to inertial mass sensing based upon nanoelectromechanical systems. *Journal of Applied Physics*, 95, 2004.

[97] J. L. Arlett and M. L Roukes. Ultimate and practical limits of fluid-based mass detection with suspended microchannel resonators. *Journal of Applied Physics*, 108(8):084701–084701–11, October 2010.

[98] M. Li. *Very high frequency nanoelectromechanical resonators and their chemical sensing applications*. PhD thesis, California Institute of Technology, Pasadena, CA, USA, 2007.

[99] I. Voiculescu, M.E. Zaghloul, R.A. McGill, E.J. Houser, and G.K. Fedder. Electrostatically actuated resonant microcantilever beam in CMOS technology for the detection of chemical weapons. *IEEE Sensors Journal*, 5(4):641–647, August 2005.

[100] M. Spletzer, A. Raman, and R. Reifenberger. Elastometric sensing using higher flexural eigenmodes of microcantilevers. *Applied Physics Letters*, 91(18):184103–184103–3, November 2007.

[101] J. Tamayo, D. Ramos, J. Mertens, and M. Calleja. Effect of the adsorbate stiffness on the resonance response of microcantilever sensors. *Applied Physics Letters*, 89(22):224104, November 2006.

[102] R. Raiteri, M. Grattarola, H. J. Butt, and P. Skladal. Micromechanical cantilever-based biosensors. *Sensors and Actuators B: Chemical*, 79(2-3):115–126, October 2001.

[103] H.-J. Butt. A sensitive method to measure changes in the surface stress of solids. *Journal of Colloid and Interface Science*, 180(1):251–260, June 1996.

[104] M. Maute, S. Raible, F.E. Prins, D.P. Kern, H. Ulmer, U. Weimar, and W. GÃűpel. Detection of volatile organic compounds (VOCs) with polymer-coated cantilevers. *Sensors and Actuators B: Chemical*, 58(1-3):505–511, September 1999.

[105] A. Subramanian, P. I. Oden, S. J. Kennel, K. B. Jacobson, R. J. Warmack, T. Thundat, and M. J. Doktycz. Glucose biosensing using an enzyme-coated microcantilever. *Applied Physics Letters*, 81(2):385 –387, July 2002.

[106] B. Ilic, D. Czaplewski, H. G. Craighead, P. Neuzil, C. Campagnolo, and C. Batt. Mechanical resonant immunospecific biological detector. *Applied Physics Letters*, 77:450–452, 2000.

[107] R. L. Gunter, W. G. Cady, K. Manygoats, A. Kooser, and T. L. Porter. Viral detection using an embedded piezoresistive microcantilever sensor. *Sensors and Actuators A: Physical*, 107(3):219–224, November 2003.

[108] N. V. Lavrik. Microsensors, macrosensitivity. *oemagazine*, 2005.

[109] M. Alvarez and L. M. Lechuga. Microcantilever-based platforms as biosensing tools. *Analyst*, 135(5), 2010.

[110] M. Zougagh and A. Rios. Micro-electromechanical sensors in the analytical field. *Analyst*, 134(7):1274–1290, June 2009.

[111] R. Maboudian and C. Carraro. Surface chemistry and tribology of mems. *Annual Review of Physical Chemistry*, 55(1):35–54, 2004.

[112] P. Xu, H. Yu, and X. Li. Functionalized mesoporous silica for microgravimetric sensing of trace chemical vapors. *Analytical Chemistry*, 83(9):3448–3454, May 2011.

[113] L. Sekaric, M. Zalalutdinov, R. B. Bhiladvala, A. T. Zehnder, J. M. Parpia, and H. G. Craighead. Operation of nanomechanical resonant structures in air. *Applied Physics Letters*, 81:2641–2643, 2002.

[114] D. Jin, X. Li, J. Liu, G. Zuo, Y. Wang, M. Liu, and H. Yu. High-mode resonant piezoresistive cantilever sensors for tens-femtogram resoluble mass sensing in air. *Journal of Micromechanics and Microengineering*, 16(5):1017–1023, May 2006.

[115] T. M. Huber, B. C. Abell, D. C. Mellema, M. Spletzer, and A. Raman. Mode-selective non-contact excitation of microcantilevers and microcantilever arrays in air using the ultrasound radiation force. *Applied Physics Letters*, 97(21):214101–214101–3, November 2010.

[116] A. P. Davila, J. Jang, A. K. Gupta, T. Walter, A. Aronson, and R. Bashir. Microresonator mass sensors for detection of bacillus anthracis sterne spores in air and water. *Biosensors and Bioelectronics*, 22:3028–3035, 2007.

[117] L.A. Beardslee, F. Josse, S.M. Heinrich, I. Dufour, and O. Brand. Geometrical considerations for the design of liquid-phase biochemical sensors using a cantilever's fundamental in-plane mode. *Sensors and Actuators B: Chemical*, 164(1):7–14, March 2012.

[118] C. P. Green and J. E. Sader. Frequency response of cantilever beams immersed in viscous fluids near a solid surface with applications to the atomic force microscope. *Journal of Applied Physics*, 98(11):114913, 2005.

[119] J. E. Sader. Frequency response of cantilever beams immersed in viscous fluids with applications to the atomic force microscope. *Journal of Applied Physics*, 84(1):64–76, July 1998.

[120] C. Ziegler. Cantilever-based biosensors. *Analytical and Bioanalytical Chemistry*, 379(7-8), July 2004.

[121] M. Yue, H. Lin, D. E. Dedrick, S. Satyanarayana, A. Majumdar, A. S. Bedeckar, . W. Jenkins, and S. Sundaram. A 2-d microcantilever array for multiplexed biomolecular analysis. *Journal of Microelectromechanical Systems*, 13:290–299, 2004.

[122] J. Park, T. Asakura, H. Kim, S. Kim, D. Yoon, C. Cheon, H. Kim, and T. Kim. Resonance properties and mass sensitivity of monolithic microcantilever sensors actuated by piezoelectric PZT thick film. *Journal of Electroceramics*, 17(2):565–572, 2006.

[123] J. L. Arlett, E. B. Myers, and M. L. Roukes. Comparative advantages of mechanical biosensors. *Nature Nanotechnology*, 6(4):203–215, 2011.

[124] M. K. Ghatkesar, T. Braun, V. Barwich, J.-P. Ramseyer, C. Gerber, M. Hegner, and H. P. Lang. Resonating modes of vibrating microcantilevers in liquid. *Applied Physics Letters*, 92(4):043106, 2008.

[125] T. P. Burg, M. Godin, S. M. Knudsen, W. Shen, G. Carlson, J. S. Foster, K. Babcock, and S. R. Manalis. Weighing of biomolecules, single cells and single nanoparticles in fluid. *Nature*, 446(7139):1066–1069, April 2007.

[126] T. P. Burg and S. R. Manalis. Suspended microchannel resonators for biomolecular detection. *Applied Physics Letters*, 83(13):2698–2700, September 2003.

[127] T. P. Burg, A. R. Mirza, N. Milovic, C. H. Tsau, G. A. Popescu, J. S. Foster, and S. R. Manalis. Vacuum-packaged suspended microchannel resonant mass sensor for biomolecular detection. *Journal of Microelectromechanical Systems*, 15(6):1466–1476, December 2006.

[128] A. N. Cleland and M. L. Roukes. Fabrication of high frequency nanometer scale mechanical resonators from bulk si crystals. *Applied Physics Letters*, 69(18):2653 –2655, October 1996.

[129] T. Kemp and M. Ward. Tunable response nano-mechanical beam resonator. *Sensors and Actuators A: Physical*, 123-124:281–284, September 2005.

[130] B. Ilic, S. Krylov, K. Aubin, R. Reichenbach, and H. G. Craighead. Optical excitation of nanoelectromechanical oscillators. *Applied Physics Letters*, 86(19):193114, 2005.

[131] B. Ilic, S. Krylov, M. Kondratovich, and H.G. Craighead. Optically actuated nanoelectromechanical oscillators. *IEEE Journal of Selected Topics in Quantum Electronics*, 13(2):392 –399, April 2007.

[132] I. Bargatin, I. Kozinsky, and M. L. Roukes. Efficient electrothermal actuation of multiple modes of high-frequency nanoelectromechanical resonators. *Applied Physics Letters*, 90(9):093116 –093116–3, February 2007.

[133] H. Jianqiang, Z. Changchun, L. Junhua, and H. Yongning. Dependence of the resonance frequency of thermally excited microcantilever resonators on temperature. *Sensors and Actuators A: Physical*, 101(1-2):37–41, September 2002.

[134] A. R. Kadam, G. P. Nordin, and M. A. George. Use of thermally induced higher order modes of a microcantilever for mercury vapor detection. *Journal of Applied Physics*, 99(9):094905 –094905–4, May 2006.

[135] S. Basak, A. Raman, and S. V. Garimella. Dynamic response optimization of piezoelectrically excited thin resonant beams. *Journal of Vibration and Acoustics*, 127(1):18–27, 2005.

[136] C.R. Tellier and T.G. Leblois. On the design of GaAs (hhl) resonant cantilevers: Study of piezoelectric excitation, of piezoresistive sensing and of micromachined structure. *Sensors and Actuators A: Physical*, 132(1):224–235, November 2006.

[137] M. D. LaHaye, O. Buu, B. Camarota, and K. C. Schwab. Approaching the quantum limit of a nanomechanical resonator. *Science*, 304(5667):74–77, April 2004.

[138] L. Sekaric, J.M. Parpia, H.G. Craighead, T. Fegelson, B.H. Houston, and J.E. Butler. Nanomechanical resonant structures in nanocrystalline diamond. *Applied Physics Letters*, 81:23, 2002.

[139] H. B. Peng, C. W. Chang, S. Aloni, T. D. Yuzvinsky, and A. Zettl. Ultrahigh frequency nanotube resonators. *Physical Review Letters*, 97(8):087203, August 2006.

[140] A. N. Cleland, M. Pophristic, and I. Ferguson. Single-crystal aluminum nitride nanomechanical resonators. *Applied Physics Letters*, 79(13):2070 –2072, September 2001.

[141] X. M. H. Huang, C. A. Zorman, M. Mehregany, and M. L. Roukes. Nanoelectromechanical systems: Nanodevice motion at microwave frequencies. *Nature*, 421(6922):496–496, January 2003.

[142] J. S. Bunch, A. M. van der Zande, S. S. Verbridge, I. W. Frank, D. M. Tanenbaum, J. M. Parpia, H. G. Craighead, and P. L. McEuen. Electromechanical resonators from graphene sheets. *Science*, 315(5811):490–493, January 2007.

[143] A. K. Naik, O. Buu, M. D. LaHaye, A. D. Armour, A. A. Clerk, M. P. Blencowe, and K. C. Schwab. Cooling a nanomechanical resonator with quantum back-action. *Nature*, 443(7108):193–196, September 2006.

[144] R. G. Knobel and A. N. Cleland. Nanometre-scale displacement sensing using a single electron transistor. *Nature*, 424(6946):291–293, July 2003.

[145] D. Rugar, R. Budakian, H. J. Mamin, and B. W. Chui. Single spin detection by magnetic resonance force microscopy. *Nature*, 430(6997):329–332, July 2004.

[146] H. J. Mamin, M. Poggio, C. L. Degen, and D. Rugar. Nuclear magnetic resonance imaging with 90-nm resolution. *Nature Nanotechnology*, 2(5):301–306, May 2007.

[147] B. Rogers, L. Manning, M. Jones, I. Sulchek, K. Murray, B. Beneschott, J. D. Adams, Z. Hu, T. Thundat, H. Cavazos, and S. C. Minne. Mercury vapor detection with a self-sensing, resonating piezoelectric cantilever. *Review of Scientific Instruments*, 74(11):4899, November 2003.

[148] D. Chen, J. Wang, Y. Xu, and L. Zhang. A thin film electro-acoustic enzyme biosensor allowing the detection of trace organophosphorus pesticides. *Analytical Biochemistry*, 429(1):42–44, October 2012.

[149] H. P. Lang, R. Berger, F. Battiston, J.-P. Ramseyer, E. Meyer, C. Andreoli, J. Brugger, P. Vettiger, M. Despont, and T. Mezzacasa. A chemical sensor based on a micromechanical cantilever array for the identification of gases and vapors. *Applied Physics A: Materials Science & Processing*, 66:61–64, 1998.

[150] D. Lange, C. Hagleitner, A. Hierlemann, O. Brand, and H. Baltes. Complementary metal oxide semiconductor cantilever arrays on a single chip: Mass-sensitive detection of volatile organic compounds. *Analytical Chemistry*, 74(13):3084–3095, July 2002.

[151] L. A. Pinnaduwage, V. I. Boiadjiev, G. M. Brown, T. Thundat, and S. W. Petersen. Detection of hexavalent chromium in ground water using a single microcantilever sensor. *Sensor Letters*, 2(1):25–30, March 2004.

[152] A. ul Haque, M. Rokkam, A.R. De Carlo, S.T. Wereley, S.J. Roux, P.P. Irazoqui, and D.M. Porterfield. A MEMS fabricated cell electrophysiology biochip for in silico calcium measurements. *Sensors and Actuators B: Chemical*, 123(1):391–399, April 2007.

[153] C.-H. Chen, R.-Z. Hwang, L.-S. Huang, S.-M. Lin, H.-C. Chen, Y.-C. Yang, Y.-T. Lin, S.-A. Yu, Y.-S. Lin, Y-H. Wang, N.-K. Chou, and S.-S. Lu. A wireless bio-MEMS sensor for c-reactive protein detection based on nanomechanics. *IEEE Transactions on Biomedical Engineering*, 56(2):462–470, February 2009.

[154] X. Su, C. Dai, J. Zhang, and S. J. O'Shea. Quartz tuning fork biosensor. *Biosensors and Bioelectronics*, 17(1-2):111–117, January 2002.

[155] J. Fritz, M. K. Baller, H. P. Lang, H. Rothuizen, P. Vettiger, E. Meyer, HJ Guntherodt, Ch. Gerber, and J. K. Gimzewski. Translating biomolecular recognition into nanomechanics. *Science*, 288:316–318, 2000.

[156] K. M. Klein, J. Zheng, A. Gewirtz, D. S. Sarma, S. Rajalakshmi, and K. Sitaraman. Array of nano-cantilevers as a bio-assay for cancer diagnosis. In *Electronic Components and Technology Conference, 2005. Proceedings. 55th*, pages 583 –587, June 2005.

[157] M. Su, S. Li, and V. P. Dravid. Microcantilever resonance-based DNA detection with nanoparticle probes. *Applied Physics Letters*, 82, 2003.

[158] B. Dhayal, W. A. Henne, D. D. Doorneweerd, R. G. Reifenberger, and P. S. Low. Detection of bacillus subtilis spores using peptide-functionalized cantilever arrays. *Journal of the American Chemical Society*, 128(11):3716–3721, March 2006.

[159] B. Ilic, Y. Yang, and H. G. Craighead. Virus detection using nanoelectromechanical devices. *Applied Physics Letters*, 85(13):2604 –2606, September 2004.

[160] N. Nugaeva, K. Y. Gfeller, N. Backmann, H. P. Lang, M. Duggelin, and M. Hegner. Micromechanical cantilever array sensors for selective fungal immobilization and fast growth detection. *Biosensors and Bioelectronics*, 21(6):849–856, December 2005.

[161] K. Y. Gfeller, N. Nugaeva, and M. Hegner. Micromechanical oscillators as rapid biosensor for the detection of active growth of escherichia coli. *Biosensors and Bioelectronics*, 21(3):528–533, September 2005.

[162] G. A. Campbell and R. Mutharasan. PEMC sensor's mass change sensitivity is 20 pg/Hz under liquid immersion. *Biosensors and Bioelectronics*, 22(1):35–41, July 2006.

[163] L. B. Sharos, A. Raman, S. Crittenden, and R. Reifenberger. Enhanced mass sensing using torsional and lateral resonances in microcantilevers. *Applied Physics Letters*, 84(23):4638–4640, May 2004.

[164] W. Pang, L. Yan, H. Zhang, H. Yu, E. S. Kim, and W. C. Tang. Femtogram mass sensing platform based on lateral extensional mode piezoelectric resonator. *Applied Physics Letters*, 88(24):243503–243503–3, June 2006.

[165] H. Yu and X. Li. Bianalyte mass detection with a single resonant microcantilever. *Applied Physics Letters*, 94(1):011901–011901–3, January 2009.

[166] Z. Shen, W. Y. Shih, and W.-H. Shih. Mass detection sensitivity of piezoelectric cantilevers with a nonpiezoelectric extension. *Review of Scientific Instruments*, 77(6):065101–1–065101–10, June 2006.

[167] A. K. Kar and M. A. George. Improved detection of thermally induced higher resonance modes and harmonics of a microcantilever. *Journal of Applied Physics*, 94(7):4626–4631, October 2003.

[168] E. Gil-Santos, D. Ramos, J. Martinez, M. Fernandez-Regulez, R. Garcia, A. San Paulo, M. Calleja, and J. Tamayo. Nanomechanical mass sensing and stiffness spectrometry based on two-dimensional vibrations of resonant nanowires. *Nat Nano*, 5(9):641–645, 2010.

[169] S. Dohn, R. Sandberg, W. Svendsen, and A. Boisen. Enhanced functionality of cantilever based mass sensors using higher modes. *Applied Physics Letters*, 86(23):233501–233501–3, June 2005.

[170] S. Dohn, W. Svendsen, A. Boisen, and O. Hansen. Mass and position determination of attached particles on cantilever based mass sensors. *Review of Scientific Instruments*, 78(10):103303–103303–3, October 2007.

[171] S. Dohn, S. Schmid, F. Amiot, and A. Boisen. Position and mass determination of multiple particles using cantilever based mass sensors. *Applied Physics Letters*, 97(4):044103–044103–3, July 2010.

[172] D. Ramos, J. Tamayo, J. Mertens, M. Calleja, and A. Zaballos. Origin of the response of nanomechanical resonators to bacteria adsorption. *Journal of Applied Physics*, 100(10):106105–106105–3, November 2006.

[173] H. P. Lang, M. Hegner, and C. Gerber. Cantilever array sensors. *Materials Today*, 8(4):30–36, April 2005.

[174] H. P. Lang, M. K. Baller, R Berger, Ch Gerber, J. K. Gimzewski, F. M. Battiston, P. Fornaro, J. P. Ramseyer, E. Meyer, and H. J. Guntherodt. An artificial nose based on a micromechanical cantilever array. *Analytica Chimica Acta*, 393(1-3):59–65, June 1999.

[175] S. Z. Lulec, C. Sagiroglu, A. Mostafazadeh, E. Ermek, E. Timurdogan, Y. Leblebici, and H. Urey. Simultaneous self-sustained actuation and parallel readout with MEMS cantilever sensor array. In *Micro Electro Mechanical Systems (MEMS), 2012 IEEE 25th International Conference on*, pages 644–647, 2012.

[176] G.-C. Wei and M. S.-C. Lu. Design and characterization of a CMOS MEMS capacitive resonant sensor array. *Journal of Micromechanics and Microengineering*, 22(12):125030, December 2012.

[177] J.F. Vignola, J.A. Judge, and A.J. Kurdila. Shaping of a system's frequency response using an array of subordinate oscillators. *Journal of the Acoustical Society of America*, 126:129–139, 2009.

[178] A. A. J. Glean, J. A. Judge, and J. F. Vignola. Inverse eigenmode method for identifying and locating added mass in mechanically diverse coupled microresonantor arrays. In *ASME 2011 International Design Engineering Technical Conferences and Computers and Information in Engineering Conference (IDETC/CIE2011) 5th International Conference on Micro- and Nanosystems*, volume 7, pages 219–226. ASME, August 2011.

[179] A. A. J. Glean, J. F. Vignola, J. A. Judge, T. J. Woods, and P. F. O'Malley. Disorder in subordinate oscillators arrays used to shape the response of dynamic systems. In *The 161st Meeting of the Acoustical Society of America*, volume 129, pages 2612–2612, May 2011.

[180] J. F. Vignola, A. A. J. Glean, J. A. Judge, and T. J. Ryan. Alternative approach to rapid step response with limited ringing and light damping. *Journal of the Acoustical Society of America*, in review.

[181] M. Strasberg and D. Feit. Vibration damping of large structures induced by attached small resonant structures. *Journal of the Acoustical Society of America*, 99:335–344, 1996.

[182] M. Strasberg. Continuous structures as "fuzzy" substructures. *Journal of the Acoustical Society of America*, 100:3456–3459, 1996.

[183] R.J. Nagem, I. Veljkovic, and G. Sandri. Vibration damping by a continuous distribution of undamped oscillators. *Journal of Sound and Vibration*, 207(3):429–434, October 1997.

[184] G. Maidanik. Induced damping by a nearly continuous distribution of nearly undamped oscillators: linear analysis. *Journal of Sound and Vibration*, 240:717–731, 2001.

[185] A. Carcaterra and A. Akay. Theoretical foundations of apparent-damping phenomena and nearly irreversible energy exchange in linear conservative systems. *Journal of the Acoustical Society of America*, 121:1971–1982, 2007.

[186] A. S. Alsuwaiyan and S. W. Shaw. Localization of free vibration modes in systems of nearly identical vibration absorbers. *Journal of Sound Vibration*, 228:703–711, December 1999.

[187] A. F. Vakakis and C. Cetinkaya. Mode localization in a class of multidegree-of-freedom nonlinear systems with cyclic symmetry. *SIAM Journal on Applied Mathematics*, 53(1):265–282, February 1993.

[188] B. E. DeMartini, J. F. Rhoads, M. A. Zielke, K. G Owen, S. W. Shaw, and K. L. Turner. A single input-single output coupled microresonator array for the detection and identification of multiple analytes. *Applied Physics Letters*, 93:054102, 2008.

[189] B. E. DeMartini, J. F. Rhoads, S. W. Shaw, and K. L. Turner. A single input-single output mass sensor based on a coupled array of microresonators. *Sensors and Actuators A*, 137:147–156, 2007.

[190] M. Spletzer, A. Raman, A. Q. Wu, X. Xu, and R. Reifenberger. Ultrasensitive mass sensing using mode localization in coupled microcantilevers. *Applied Physics Letters*, 88, 2006.

[191] M. Spletzer, A. Raman, H. Sumali, and J. P. Sullivan. Highly sensitive mass detection and identification using vibration localization in coupled microcantilever arrays. *Applied Physics Letters*, 92, 2008.

[192] P. Thiruvenkatanathan, J. Yan, J. Woodhouse, and A. A. Seshia. Enhancing parametric sensitivity in electrically coupled MEMS resonators. *Journal of Microelecromechanical Systems*, 18:1077–1085, 2009.

[193] P. Thiruvenkatanathan, J. Yan, J. Woodhouse, A. Aziz, and A. A. Seshia. Ultrasensitive mode-localized mass sensor with electrically tunable parametric sensitivity. *Applied Physics Letters*, 96(8):081913, 2010.

[194] P. Thiruvenkatanathan, Jize Yan, and A.A. Seshia. Differential amplification of structural perturbations in weakly coupled MEMS resonators. *IEEE Transactions on Ultrasonics, Ferroelectrics and Frequency Control*, 57(3):690–697, March 2010.

[195] A. A. J. Glean, J. F. Vignola, J. A. Judge, and T. J. Ryan. Mass sensing using the time-domain response of a MEMS structure with a functionalized subordinate oscillator array. In *Proceedings of the ASME IDETC/CIE 2013 7th International Conference on Micro- and Nanosystems (MNS)*, Portland, Oregon, August 2013. ASME.

[196] P. Thiruvenkatanathan, J. Woodhouse, J. Yan, and A. A. Seshia. Limits to mode-localized sensing using micro- and nanomechanical resonator arrays. *Journal of Applied Physics*, 109(10):104903, 2011.

[197] D. Pfister-Senz. Licensed under the creative commons attribution-share alike 3.0 unported license. http://commons.wikimedia.org/wiki/File:Turbine_Grafenrheinfeld.jpg.

[198] E. Silversmith. Licensed under the creative commons attribution-share alike 3.0 unported license. http://commons.wikimedia.org/wiki/File:Sydney_harbour_bridge_B%26W.jpg.

[199] A. D. Pierce, V. W. Sparrow, and D. A. Russell. Fundamental structural-acoustic idealizations for structures with fuzzy internals. *Journal of Vibration and Acoustics*, 117:339–348, 1995.

[200] A. Carcaterra, A. Akay, and F. Lenti. Pseudo-damping in undamped plates and shells. *Journal of the Acoustical Society of America*, 122:804–813, 2007.

[201] A. Carcaterra and A. Akay. Transient energy exchange between a primary structure and a set of oscillators: Return time and apparent damping. *The Journal of the Acoustical Society of America*, 115(2):683–696, 2004.

[202] L. Brillouin. *Wave Propagation in Periodic Structures: Electric Filters and Crystal Lattices*. Courier Dover Publications, December 2003.

[203] A. Lagendijk, B. van Tiggelen, and D. S. Wiersma. Fifty years of anderson localization. *Physics Today*, 62(8):24–29, 2009.

[204] P. W. Anderson. Absence of diffusion in certain random lattices. *Physical Review*, 109(5):1492–1505, March 1958.

[205] D. J. Ewins. A study of resonance coincidence in bladed discs. *Journal of Mechanical Engineering Science*, 12(5):305–312, October 1970.

[206] C. H. Hodges and J. Woodhouse. Vibration isolation from irregularity in a nearly periodic structure: Theory and measurements. *The Journal of the Acoustical Society of America*, 74(3):894–905, 1983.

[207] C. Pierre and E.H. Dowell. Localization of vibrations by structural irregularity. *Journal of Sound and Vibration*, 114(3):549–564, May 1987.

[208] S.-T. Wei and C. Pierre. Localization phenomena in mistuned assemblies with cyclic symmetry part i: Free vibrations. *Journal of Vibration Acoustics Stress and Reliability in Design*, 110(4):429, 1988.

[209] M. P. Castanier and C. Pierre. Individual and interactive mechanisms for localization and dissipation in a mono-coupled nearly periodic structure. *Journal of Sound and Vibration*, 163:479–505, 1993.

[210] C. H. Hodges and J. Woodhouse. Confinement of vibration by one-dimensional disorder, II: a numerical experiment on different ensemble averages. *Journal of Sound and Vibration*, 130(2):253–268, April 1989.

[211] C. H. Hodges and J. Woodhouse. Confinement of vibration by one-dimensional disorder, i: Theory of ensemble averaging. *Journal of Sound and Vibration*, 130(2):237–251, April 1989.

[212] J. A. Judge, B. Houston, D. Photiadis, and P. Herdic. Effects of disorder in one and two dimensional micromechanical resonator arrays for filtering. *Journal of Sound and Vibration*, 290:1119–1140, 2006.

[213] D. J. Mead. Wave propagation and natural modes in periodic systems: I. mono-coupled systems. *Journal of Sound and Vibration*, 40(1):1–18, May 1975.

[214] O. O. Bendiksen. Localization phenomena in structural dynamics. *Chaos, Solitons & Fractals*, 11(10):1621–1660, August 2000.

[215] L. E. Kinsler, A. R. Frey, A. B. Coppens, and J. V. Sanders. *Fundamentals of Acoustics*. Wiley, 4th edition, December 1999.

[216] C. H. Hodges. Confinement of vibration by structural irregularity. *Journal of Sound and Vibration*, 82(3):411–424, June 1982.

[217] M. Spletzer, A. Raman, R. Reifenberger, A. Q. Wu, and S. Xu. Biochemical mass detection using mode localization in microcantilever arrays. In *ASME 2005 International Mechanical Engineering Congress and Exposition (IMECE2005)*, volume 2005, pages 493–497. ASME, 2005.

[218] J. A. Judge, J. F. Vignola, B. H. Houston, D. M. Photiadis, and M. H. Marcus. Vibration localization in near-periodic coupled two-dimensional resonator arrays. In *Volume 1: 20th Biennial Conference on Mechanical Vibration and Noise, Parts A, B, and C*, pages 2495–2504, Long Beach, California, USA, September 2005.

[219] R. B. Bhiladvala and Z. J. Wang. Effect of fluids on the q factor and resonance frequency of oscillating micrometer and nanometer scale beams. *Physical Review E*, 69(3), March 2004.

[220] K. L. Ekinci and M. L. Roukes. Nanoelectromechanical systems. *Review of Scientific Instruments*, 76:061101, 2005.

[221] K. Eom, H. S. Park, D. S. Yoon, and T. Kwon. Nanomechanical resonators and their applications in biological/chemical detection: Nanomechanics principles. *Physics Reports*, 503(4-5):115–163, June 2011.

[222] C. Pierre. Weak and strong vibration localization in disordered structures: A statistical investigation. *Journal of Sound and Vibration*, 139(1):111–132, May 1990.

[223] J. H. Ginsberg. *Mechanical and Structural Vibrations*. John Wiley & Sons, New York, 2001.

[224] J. A. Judge, T. J. Woods, and J. F. Vignola. Considerations for use of square-paddle resonators for arrays of micro- and nanoscale devices. In *ASME 2009 International Design Engineering Technical Conferences and Computers and Information in Engineering Conference (IDETC/CIE2009)*, San Diego, CA, 2009.

[225] J. A. Judge, T. J. Woods, J. F. Vignola, P. F. O'Malley, and S. A. Mathews. Investigation of bandpass filters implemented via two-dimensional arrays of micromechanical resonators. In *Proceedings of 2009 NSF Engineering Research and Innovation Conference*, Honolulu, Hawaii, 2009.

[226] J. A. Judge, T. J. Woods, J. F. Vignola, P. F. O'Malley, and A. A. Glean. Experimental identification of resonator mass and stiffness in micromechanical and nanomechanical resonator arrays. In *Proceedings of the 2011 NSF Engineering Research and Innovation Conference*, Atlanta, Georgia, 2011.

[227] T. J. Ryan, J. A. Judge, and J. F. Vignola. Identification of mass distribution of nominally identical microresonator arrays in the presence of measurement noise. In *ASME (IDETC/CIE2011) 5th International Conference on Micro- and Nanosystems*, volume 7, pages 227–233, Washington, DC, USA, August 2011. ASME.

[228] A. A. J. Glean, J. A. Judge, J. F. Vignola, P. F. O'Malley, and T. J. Ryan. Graduate and undergraduate laboratory courses in acoustics and vibration. In *Proceedings of Meetings on Acoustics, 161st Meeting of the Acoustical Society of America*, volume 12, page 025002, Seattle, Washington, May 2011.

[229] T. J. Ryan, J. A. Judge, A. A. J. Glean, and J. F. Vignola. Noise sensitivity of a mass detection method using vibration modes of coupled microcantilever arrays. *Applied Physics Letters*, 101(4):043104–1–4, July 2012.

[230] P. F. O'Malley, T. J. Woods, J. A. Judge, and J. F. Vignola. Five-axis scanning laser vibrometry for three-dimensional measurements of non-planar surfaces. *Measurement Science and Technology*, 20:115901–9, 2009.